3-21-2019

Direct Numerical Simulation of Roughness Induced Hypersonic Boundary Layer Transition on a 7° Half-Angle Cone

Tara E. Crouch

Direct Numerical Simulation of Roughness Induced Hypersonic Boundary Layer Transition on a 7° Half-Angle Cone

THESIS

Crouch, Tara E., 1st Lt, USAF

AFIT-ENY-MS-19-M-211

DEPARTMENT OF THE AIR FORCE
AIR UNIVERSITY

AIR FORCE INSTITUTE OF TECHNOLOGY

Wright-Patterson Air Force Base, Ohio

AFIT-ENY-MS-19-M-211

HYPERSONIC BOUNDARY-LAYER TRANSITION DIRECT NUMERICAL SIMULATION AT MACH 10 ON 7° CONE

THESIS

Presented to the Faculty

Department of Aeronautics and Astronautics

Graduate School of Engineering and Management

Air Force Institute of Technology

Air University

Air Education and Training Command

in Partial Fulfillment of the Requirements for the

Degree of Master of Science (Aerospace Engineering)

Crouch, Tara E., BS

1st Lt, USAF

21 March 2019

AFIT-ENY-MS-19-M-211

HYPERSONIC BOUNDARY-LAYER TRANSITION DIRECT NUMERICAL SIMULATION AT MACH 10 ON 7° CONE

THESIS

Crouch, Tara E., BS
1st Lt, USAF

Committee Membership:

Lt Col. Jeffrey R. Komives, PhD
Chair

Mark F. Reeder, PhD
Member

Robert B. Greendyke, PhD
Member

Abstract

Direct numerical simulation (DNS) computational fluid dynamic (CFD) calculations were performed on a 30° slice of 7° half-angle cones with increasing nose radii bluntness at Mach 10 while simulating a distributed roughness pattern on the cone surface. These DNS computations were designed to determine if the non-modal transition behavior observed in testing performed at the Arnold Engineering Development Center (AEDC) Hypervelocity Wind Tunnel 9 was induced via distributed surface roughness. When boundary layer transition is dominated by second mode instabilities, an increase in nose radius delays the transition location downstream. However, blunt nose experiments indicated that as the nose radius continued to increase from sharp to blunt, the transition location was no longer second mode dominated and the transition location failed to continue to move downstream. The cause of this non-modal transition phenomenon is unknown but is hypothesized to be due to distributed roughness on the surface of the test articles. The DNS grids utilized in this research effort simulated distributed roughness along the surface of the cone by moving the nodes on the surface according to a normal distribution centered on the maximum roughness height and having the nodes in the direction normal to the cone move in a hyperbolic tangent descent. The results showed that the distributed surface roughness was not sufficient to cause transitional flow by itself. Distributed surface roughness may still be an influencing factor for the non-modal transition observed in the blunt nose cone experiments performed by the AEDC Tunnel 9 but an additional forcing function would have needed to be present to cause transitional flow.

To my supportive husband

Acknowledgements

First and foremost I would like to thank my research adviser Lt. Col. Jeffrey Komives for his investment in my graduate career and his investment in my professional career as an officer. His strong guidance and encouragement to push the limits of science inspires those who have the honor of having him as a professor or adviser. Lt. Col. Komives's admirable sense of purpose to shaping young officers into critical technology experts inspires me to find the same level of meaning in all my future jobs.

Additionally, I should extend this thanks to Lt. Col. Komives's research group, members past and present, for their help in my work. Specifically thanking Capt. Ryan Thompson who endured this journey beside me but in many ways paved the way for me.

I would like to thank the members of my committee, Dr. Mark Reeder and Dr. Robert Greendyke for their expert critiques and advice. A special thanks is extended to Dr. Marc Polanka who spent many hours providing feedback on my thesis drafts. It was his early feedback which set high personal expectations and it is his care for the quality of theses which raises the bar within AFIT.

Many thanks is extended to the Department of Defense High Performance Computing program. The technology and service provided by the DoDHPC program advances the DoD's scientific research daily and without access to their resources my research effort would not have been feasible. Warm thanks is extended to the entire AFIT Computer Support and Help Office. I am eternally grateful to Mr. Dave Doak who has kept the AFIT Linux Lab operational despite many difficulties far beyond his control.

I would like to thank my sponsoring organization, the Arnold Engineering Development Complex Hypervelocity Wind Tunnel 9 for funding this research

effort. I owe thanks to Dr. John Lafferty and Mr. George Moraru for their collaboration which helped to inspire and scope my work.

My thanks is extended to Capt. Grant Johnson, Lt. Avery Leonard, and Lt. Ryan Saunders who provided camaraderie, help, and encouragement throughout the entire CFD sequence. There is no greater graduate school blessing than an amazing study group.

Finally, I would like to thank my husband for being my partner through this AFIT journey and all future adventures which the Air Force and life will send us on.

Crouch, Tara E.

Table of Contents

Page

List of Figures

List of Tables

List of Symbols

Symbol		Page
R_N	Nose Radius, mm	2
s	Streamwise Coordinate, m	4
St	Stanton Number	4
Re_L	Reynolds Number Based on Cone Length	4
$\dot{q}$	Heat Transfer per unit Area, $\frac{\mathrm{W}}{\mathrm{m}^2}$	4
ρ	Density, $\frac{\mathrm{kg}}{\mathrm{m}^3}$	4
V_∞	Freestream Velocity, $\frac{\mathrm{m}}{\mathrm{s}}$	4
H_0	Total Enthalpy, $\frac{\mathrm{J}}{\mathrm{kg}}$	4
c_p	Specific Heat, $\frac{\mathrm{J}}{\mathrm{kg \cdot K}}$	4
T_w	Wall Temperature, K	4
L	Length of Cone, m	4
ν	Kinematic Viscosity, $\frac{\mathrm{m}^2}{\mathrm{s}}$	4
S_T	Start of Transition Location, m	6
M	Mach Number	12
u	Velocity Magnitude, $\frac{\mathrm{m}}{\mathrm{s}}$	12
a	Speed of Sound, $\frac{\mathrm{m}}{\mathrm{s}}$	12
δ	Boundary Layer Height, m	12
Re	Reynolds Number	12
U	Velocity Scale, $\frac{\mathrm{m}}{\mathrm{s}}$	13
L	Length Scale, m	13
τ_w	Wall Shear Stress, Pa	13
c_f	Skin Friction Coefficient	13

Symbol		Page
δ^*	Displacement Thickness, m	13
$u(y)$	Local Velocity in Terms of the Wall Normal Coordinate, $\frac{\text{m}}{\text{s}}$	13
U_∞	Freestream Velocity, $\frac{\text{m}}{\text{s}}$	13
θ	Momentum Thickness, m	14
u_τ	Friction Velocity Based on the Shear Stress, $\frac{\text{m}}{\text{s}}$	15
κ	von Karman Constant	16
X_{SW}	Swallowing Point, m	17
δ_s	Entropy Layer Thickness, mm	18
ξ	Streamwise Coordinate, m	18
T	Temperature, K	20
u	Local Velocity Component, $\frac{\text{m}}{\text{s}}$	28
U	Single Value Mean of Velocity, $\frac{\text{m}}{\text{s}}$	28
u'	Velocity Perturbation from the Mean, $\frac{\text{m}}{\text{s}}$	28
$\psi(x, y, t)$	Stream Function, $\frac{\text{m}^2}{\text{s}}$	28
α	Wavelength of Perturbation, m	28
β_r	Frequency Factor	29
β_i	Amplification Factor	29
c	Phase Velocity of a Wave, $\frac{\text{m}}{\text{s}}$	29
p	Pressure, Pa	30
g	Gravitational Acceleration, $\frac{\text{m}}{\text{s}^2}$	30
T_s	Surface Tension, $\frac{\text{N}}{\text{m}}$	30
z_S	Azimuthal Height, m	30
k_{min}	Minimum Wave Number to Cause an Instability, $\frac{1}{\text{cm}}$	32

Symbol		Page
Re_{Sc}	Schiller Reynolds Number	73
u_k	Velocity at the Top of the Roughness element, $\frac{m}{s}$	74
k	Roughness Element Height, m	74
N	Non-dimensional Number Indicating Instability Growth	75
f	Frequency, Hz	76
$A(s)$	Pressure Fluctuation RMS Normalized by Mean Edge Pressure, Pa	77
$a_0(f)$	Pressure Spectral Amplitude, $\frac{\mathrm{W}}{\mathrm{Hz}}$	77
A_T	Pressure Fluctuation RMS Normalized by Mean Edge Pressure at the Start of Transition, Pa	77
$a_0(f_T)$	Pressure Spectral Amplitude Normalized by Mean Edge Pressure for the Start of Transition Frequency, $\frac{\mathrm{W}}{\mathrm{Hz}}$	77
Δf	Second-Mode Bandwidth, Hz	77
C_1	Empirical Constant for AEDC Hypervelcity Wind Tunnel 9	77
A_{max}	Maximum Amplitude, m	77
N_T	N Factor at the Start of Transition	77
$(Re_t)_\delta$	Reynolds Number for the End of Transition	78
C	Tunnel Test-Section Circumference, m^2	78
C_1	Circumference of a 30.5 $\times$ 30.5 cm tunnel, cm^2	78
C_F	Coefficient of Friction	78
P_N	Pate Noise Parameter	79
P_0	Total Pressure, Pa	91
T_0	Total Temperature, K	91
γ	Ratio of Specific Heats	91

Symbol		Page
R	Specific Gas Constant for Nitrogen, $\frac{\text{J}}{\text{kg}\cdot\text{K}}$	91
c_v	Specific Heat in Constant Volume, $\frac{\text{J}}{\text{kg}\cdot\text{K}}$	92
Δx	Cell Spacing in Streamwise Direction, m	101
k	Wave Number, $\frac{1}{\text{m}}$	101
$\vec{u}_{wall}$	Normal Component of Velocity, $\frac{\text{m}}{\text{s}}$	109
y^+	Wall Distance Units	112
C_f	Coefficient of Friction	112
Δs	Initial Wall Normal Spacing, m	113
Ω	Finite Volume, m^3	116
$\vec{v}$	Velocity Vector	116
$\vec{n}$	Normal Vector	116
dS	Elemental Surface Area, m^2	116
$\vec{f_e}$	External Forces, N	116
$\overline{\overline{\tau}}$	Viscous Stress Tensor	116
E	Total Energy Per Unit Mass, $\frac{\text{J}}{\text{kg}}$	116
H	Total Enthalpy, $\frac{\text{J}}{\text{kg}}$	116
k	Thermal Conductivity Coefficient	116
$\dot{q_h}$	Time Rate of Change of Heat Transfer Per Unit Mass $\frac{\text{W}}{\text{m}^2\cdot\text{kg}}$	116
T_w	Wall Temperature, K	117
q_w	Total Wall Heat Flux, $\frac{\text{W}}{\text{m}^2}$	126
C	Cell Size, m^3	133
N	Total Number of Cells	133
V_i	Volume of a Cell, m^3	133

Symbol		Page
r	Grid Refinement Factor	134
ϕ	Generic Flow Variable	134
$\phi_{ext}^{1,2}$	Extrapolated Value of Generic Flow Variable	134
$e_a^{1,2}$	Approximate Relative Error	135
$e_{ext}^{1,2}$	Extrapolated Relative Error	135
$\mathrm{GCI_{fine}}^{1,2}$	Fine-Grid Convergence Index	135
F_s	Safety Factor	135
dy	Roughness Height, μm	138
$\mathcal{N}$	Random Number Between 0 and 1	138
α_{diss}	Ducros Switch	146
$F_{f,diss}$	Disspative Flux	146
D_f	Dissipative Portion of a Standard Shock Capturing Scheme	146
ω	Vorticity Magnitude, $\frac{\mathrm{rad}}{\mathrm{s}}$	147
ds_0	Spacing of the First Cell Away From the Wall, m	159
ξ	Computation Domain	160
δ	Stretching Function	160
$\bar{P}$	Mean Component of Pressure	168
P'	Fluctuating Component of Pressure	168

List of Abbreviations

Abbreviation		Page
AEDC	Arnold Engineering Development Center	1
CFD	Computational Fluid Dynamics	1
DNS	Direct Numerical Simulation	1
HIFiRE-5	Hypersonic International Flight Research Experimentation Program Flight 5 Vehicle	38
AFOSR	Air Force Office of Scientific Research	40
BAM6QT	Boeing AFOSR Mach 6 Quiet Tunnel	40
RHLNSE	Reduced Harmonic Linearized Navier Stokes Equations	44
AFRL	Air Force Research Lab	44
DREs	Discrete Roughness Elements	53
FDL	Flight Dynamics Laboratory	64
PSD	Power Spectral Density	67
AOA	Angle of Attack	67
RMS	Root-Mean-Squared	77
PSE	Parabolized Stability Equation	77
LST	Linear Stability Theory	81
LES	Large-Eddy Simulation	84
BOLT	Boundary Layer Transition	85
MSW	Modified Steger-Warming	117
MUSCL	Monotonic Upwind Scheme for Conservation Laws	117
DPLR	Data Parallel Line Relaxation	117
GCI	Grid Convergence Method	132

Abbreviation		Page
CFL	Courant Friedrichs-Lewy Number	142
KEC	Kinetic Energy Consistent	144
FFTW	Fastest Fourier Transform in the West	149
DFT	Discrete Fourier Transform	149
DoDHPC	Department of Defense High Performance Computers	154

HYPERSONIC BOUNDARY-LAYER TRANSITION DIRECT NUMERICAL SIMULATION AT MACH 10 ON 7° CONE

I. Introduction

Boundary layer transition from laminar to turbulent flow is a complex area of research that is not completely understood. Thus research efforts towards understanding boundary layer transition phenomenon requires simple geometries to isolate the transition inducing mechanisms. The Arnold Engineering Development Center (AEDC) Hypervelocity Wind Tunnel 9 conducted Mach 10 experiments on six, 7° half-angle cones and documented a break with modern modal boundary layer transition theory as the nose radius increased from sharp to blunt. The onset of transition was due to an unknown mechanism but was hypothesized to be caused by distributed surface roughness [59], [62], [79]. Boundary layer transition was inferred through a sustained increase in heat transfer data above laminar calculations. The goal of this research effort was to reproduce the AEDC Tunnel 9 experimental conditions and identify if the cause of transition was due to the distributed surface roughness of the material. Therefore, a computational fluid dynamic (CFD) direct numerical simulation (DNS) with an imposed artificial distributed surface roughness was run on computational models of the AEDC Tunnel 9 test articles.

1 Experimental Background

The AEDC Tunnel 9 conducted Mach 10 experiments on six, 7° half-angle cones of length of 1.55 m, a base diameter of 0.381 m, at zero angle of attack and with a unit Reynolds number of 17 x 10^6 /m [59]. The six nose radii tested were 0.152, 5.08, 9.53,

12.7, 25.4, and 50.8 mm as shown in Figure 1. The onset location of the boundary layer transition was inferred from measurements made with thermocouples mounted on the surface of the model and the boundary layer transition onset location was defined as the first sensor location with a sustained increase in heat transfer above the laminar CFD computations [59].

In Figure 1, Configuration 3 corresponded to the configuration with base diameter of 0.381 m which was consistent across all models used in this research effort [54]. The cones labeled Configuration A had the same forward, middle, and aft conic section with a customized fourth section for the nose radius (R_N). The fourth section for Configuration A had nose radii of 0.152, 5.08, and 9.53 mm [54]. Configuration C corresponded to the nose radius of 12.7 mm while Configuration B corresponded to the bluntest nose radius of 50.8 mm. Configuration B did not use the forward conic section used in Configurations A and C due to the large amount of bluntness in the nose radius [54]. The experimental test articles were fabricated from 15-5 PH stainless steel and the noses were polished to a maximum roughness level 15 μm before each run [59]. This level of roughness was used as the maximum amplitude of the distributed roughness height in the DNS calculations.

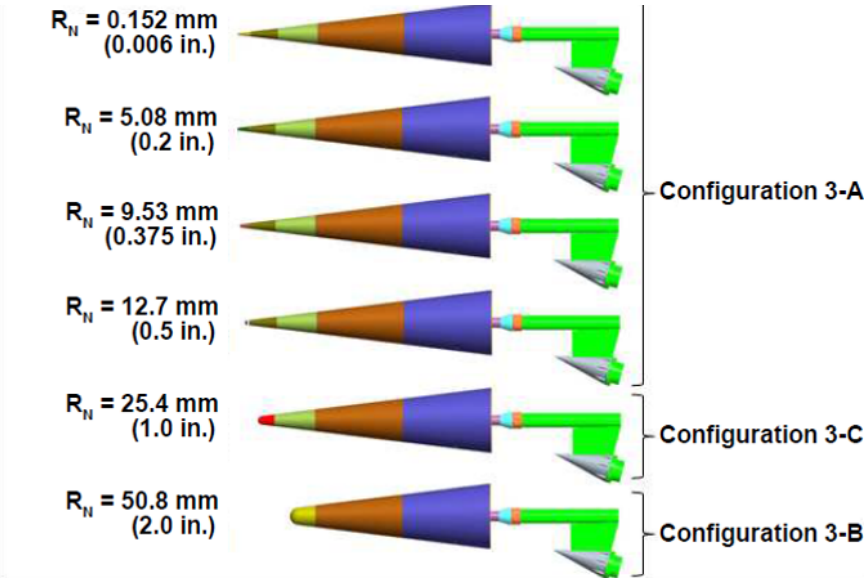

Figure 1. AEDC Tunnel 9 Experimental Configurations for 7° Axi-Symmetric Cones with Increasing Nose Radii [54]

2 Departure from Modern Modal Transition Theory

The boundary layer transition onset location data from the cones with the three most blunt nose radii (12.7, 25.4, and 50.8 mm) indicated a departure from the modern modal transition theory. The cause of transition on the 7° half-angle cones with nose radii of 12.7, 25.4, and 50.8 mm was determined to be non-modal because the symmetrical, non-flared geometry of the conics precluded Görtler instabilities or crossflow instabilities as the cause of transition. Additionally, the Mach number was above the range where first mode instabilities would be dominant and the pressure power spectral density calculations performed by Moraru revealed no indication of second mode domination for the three most blunt nose radii [59]. For the three least blunt nose radii (0.152, 5.08, and 9.53 mm), the boundary layer transition was dominated by second mode instabilities.

The established precedent for second mode dominated transition was that the transition location would move aft on the geometry as the nose radius was increased

[72]. Figure 2 presents the heat transfer data for the six, 7° half-angle cones used in the AEDC Tunnel 9 experiments where the streamwise location (s) was plotted against the Stanton number (St) multiplied by the square root of the Reynolds number based on the cone length (Re_L). The Stanton number is a nondimensional number which measured the rate of heat transfer to thermal capacity and is defined as

$$St = \frac{\dot{q}}{\rho V_\infty (H_0 - c_p T_w)} \tag{1.1}$$

where $\dot{q}$ was the heat transfer per unit area, ρ was the freestream density, V_∞ was the freestream velocity, H_0 was the total enthalpy in the flow, c_p was the specific heat of the fluid, and T_w was the wall temperature. The Reynolds number was a nondimesional measure the ratio of the viscous to inertial forces defined as

$$Re_L = \frac{V_\infty L}{\nu} \tag{1.2}$$

where V_∞ was the freestream velocity, L was the length of the cone, and ν was the kinematic viscosity of the fluid.

The Sharp Nose label in Figure 2 corresponded to the cone with the nose radius of 0.152 mm and demonstrated a clear example of a second mode dominated transition profile. In the Sharp Nose case, the lowest heat transfer rates occurred during the laminar portion of the flow detected by the first three sensors, represented as the red dots in Figure 2. When transition onset occurred around 0.25 m, the heat transfer rate drastically increased due to the mechanical energy in the flow which was attributed to the formation of turbulent eddies which dissipated as heat [90]. Subsequently, as fully turbulent flow developed around 0.4 m, the heat transfer rate decreased slightly due to continual streamwise boundary layer thickening but the heat transfer rate in the fully turbulent region remained higher than those of the laminar flow.

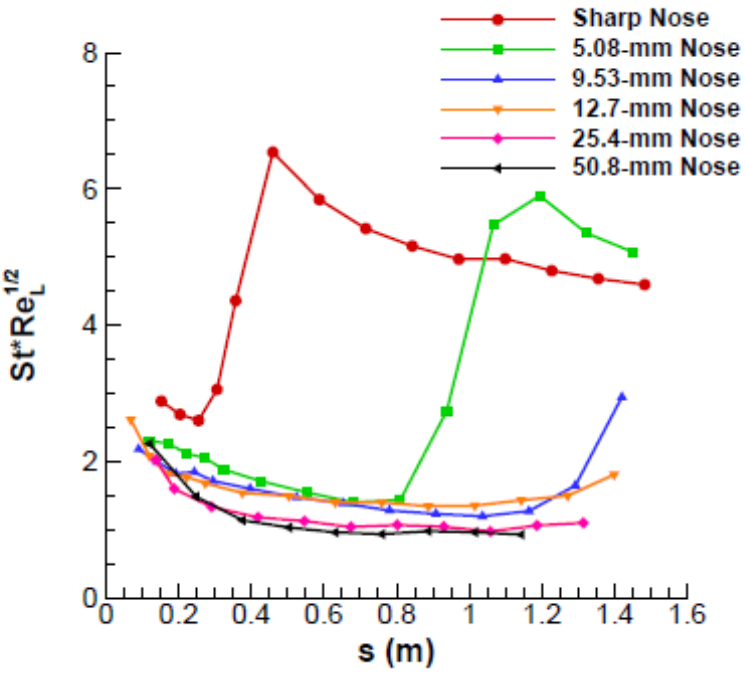

Figure 2. Heat transfer profiles for varying nose radii at Mach 10 and zero angle of attack with Re = 15×10^6 /m (sharp nose) and Re = 17×10^6 /m (blunt nose) (used with permission) [59]

As the nose radius increased from 0.152 to 5.08 mm, the appearance of second mode instabilities was delayed and as a result, the transition location was also delayed to a downstream location on the blunt cone [63]. The comparison between the Sharp Nose case with the 5.08 mm case in Figure 2 clearly exemplified the delay in transition onset location of the established second mode dominated transition trend. As the nose radius increased from 5.08 to 9.53 mm the transition location continued to move downstream, but fully turbulent flow was no longer achieved. However, as the nose radius increased from 9.53 to 12.7 mm the downstream movement of the transition location was barely perceived [63]. This negligible change in transition location indicated that the transition location had deviated from the established second mode dominated precedent for modal transition. Furthermore, at a nose radius of 12.7 mm the start of transition occurred prior to the detection of second

mode instabilities [63]. Therefore another physical phenomena besides second mode instabilities was the catalyst for the onset of transitional flow for the 12.7 mm nose radius case. The heat transfer profiles of the cones with the nose radii of 25.4 and 50.8 mm fell into the unexplained regime behavior exhibited by the cone with the nose radius of 12.7 mm. The thermocouples were placed 0.05 m apart and this spacing was the largest source of uncertainty in the experimental measurements of the transition onset location but was not enough uncertainty to account for this transition reversal phenomena.

In Figure 3, a laminar CFD line provided reference to where the heat flux levels rose above laminar flow conditions thus indicating transitional flow. All nose radii cases for the experimental research effort started out as laminar and matched the laminar CFD solution computed by Moraru [59]. Additionally seen in Figure 3, all nose radii cases the heat transfer profiles increased above the laminar CFD values thus implicating transitional flow occurred for all nose radii cases. The laminar solution does not predict transition but it does serve as a baseline for matching laminar flow conditions at the beginning of the geometry and identifying when the heat transfer data has begun to monotonically increase.

The start of transition location (S_T) was labeled in Figure 3 by Moraru and was determined by the first sensor which measured a sustained increase in heat transfer data [59]. In Figure 3a, the start of transition was much more evident than in Figures 3b - 3d because the slope of the transition region in Figure 3a was much more dramatic due to the second mode dominated nature of the 9.53 mm nose radius case. The heat flux definitively increased above the laminar line for the blunter nose radii in Figures 3b - 3d but the heat transfer profiles did not match traditional heat profiles for second mode dominated transition. The heat transfer data in the three most blunt cases increased with a gradual slope, thus the identification of the start of transition

location became subjective and the labeled start of transition locations for Figures 3b - 3d are viewed as estimations by the present author.

2.1 Problem Statement.

The boundary layer transition data of the cones with the three most blunt nose radii indicated that the cause of transition was non-modal as it did not conform to modern modal transition theory. Since boundary layer transition outside of modern modal theory remains largely unexplained, the purpose of this research effort is to determine if the non-modal transition observed in the AEDC Tunnel 9 experiments was due to surface roughness through DNS CFD calculations. From the experimental results shown in Figure 2, a DNS was run on the 9.53 and 12.7 mm nose radii cases with distributed surface roughness. The nose radius of 9.53 mm served as the control case to compare to the results of the 12.7 mm case where non-modal transition was observed.

Modern modal boundary layer transition theory considers four types of instabilities in the boundary layer transition: the centrifugal instabilities commonly referred to as Görtler instabilities, the three-dimensional crossflow instabilities, and the first and second Mack mode instabilities [70]. Additionally, the entropy layer contains instabilities which interact with the boundary layer. Flowfield instabilities of any origin are not mutually exclusive within a flowfield. Instabilities are the form of the forcing factor that causes transition to occur within the boundary layer if the receptivity process is favorable. While the instabilities are the mechanisms to cause transition; there are many additional factors which influence the rate at which transition occurs and the transition onset location. The influencing factors include roughness, freestream noise, curvature, bluntness, wall heating and cooling, suction and blowing, angle of attack, and many more. The influencing factors are not additive in effect [8]. Therefore

systematic study of each influencing factor as well as each combination of influencing factors is required for a full understanding of boundary layer transition. For the present research effort it is hypothesized that proper simulation of distributed surface roughness will yield qualitatively similar results to the experimental data. This hypothesis in bolstered by the successful results of Dinzl's research effort on the effects of distributed surface roughness on crossflow instabilities [21]. Distributed surface roughness is believed to be the likely cause of the non-modal transition behavior described in Section 2 but other influencing factors could have contributed to the phenomenon.

Boundary layer transition experiments which provide information on the location of the breakdown of laminar flow and alone can provide only limited information regarding the fundamental questions involving the roles of the dominant instabilities. However, they can provide guidance and assistance for future stability experiments and analytical stuides, which hopefully can provide more complete answers [79]. In much of the same sentiment, the goal of this research was to further the collective academic understanding of boundary layer transition by determining if the cause of the increased heat transfer data provided by the AEDC Tunnel 9 experiments on the 7° half-angle cones of increasing nose radii was due to distributed surface roughness.

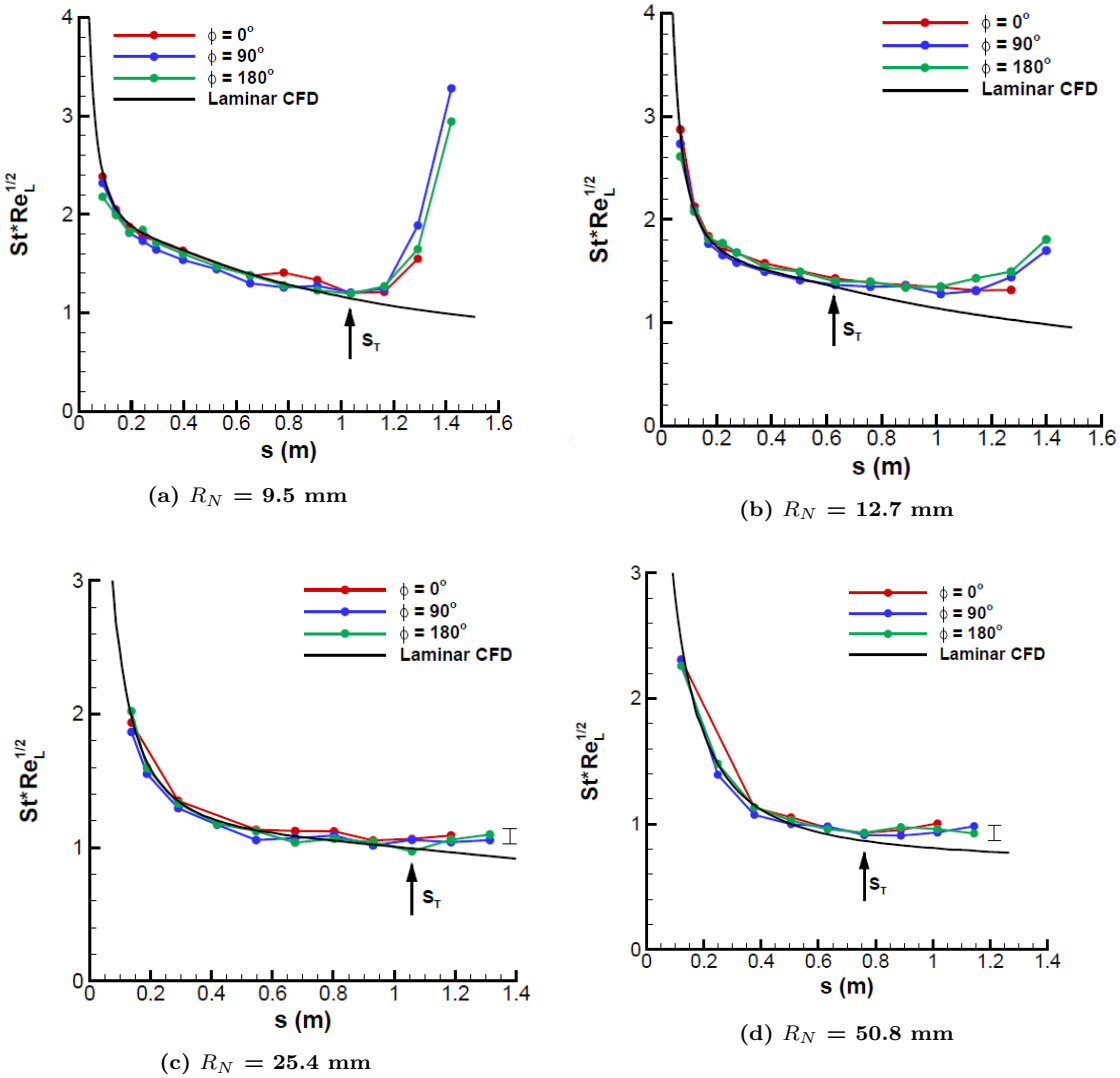

(a) R_N = **9.5 mm**

(b) R_N = **12.7 mm**

(c) R_N = **25.4 mm**

(d) R_N = **50.8 mm**

Figure 3. Laminar Heat Transfer Data and Experimental Heat Transfer Data at Re = 17×10^6 **/m for blunt nose radii (used with permission) [59]**

3 Overview of Subsequent Chapters

The present research effort begins with a survey of the relevant literature in Chapter 2 where highlighted aspects of hypersonic aerodynamics and boundary layer transition theory are presented. The research methodology presented in Chapter 3 detailed the instability resolution case study which drove the grid formation, the CFD DNS smooth wall computational set up and results, as well as the process to obtain the grids which simulated distributed surface roughness on the 7° half-angle cones with the nose radii of 9.53 and 12.7 mm. The results of the DNS with distributed roughness grids are revealed in Chapter 4 for rigorous scientific analysis. All concluding remarks pertaining to the research and suggestions for future research related to the current effort and incorporating of emerging technologies are presented in Chapter 5.

II. Literature Review

The Arnold Engineering Development Center (AEDC) Hypervelocity Wind Tunnel 9 performed experiments on six, 7° half-angle cones at Mach 10. The boundary layer transition onset location data from the experimental results revealed an unexplained deviation from modern modal theory as the nose radius increased from sharp to blunt. In attempts to interpret the experimental data, a direct numerical solution (DNS) was performed with grids simulating distributed roughness for the cones with the nose radii of 9.53 mm and 12.7 mm. In support of both the experimental data and the computational data presented in Chapter 4, it was essential to understand all the fundamental boundary layer theory and the current research in boundary layer transition and instabilities. First, presented in Sections 1 and 2, is an exploration of the basic characteristics of hypersonic aerodynamics which pertain to the current research application and an overview of the path to turbulence from laminar flow. Section 3 provided a current understanding of stability theory. Then, in Section 4, the mechanisms that cause transition to turbulence are discussed with the understanding that when dealing with unexplained phenomenon it is essential to understand modern modal mechanisms to transition. Section 5 pragmatically isolated factors that influence transition to occur and explores each factor individually. The current research methodology for boundary layer transition prediction are examined in Section 6. Finally, Section 7 established a CFD lexicon and base understanding of highlighted concepts that influenced modeling decisions made in Chapter 3.

1 Characteristics of Hypersonic Flight

The differences between hypersonic aerodynamics and subsonic or supersonic aerodynamics are stark. The aerodynamic flow regimes are often defined in terms of Mach

number. Mach number (M) is the ratio of the velocity (u) to the speed of sound (a).

$$M = \frac{u}{a} \tag{2.1}$$

Hypersonic flow is often defined as flow with Mach 5 or higher. Yet a more appropriate definition of the hypersonic regime is the regime where certain physical flow phenomena become progressively more important as the Mach number was increased to higher values [3]. Many assumptions that are assumed for the lower Mach number regimes are no longer valid in the context of hypersonics. For example, incompressibility can no longer be assumed and constant flow properties throughout the flow field are no longer upheld. Thus defining Mach 5 as the hypersonic flow regime is not an immutable rule. A brief description of applicable hypersonic physical flow phenomena is provided in the subsequent sections.

1.1 Boundary Layer.

A hydrodynamic boundary layer or velocity boundary layer is defined as the region in the fluid where a velocity gradient exits due to the no-slip boundary condition at the geometry wall and the freestream boundary condition at the top of the domain. A boundary layer occurs at any Mach number because the only requirement for boundary layer fomation is a velocity differential [6]. The boundary layer is characterized by a large velocity gradient normal to the wall and the viscous forces or frictional forces proportionally determine the values of viscous shear stress in the flow. The velocity differential which influences the boundary layer height (δ) is governed by the Reynolds number (Re).

$$Re = \frac{UL}{\nu} \tag{2.2}$$

In Equation 2.2, U is a velocity scale, L length scale, and ν is the kinematic viscosity. The velocity scale and the length scale are selected based on the application. For the current application, the velocity scale was the freestream velocity and the length scale was the length of the cone. The Reynolds number is an important nondimensional parameter because it yields a ratio of the viscous to inertial forces in the flow. Increasing the Reynolds number also decrease the wall shear stress (τ_w) and skin friction coefficient (c_f).

The boundary layer describes the region defined by a velocity gradient between the no-slip wall boundary condition and the freestream velocity. There is no unique boundary layer thickness since the effect of the viscosity in the boundary layer decreases asymptotically towards the freestream values [69]. Hence, the boundary layer height is often described as the distance required for the velocity gradient to reach 99% of the freestream value. Defining the boundary layer height in terms of 99% of the freestream value would require measurements of very small velocity differences; accordingly, it is admissible to use the displacement thickness and momentum thickness integrals to characterize the boundary layer [64]. The displacement thickness (δ^*) for incompressible flow is the thickness by which the inviscid outer flow is displaced outwards by the boundary layer [69].

$$\delta^* = \int_0^\infty \left(1 - \frac{u(y)}{U_\infty}\right) dy \tag{2.3}$$

Where $u(y)$ is the local velocity in terms of the wall normal coordinate, and U_∞ is the freestream velocity. In Figure 4, the velocity profile in the freestream has equal magnitude streamlines. However, once the boundary layer begins to form the velocity profile changed to reflect the no-slip boundary condition at the wall and the freestream boundary condition at the top of the boundary layer.

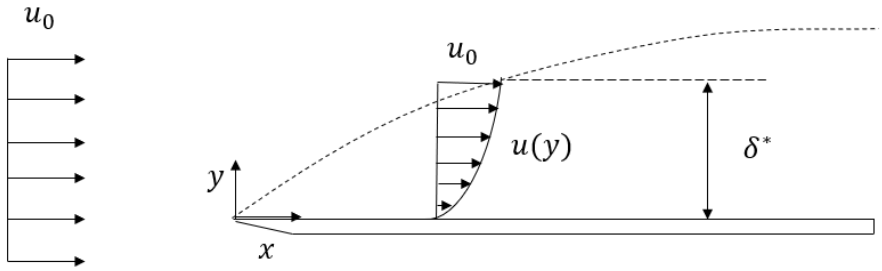

Figure 4. Boundary Layer Schematic Adapted From [90]

The momentum thickness (θ) for incompressible flow is the height required for the amount of momentum in the boundary layer relative to that in the inviscid flow [69].

$$\theta = \int_0^\infty \frac{u(y)}{U_\infty}\left(1 - \frac{u(y)}{U_\infty}\right)dy \tag{2.4}$$

The momentum thickness equations provided in Equation 2.4 implies a smaller magnitude than the displacement thickness because of the fractional velocity term in front of the displacement thickness term. Thus, the momentum thickness has a similar shape when applied to the flat plate case of Figure 4 but a smaller magnitude.

By characterizing the boundary layer through the displacement thickness, the state of the flow inside the boundary layer can be characterized as laminar or turbulent because the hydrodynamic boundary layer height changes significantly between laminar and turbulent flow. The boundary layer height for a laminar flow is less than the boundary layer height for turbulent flow because the laminar flow is composed of ordered streamlines and the turbulent flow is composed of vortical structures [6]. Figure 5 demonstrates that as the orderly streamlines of laminar flow breakdown into stochastic vortical structures of turbulence, the displacement thickness increases accordingly.

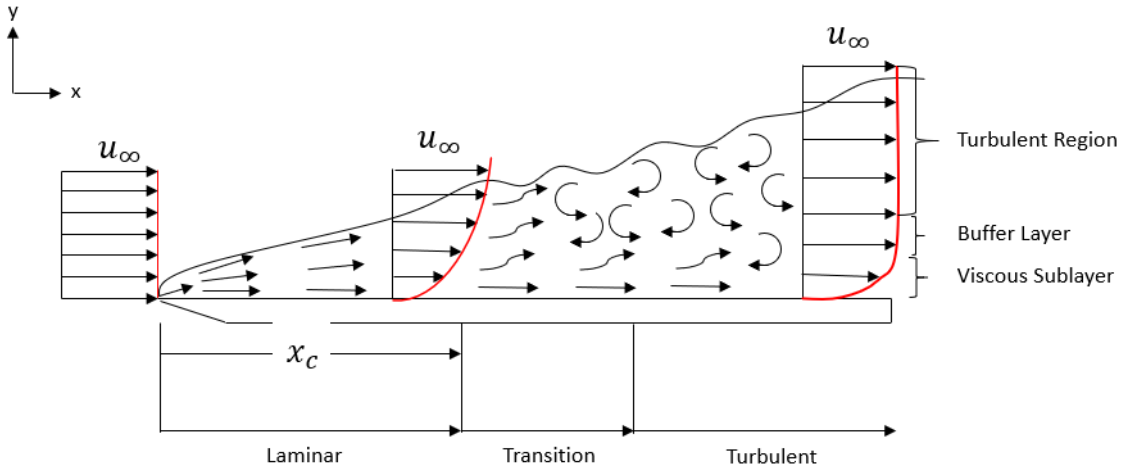

Figure 5. Laminar to Turbulent Boundary Layer Schematic Adapted from [6]

Figure 6 describes the three regions of a turbulent boundary layer: a viscous sub-layer, a buffer layer, and a velocity defect layer. The demarcation of each region is defined in terms of nondimensional wall distance units (y^+),

$$y^+ = \frac{yu_\tau}{\nu} \tag{2.5}$$

where y is the wall distance, ν is the kinematic viscosity, and u_τ is the friction velocity based on the shear stress (τ).

$$u_\tau = \sqrt{\frac{\tau}{\rho}} \tag{2.6}$$

The viscous sub-layer extends from the geometry wall to a $y^+ = 10$. Klebanoff proved that 85% of the total dissipation takes place within the viscous region and the production of turbulent energy is at the maximum value in the viscous region [37]. Thus using the concept of local isotropy in the region near the wall is a poor model [37]. The buffer layer obeys the profile

$$u^+ = \frac{1}{\kappa}\ln(y^+) + C \tag{2.7}$$

where u^+ is the velocity normalized by the friction velocity based on shear stress (u_τ), κ is the von Karman constant, and C is a constant with the value of approximately 5.2 depending on the application. The buffer layer is represented by the linear dashed line in Figure 6. The region between the buffer layer and the top of the boundary layer is referred to as the velocity wake or defect layer. The velocity wake or defect layer includes influencing inertial effects of the fully turbulent flow above the boundary layer edge [41].

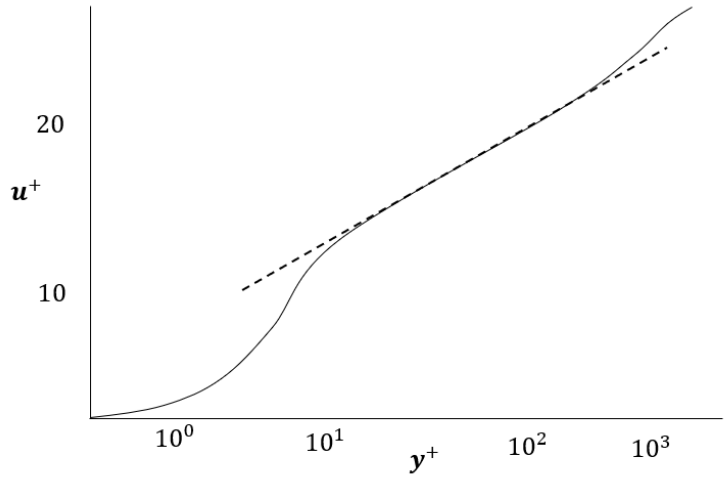

Figure 6. Incompressible Boundary Layer Expressed in Wall Units Adapted from [41]

1.2 Entropy Layers.

Entropy is defined as the energy within a system which is unavailable for use as mechanical work and is commonly referred to as the degree of randomness in a system [61]. For steady, laminar freestream flow the entropy is assumed to be a single value for all streamlines. For unsteady flow applications, the Second Law of Thermodynamics states that entropy will increase over an irreversible process [61]. Figure 7 depicts freestream streamlines of constant entropy passing through a bow shock, an irreversible process, which formed in front of a blunt body. The Streamlines

a, **b**, and **c** increased in entropy after encountering the irreversible process of a shock. However, Streamline **a** encountered a normal shock thus the magnitude of the entropy increase was the largest in Streamline **a**. Streamlines **b** and **c** encountered a weaker, oblique shock and therefore the magnitude of the entropy increase in Streamline **b** was less than the magnitude of entropy increase in Streamline **a** and so forth for Streamline **c** [4]. Effectually, a gradient of entropy levels was created on the streamlines between the geometry and the bow shock. Collectively these entropy levels are referred to as the entropy layer.

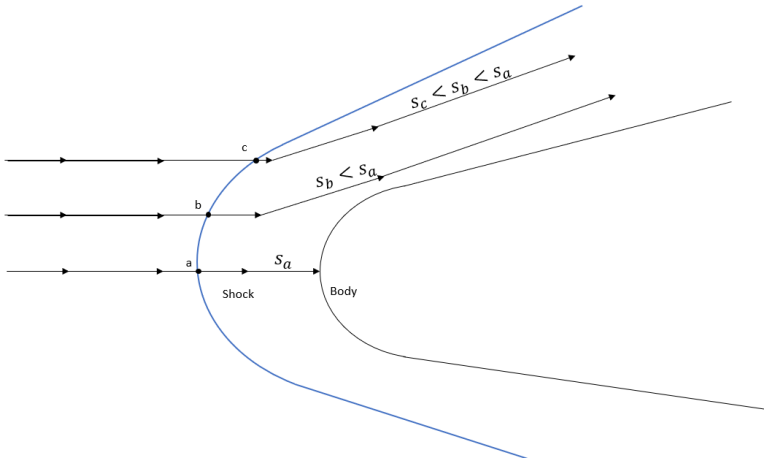

Figure 7. Entropy Gradient Schematic Adapted from[4]

The blunt cone geometry depicted in Figure 8 demonstrates that at the start of the blunt nose cone geometry the entropy layer is much larger than the boundary layer. Yet the boundary layer continues to grow in height along the streamwise direction of the geometry as discussed in Equation 2.3 and eventually the boundary layer height increases to "swallow" or entrain the entropy layer. The streamwise point at which this swallowing occurs is referred to as the swallowing point indicated in Figure 8 by X_{SW}. Before the swallowing point, the boundary layer is comprised of streamlines that encountered the normal shock and experienced a high increase in entropy. Post the swallowing length, the boundary layer continues to grow and

becomes split between the high and low entropy regions. Figure 8 has two streamlines represented by arrowhead lines. The bottom streamline encountered a normal shock and enters the boundary layer with high entropy. The top streamline is the last streamline to enter the boundary layer at the swallowing point and therefore functions as the dividing streamline between the high and low entropy regions of the boundary layer. The streamlines passing through the shock above the top streamline no longer have a large increase in entropy and comprise the low entropy region of the boundary layer after the swallowing length.

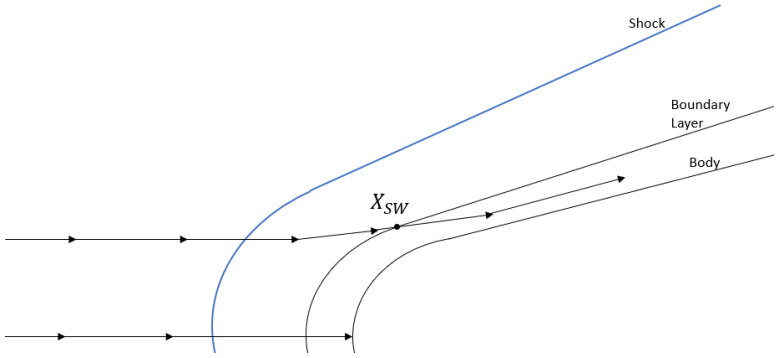

Figure 8. Entropy Layer Schematic Adapted From [79]

The entropy layer and boundary layer change in response to the freestream Reynolds number and the nose radius as demonstrated in Figures 9 and 10 where δ_s, the entropy layer thickness, and δ_h, the boundary layer thickness, are plotted against ξ, the streamwise coordinate for a 7° half-angle blunted cone of length 0.5 m. The onset transition location (ξ_T) for each case was labeled by Paredes et al. by a dot along the streamwise coordinate axis corresponding to the color of the scenario. In Figure 9 the nose radius ($R_{N,S}$) was 1.524 mm with the unit Reynolds numbers of $Re_{\infty,S} = 30.5 \times 10^6$ m^{-1}, $Re_{\infty,M} = 61.0 \times 10^6$ m^{-1}, and $Re_{\infty,L} = 91.5 \times 10^6$ m^{-1}. As the Reynolds number was increased the boundary layer thickness was reduced due to the increased inertial forces to viscous forces. Ultimately, this phenomena lead

to a longer swallowing length because the boundary layer required mode streamwise distance to rise in height to fully swallow the entropy layer. As the Reynolds number was increased, the transition location moved forward on the cone.

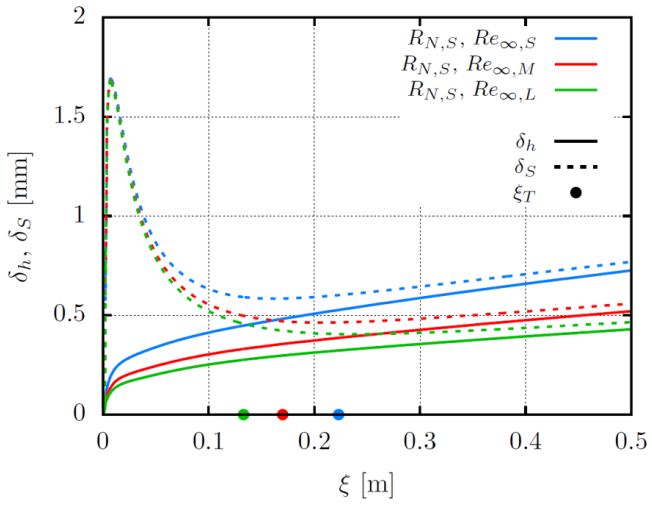

Figure 9. Boundary Layer and Entropy Layer Thickness with Constant Nose Radius and Increasing Freestream Reynolds Number [62]

In Figure 10, the nose radii considered were $R_{N,S} = 1.524$ mm, $R_{N,M} = 2.540$ mm, and $R_{N,L} = 5.080$ mm with a constant Reynolds number of $Re_{\infty,L} = 91.5 \times 10^6$ m^{-1}. As the nose radius increased, the boundary layer grew in a very slight amount. However, as the nose radius increased the entropy layer drastically increased. In the most blunt case, the swallowing length exceeded the length of the cone due to the increase in entropy layer thickness [62]. In Figure 10, the onset transition location conformed to modal transition theory by moving downstream as the nose radius increased.

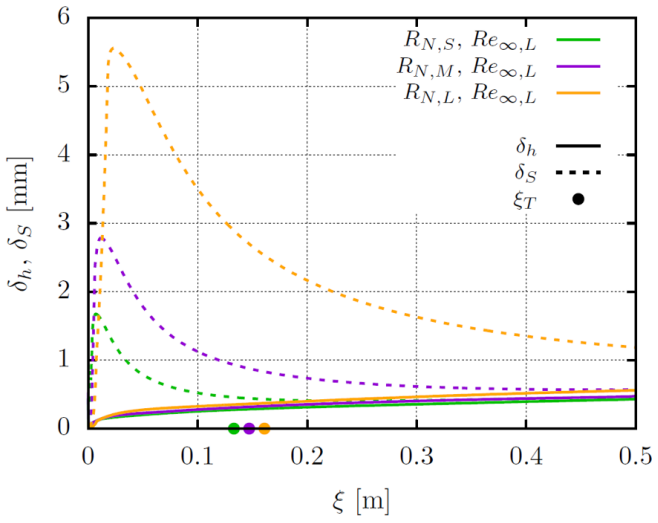

Figure 10. Boundary Layer and Entropy Layer Thickness with Increasing Nose Radius and Constant Freestream Reynolds Number [62]

The entropy layer is a region of strong vorticity [4]. The relationship between entropy and vorticity for steady flow is provided by Crocco's Theorem

$$T\nabla s = \nabla h_0 - \mathbf{V}\mathrm{x}(\nabla \mathrm{x}\mathbf{V}) \tag{2.8}$$

where T is the temperature, ∇s is the entropy gradient, ∇h_0 is the total enthalpy gradient, and $\nabla \mathrm{x}\mathbf{V}$, or the curl of the velocity, is the vorticity. For a complete derivation of Crocco's Theorem see Reference [2]. In Figure 8, the flow over the blunt cone was assumed adiabatic thus implying that the enthalpy gradient (∇h_0) was zero. Thus since the Second Law of Thermodynamics dictates that the entropy increases over a shock, then Crocco's Theorem dictates that vorticity also increases and is a nonzero value.

Crocco's Theorem proved that vorticity exists in the entropy layer. However the effect that this vorticity in the entropy layer has on boundary layer stability post the swallowing point is not well understood [30]. In 1967, Stetson and Rushton

performed Mach 5.5 shock tunnel experiments and found that as bluntness increased the transition location generally moved aft on the geometry [81]. Similar to the AEDC Tunnel 9 experiments, Stetson and Rushton found that as the nose bluntness increased past a certain point, the second mode dominated transition precedent of the transition location moving aft on the cone as the nose radius increased ceased to be upheld and the transition location began to move forward on the geometry [81]. Stetson and Rushton hypothesized that this transition reversal is an effect of the interaction between the entropy and boundary layers [81].

In 1984, Stetson et al. made instability measurements via hot wires on a 7° half-angle cone in Mach 8 flow [82]. These measurements followed an instability from inside the entropy layer until the swallowing distance. Stetson et al. discovered that the entropy layer disturbance amplitude grew outside the boundary layer and then the amplitude reduced as the instability was swallowed by the boundary layer [82]. For an instability to exist there must be a generalized inflection point, or local maximum in the angular momentum [65] and in the Stetson et al. 7° half-angle cone experiments, the maximum amplitude of the disturbances aligned with the inflection point in the flowfield velocity profile [82].

Malik et al. attempted to numerically reproduce the data seen in the Stetson 7° half-angle cone experiments via the e^N method described later in Section 6.2. The results were successful in reproducing the qualitative trends of the 1984 Stetson et al. experiments; however, the calculated growth rates were larger than the experimental data [51]. Model calculations of the entropy layer and boundary layer interaction has proven difficult and no current mathematical model encompasses all of the relevant physics to reproduce a quantitatively accurate results.

It is debatable if the entropy layer disturbances measured by Stetson et al. led to transition. In 2007, Hein calculated weakly amplified disturbances inside the entropy

layer at the same frequency as the disturbances measured by Stetson et al [33]. From these calculations Hein hypothesized that the amplification rate of the entropy layer instabilities were too small to cause transition [33]. Since the AEDC Tunnel 9 experiments with nose radii of 12.7, 25.4, and 50.8 mm did not see fully transitioned flow it is possible that the cause for the increased heat transfer data seen in Figure 3 was due to the entropy layer and boundary layer interaction. Foundational investigation into entropy layer instabilities was performed by Dietz and Hein [19] and Fedorov and Tumin [26] for the flat plate case and was applied to blunted cone geometries by Paredes et al. [62]. Paredes et al. observed no amplified entropy layer modes [62]. Therefore, this explanation for the onset of turbulence was excluded from this research effort.

2 Transition to Turbulence

Reynolds laid the foundation of the laminar to turbulent transition research via the water tube experiments which proved that under certain controlled conditions, flow changed from laminar to turbulent [66]. The term transition is used to refer to the process in which laminar flow transitions into turbulent flow. Since the Reynolds water tube experiments, significant steps have been taken towards understanding the transition process but this complex process is still not completely understood.

In order for the transition process to begin, an influencing forcing factor must exist within the domain. The forcing factor is either steady or unsteady. Unsteady forcing factors include changing disturbances like freestream noise and steady forcing factors include constant disturbances like surface roughness [20]. In the presence of a forcing function, the receptivity process dictates if transition occurs. Receptivity is the process by which disturbances enter the boundary layer and create the initial conditions for an instability [68]. The receptivity process for hypersonic boundary

layers is influenced by many factors including ablation, waviness, bluntness, curvature, and Mach number [76]. Assuming receptivity is favorable for instability growth, the path to transition continues based on the initial disturbance amplitude and the conditions within the flowfield.

White described the transition to turbulence via seven distinct steps starting with the existence of stable laminar flow [90]. White's process is depicted for a flat plate in the schematic shown in Figure 11. Due to the influencing forcing factor in the domain, unstable two-dimensional Tollmien-Schlichting waves begin to appear in the second of White's steps. The Tollmien-Schlichting waves were named after the two men who predicted sinusoidal velocity fluctuations in laminar flow over a flat plate in the 1920s [77]. The breakthrough experiments of Schubauer and Skramsted revealed the previously unseen sinusoidal fluctuations in the laminar boundary layer which were predicted by Tollmien and Schlichting. The second milestone discovery in the Schubauer and Skramsted experiments was the conclusion that the waves increased in amplitude as they traveled downstream. This amplification was indisputable evidence that the Tollmien-Schlichting waves were the cause, not the effect, of transition [49]. The key requirement in the Schubauer and Skramsted experiments to observe the sinusoidal waves was the reduction of the freestream turbulence to 0.03% [77]. This level of freestream turbulence was much lower than previous transition experiments and was more realistic of the turbulence levels at the altitude at which flight occurs than the previous experiments.

The Orr-Sommerfeld is discussed in Section 3. However, the eigenvalues of the Orr-Sommerfeld Equation described the Tollmien-Schlichting waves observed in the flat plate experiments of Schubauer and Skramsted [34]. However, the Orr-Sommerfeld Equation is valid under parallel flow conditions. Therefore, if disturbances were introduced when the parallel flow assumption was not valid then linear stability would

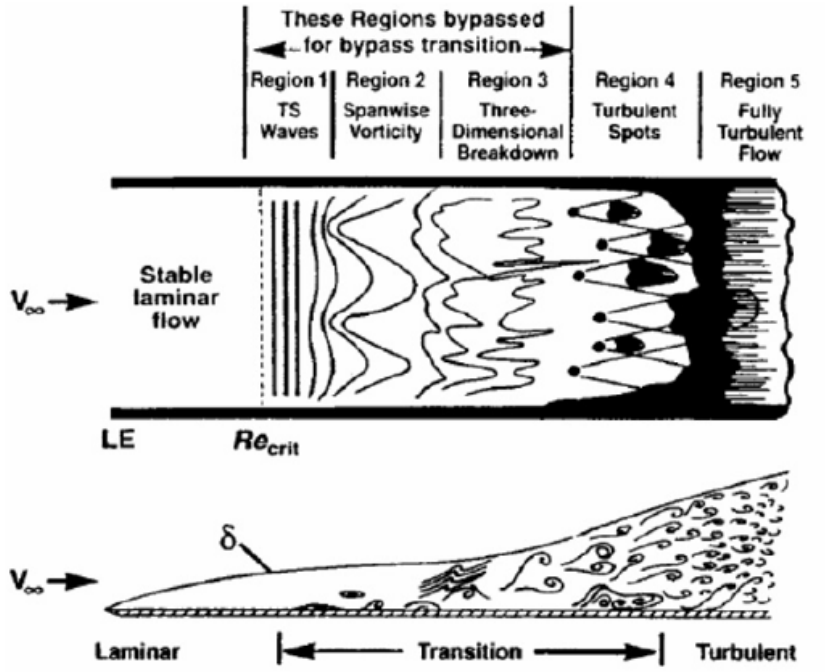

Figure 11. Boundary Layer Transition on Flat Plate (used with permission) [89]

fail to predict transition accurately by predicting transition at much lower Reynolds numbers than observed [34]. The difference between the two cases, parallel flow or not, lies in the role of the receptivity mechanism. When an instability is introduced in a region where parallel flow is a poor assumption, the instability travels downstream in accordance with the unsteady boundary layer equation until a region of parallel flow and then is amplified or damped according to linear stability theory [34]. The method of matched asymptotic expressions was shown to solve the unsteady boundary layer equation for the same Tollmien-Schlichting wave solution as the Orr-Sommerfeld Equation for regions of parallel flow [34]. This method was then successfully expanded to regions of non-parallel flow in Reference [34].

White's next two steps in transition shown in Figure 11 are the development of three-dimensional unstable waves and hairpin eddies followed by the vortex breakdown in the regions of high localized shear [90]. Next, three-dimensional fluctuations

form through the cascade vortex breakdown. The three-dimensional fluctuations lead into the formation of turbulent spots. Finally, the occurrence of the spots become abundant and the turbulent spots coalescence into fully turbulent flow [90].

When flow experiences all the steps of the transition process distinctly the transition process is described as natural transition. When the forcing functions that cause the transition process to begin have large initial amplitudes, the flow may skip the early stages of transition and move directly to the later steps of transition. This transition process is termed bypass transition. [90]. Specifically, the development of Tollmien-Schlichting waves, development of spanwise vorticity, the three dimensional vortex breakdown are skipped in bypass transition as denoted in Figure 11. Bypass transition begins with the forming and coalescing of turbulent spots to form fully turbulent flow.

For incompressible flow, the transition process is extremely complex due to the multiple possible paths to turbulence. This process becomes more complex for the compressible subsonic flow through the addition of density fluctuations. However, in the compressible subsonic regime, three-dimensional waves are typically ignored. In the supersonic and hypersonic regimes, the three-dimensional waves cannot be neglected [80]. Including the three-dimensional waves makes transition prediction extremely complex [80].

Figure 12 depicts the paths of transition depending on the amplitude of the forcing factor. The assumption in all of these paths to turbulence is that the receptivity is favorable for fostering the growth of an instability. Path A represents the path to turbulence for the smallest environmental forcing functions and Path E represents the path to turbulence for the largest environmental forcing functions. Computational investigation completed by Paredes et al. indicated that as the nose radius increased from the sharp to blunt the path to transition, in accordance to Figure 12, would

change [62]. For sharp nose cones, like the cones with the nose radii of 0.152 and 5.08 mm from the AEDC Tunnel 9 7° half-angle cones, the path to transition was dominated by second mode instabilities and therefore the path to turbulence was represented in Path A of Figure 12. When the nose radius was increased, the onset of second mode instabilities was delayed, as evident in the AEDC Tunnel 9 experiments with the nose radii of 5.08 and 9.53 mm. However, Paredes et al. concluded that cones with moderate bluntness had an initial non-modal instability but this initial non-modal instability was overcome by the modal growth of second mode instabilities later on down the frustum [62]. Thus the path to turbulence continued to follow Path A in Figure 12. For cones with large bluntness values which did not exhibit second mode instabilities, non-modal mechanisms are expected to have initiated transition to turbulence [62]. The AEDC Tunnel 9 7° half-angle cones with the nose radii of 12.7, 24.5, and 50.8 mm did not experience second mode instabilities. Therefore transient growth mechanisms are the likely cause of transition for the three most blunt cases [62]. In Figure 12, Path C represents the path to turbulence for the increased heat transfer data phenomena observed in Figure 2 for the three most blunt cases.

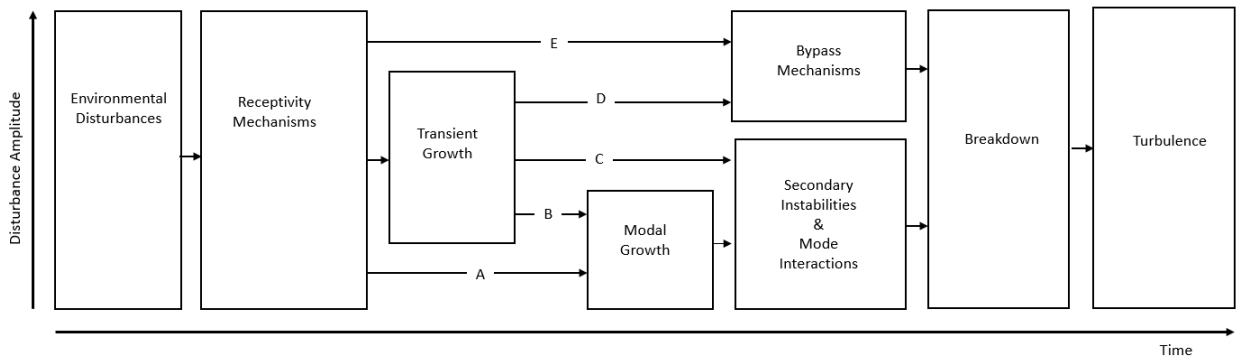

Figure 12. Paths to Turbulence Adapted From [20]

3 Stability Theory

Stability theory aims to indicate whether disturbances in the boundary layer will amplify to transition or dampen and return to fully laminar flow as the disturbances travel downstream [8]. If a disturbance unconditionally dampens out it is considered stable as demonstrated by the first ball in Figure 13. If a disturbance unconditionally grows it is considered unstable like the second ball in Figure 13. The last ball in Figure 13 represents neutral stability. If the neutral system was perturbed by an adequate forcing function then the system would not remain stable. The force required to move the last ball in Figure 13 dictates the initial amplitude necessary to perturb the ball from equilibrium. The boundary layer is a system to which the analogy in Figure 13 applies. The stability of the boundary layer hinges on the forcing function and the receptivity mechanisms. If forcing functions do not exist in the system or the receptivity mechanisms are not favorable for the forcing functions present in the system then the boundary layer is unconditionally stable. For this research effort, the boundary layer was perturbed by the forcing function resulting from distributed surface roughness. If this forcing mechanism is large enough to pass through the receptivity mechanisms then transition to turbulent flow will occur.

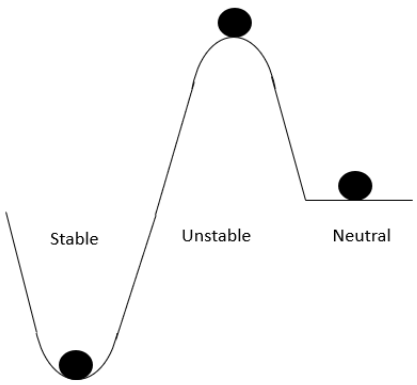

Figure 13. Conditions of Stability Adapted from [87]

Regions of flow can be characterized in a similar manner. For example, the wake region behind a body is usually an unstable region; meaning this region of the flow where perturbations added locally are magnified temporally and spatially and affect the entire flow eventually [69]. Similarly, the boundary layer is a convectively unstable region meaning it is a region where it can be laminar and then when a local perturbation is added to the flow it will convects downstream and no longer affect the original position of the perturbation [69].

3.1 The Orr-Sommerfeld Equation.

The fundamental concept of stability theory hinges on the decomposition of the flow properties into a mean or average component and a perturbation component at each location [64]. For example, the x-component of velocity is decomposed into

$$u = U + u' \tag{2.9}$$

where u is the entire flow velocity component at any given location, U is the single value mean velocity for the entire flowfield, and u' is the perturbation from the mean value at any given location. The other velocity components are decomposed similarly. In most practical fluid dynamic applications, the perturbation magnitude will be less than the magnitude of the mean velocity [69].

If the flow is reduced, for simplicity of analysis, to two dimensional flow then a stream function, $\psi(x, y, t)$, can be used to model the perturbation functions as

$$\psi(x, y, t) = \varphi(y)e^{i(\alpha x - \beta t)} \tag{2.10}$$

where α is related to the wavelength of the perturbation.

$$\beta = \beta_r + i\beta_i \tag{2.11}$$

The term β_r is defined as the frequency factor and β_i is defined as the amplification factor. A negative value of β_i indicates that the instability wave is damped and a positive value of β_i indicates that the instability wave is amplified [69].

The stream function, represented in Equation 2.10, is differentiated in terms of the two dimensional Cartesian directions to obtain the perturbation components of the velocity (u' and v').

$$u' = \frac{\partial \psi}{\partial y} \tag{2.12}$$

$$v' = -\frac{\partial \psi}{\partial x} \tag{2.13}$$

It is useful to represent the two perturbations (u' and v') in terms of the single stream function because the principle of the Continuity Equation is automatically satisfied for the system of equations representing an incompressible flow. These definitions can be substituted into the two dimensional incompressible Navier-Stokes Equations utilizing the parallel flow assumption that there is no mean flow in the spanwise direction (i.e. $V = 0$) and employing the boundary layer approximations to obtain the Orr-Sommerfeld Equation [69].

$$(U - c)(\varphi'' - \alpha^2\varphi) - U''\varphi = -\frac{i}{\alpha Re}(\varphi'''' - 2\alpha^2\varphi'' + \alpha^4\varphi) \tag{2.14}$$

In the Orr-Sommerfeld Equation, $c = \frac{\beta}{\alpha}$ and represents the phase velocity of the wave. Equation 2.14 is a fourth order eigenvalue problem that is dependent on flow conditions and has no dependence on geometry. For a full derivation of the Orr-Sommerfled Equation see Reference [69].

The Orr-Sommerfeld equation can be solved for the line of neutral stability ($c_i =$

0). The behavior of a disturbance is determined based on the Reynolds number defined by the displacement thickness as the reference length and wavelength multiplied by displacement thickness. Equation 2.3 provides the equation for the displacement thickness. Analysis of the Orr-Sommerfeld Equation provided the evidence that the Reynolds number plays a large role in influencing the transition of a flowfield. The Reynolds number can be a useful quantity in stability theory; however, Mack argued that transition is much more complex than single parameter prediction [48]. Fundamentally, the Reynolds number is based on the mean flow therefore, the ability to predict transition based on the calculation of the Reynolds number is doubtful.

3.2 Kelvin-Helmholtz Instability.

The Kelvin-Helmholtz instability occurs in the interface plane when two superposed fluids flow one over the other with velocities flowing in the same direction [14]. The equations of motion to begin the Kelvin-Helmholtz Instability analysis are listed in Equations 2.15 - 2.20, where U is the mean velocity in the x-direction, u is the perturbed velocity in the x-direction per the decomposition method described in Equation 2.9, ρ is density, p is pressure, g is the acceleration due to gravity, and T_s is a surface tension term with a resulting height in the z-direction denoted z_S.

$$\rho\frac{\partial u}{\partial t} + \rho U\frac{\partial u}{\partial x} + \rho w\frac{dU}{dz} = -\frac{\partial}{\partial}\delta p \tag{2.15}$$

$$\rho\frac{\partial v}{\partial t} + \rho U\frac{\partial v}{\partial x} = -\frac{\partial}{\partial y}\delta p \tag{2.16}$$

$$\rho\frac{\partial w}{\partial t} + \rho U\frac{\partial w}{\partial x} = -\frac{\partial}{\partial z}\delta p - g\delta p + \sum_s T_s\left[\left(\frac{\partial^2}{\partial x^2} + \frac{\partial^2}{\partial y^2}\right)\delta z_s\right]\delta(z - z_s) \tag{2.17}$$

$$\frac{\partial}{\partial t}\delta\rho + U\frac{\partial}{\partial x}\delta\rho = -w\frac{d\rho}{dz} \tag{2.18}$$

$$\frac{\partial}{\partial t}\delta z_s + U_s\frac{\partial}{\partial x}\delta z_s = w(z_s) \tag{2.19}$$

$$\frac{\partial u}{\partial x} + \frac{\partial v}{\partial y} + \frac{\partial w}{\partial z} = 0 \tag{2.20}$$

Equations 2.15 and 2.16 are the equations for the components of velocity (u and v) in the x and y directions. Equation 2.17 is the w component of velocity in the z direction with allowance for surface tension at the interface between the fluids. Equation 2.19 is the resulting height term in the z-direction when surface tension is considered. Continuity is represented in Equation 2.20. If the disturbance is given the following form,

$$\exp\, i(k_x x + k_y y + nt) \tag{2.21}$$

where k_x, k_y, and n are constants, then Equations 2.15 - 2.20 can be rewritten as the following exercising the shorthand notation $D = d/dz$.

$$i\rho(n + k_x U)u + \rho(DU)w = -ik_x\delta p \tag{2.22}$$

$$i\rho(n + k_x U)v = -ik_y\delta p \tag{2.23}$$

$$i\rho(n + k_x U)w = -D\delta p - g\delta\rho - k^2 \sum_s T_s \delta z_s \delta(z - z_s) \tag{2.24}$$

$$i(n + k_x U)\delta\rho = -wD\rho \tag{2.25}$$

$$i(n + k_x U_s)\delta z_s = w_s \tag{2.26}$$

$$i(k_x u + k_y v) = -Dw \tag{2.27}$$

Through equation manipulation and proper boundary condition application presented in detail in Reference [14], a single equation is obtained for the disturbance solution.

$$(n+k_xU)(D^2-k^2)w - k_x(D^2U)w - gk^2\frac{D\rho}{\rho}\frac{w}{n+k_xU} + \frac{D\rho}{\rho}[(n+k_xU)Dw - k_x(DU)w] = 0 \tag{2.28}$$

The roots of Equation 2.28 are given by

$$n = -k_x(\alpha_1 U_1 + \alpha_2 U_2) \pm \left[gk\left((\alpha_1 - \alpha_2) + \frac{k^2 T}{g(\rho_1 + \rho_2)} \right) - k_x^2 \alpha_1 \alpha_2 (U_1 - U_2)^2 \right]^{\frac{1}{2}} \quad (2.29)$$

where $\alpha_1 = \frac{\rho_1}{\rho_1+\rho_2}$ and $\alpha_2 = \frac{\rho_2}{\rho_1+\rho_2}$ with ρ_1 and U_1 being the density and x-direction velocity of the lower fluid and ρ_2 and U_2 being the density and x-direction velocity of the higher fluid. If the surface tension terms are neglected then

$$k_{min} = \frac{g(\alpha_1 - \alpha_2)}{\alpha_1 \alpha_2 (U_1 - U_2)^2} \quad (2.30)$$

where k_{min} is the minimum wave number that will cause an instability. The surface tension terms would have had a stabilizing effect if they had been carried throughout the entire analysis [14]. The importance of Equation 2.30 is the statement that an instability occurs if there is any difference between the x-direction velocities in an inviscid flow. With regards to this analysis Helmholtz stated "every perfect geometrically sharp edge by which a fluid flows must tear it asunder and establish a surface of separation, however slowly the rest of the fluid may move" [14]. Entropy layer instabilities are an inviscid phenomenon [31]. Thus when considering blunt nose cone geometries, like the six 7° cones with increasing nose radii from AEDC Tunnel 9, there was a difference in the x-direction velocities by nature of the aerodynamics, instabilities were inherently present in the flowfield.

4 Mechanisms to Turbulence

A laminar boundary layer is the dispersive medium that fosters the propagation of instability waves [49]. Thus, the instabilities are the mechanisms that cause transition in the boundary layer. The four established instabilities of modern modal transition theory are the centrifugal instabilities commonly referred to as Görtler instabilities,

the three-dimensional crossflow instabilities, and the first and second Mack mode instabilities [70]. Depending on the application of a given flowfield, these instabilities can occur alone or in any combination. Fundamentally, instabilities are the form of the forcing factor that causes transition to occur within the boundary layer if the receptivity process is favorable. While the instabilities are the mechanisms to cause transition; there are many additional factors which influence the rate at which transition occurs and the transition onset location. The influencing factors include roughness, freestream noise, curvature, bluntness, wall heating and cooling, suction and blowing, angle of attack, and many more. Section 5 provides a pragmatic look at the factors that influence transition while the current section focuses on the characteristics of the four established instabilities of modern modal transition theory, the secondary instabilities, non-modal instabilities, and entropy layer instabilities.

4.1 Görtler Instability.

Boundary layer which forms over concave geometries has a strong inviscid instability mechanism that establish via the presence of counter-rotating vortex pairs which lead to the transition through typical modalities [29]. The concave wall creates centrifugal forces acting in the wall normal directions that must be balanced by a negative pressure gradient resulting in perturbations in the form of radial displacement [57]. An example of concave geometries in hypersonic research is flared cones. However, the AEDC Tunnel 9 cones were not concave therefore this mechanism to transition was not anticipated. In Figure 14, the concave surface is shown along the z-axis with R as the dimensional radius of curvature and the counter-rotating vortex pairs occur at the wavelength of the disturbances (λ). Görtler instabilities can form on both concave and convex walls. A positive radius of curvature indicates a convex wall and a negative radius of curvature indicates a concave wall [69].

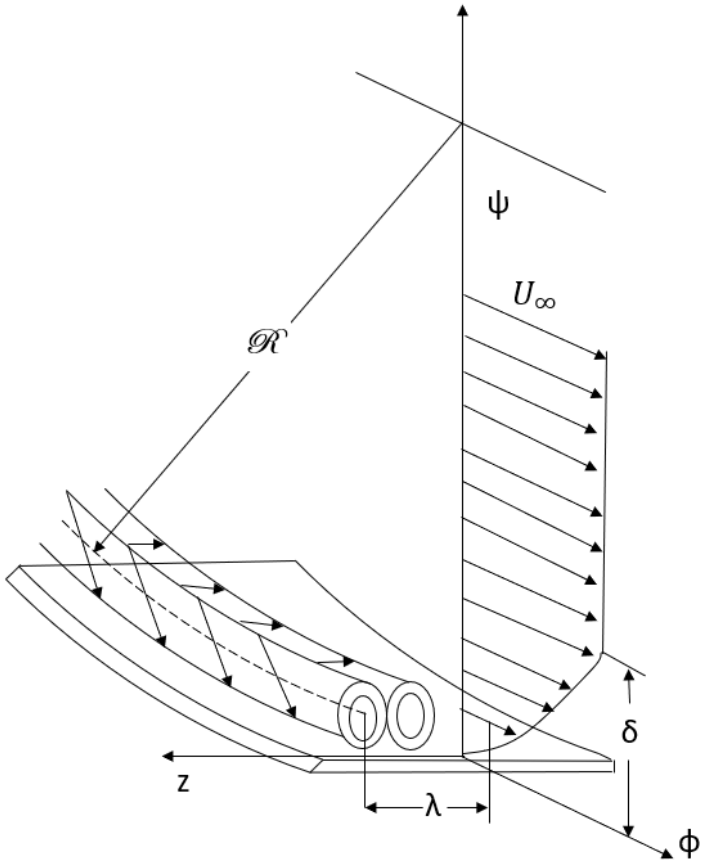

Figure 14. Görtler Instability Schematic Adapted from [29]

The Görtler instabilities are governed by the Görtler number (G) which is a ratio of the centrifugal forces and viscous forces [29]. Görtler instabilities arise when there are more centrifugal forces than viscous forces acting within the boundary layer.

$$G = \frac{U_\infty \theta}{\nu}\sqrt{\frac{\theta}{R}} \tag{2.31}$$

In Equation 2.31, θ is the momentum thickness calculated from Equation 2.4, U_∞ is the freestream velocity, and ν is the kinematic viscosity. Generally, a Görtler instability forms when the radius of curvature is on the same order of magnitude as the boundary layer thickness [29]. In experiments performed by Mendez et al. the effect of the Görtler number on the form of the Görtler instabilities was clearly

demonstrated. When the Görtler number was equal to 4 in Figure 15a, there was no detection of the instabilities forming. As the Görtler number was increased to 9 in Figure 15b a clear wave pattern was present. Figure 15c demonstrates the mushroom-esque structures that formed when the Görtler number was increased to 12. The formation of the mushroom-esque structures was caused by the lower velocity being pushed on top of the high velocity and caused inflection points in the wall-normal velocity profile [57]. Inflection points are the source of instabilities. Finally, as the Görtler number was increased to 18 in Figure 15d, the flowfield was overcome by secondary effects and fully turbulent flow was achieved.

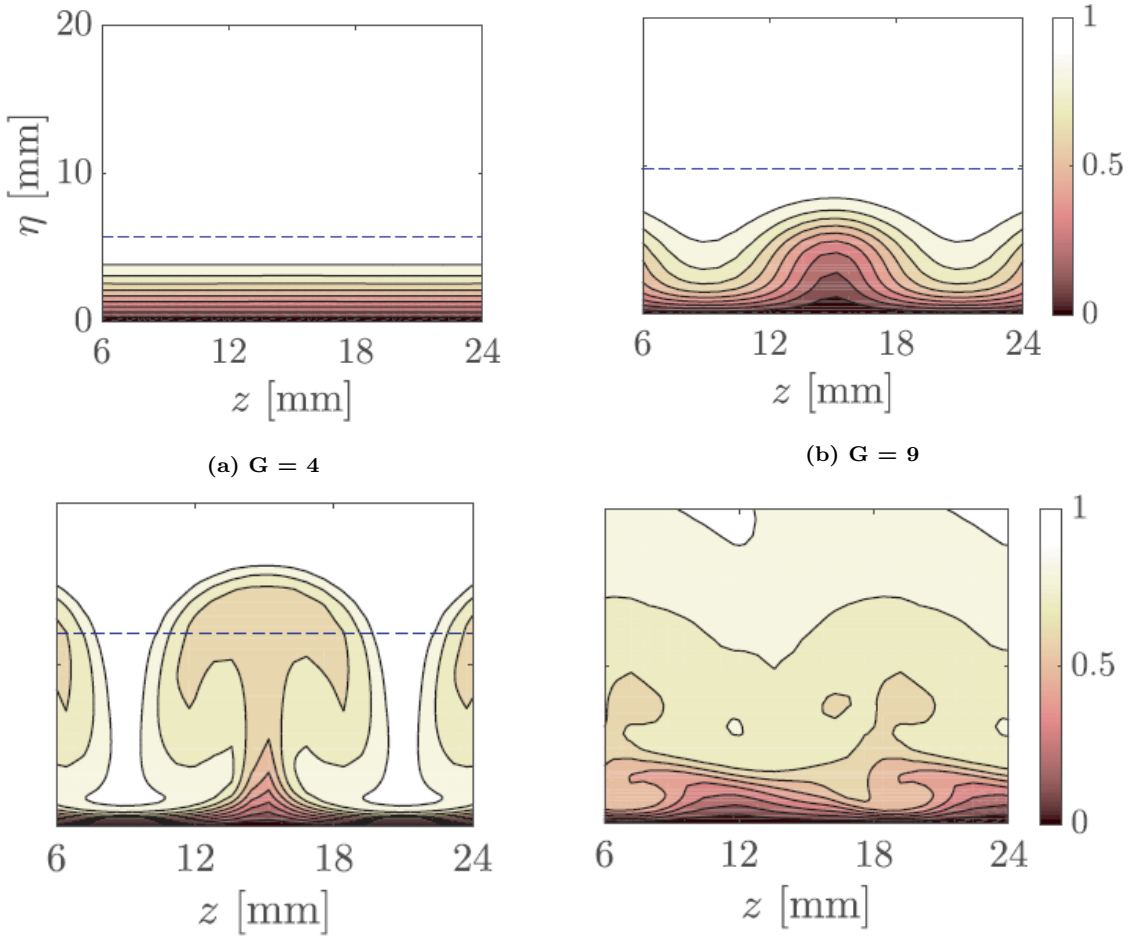

(a) G = 4

(b) G = 9

(c) G = 12

(d) G = 18

Figure 15. Streamwise evolution of U/U_∞ (used with permission) [57]

The streamwise component of the flow is generally small since it is a secondary flow. Additionally there is a balance in the fluid moving away and towards the geometry; therefore, Görtler instabilities have a weak effect on the average base flow [29]. Thus, Görtler instabilities do not break down into turbulence. Instead Görtler instabilities create an unstable flowfield that is susceptible to developing secondary instabilities that lead to transition [57]. The effects of curvature on transition are further discussed in Section 5.3.

4.2 Crossflow Instability.

The crossflow instability forms as a result of pressure gradients on geometries with swept wings or rotating disks. Outside of the boundary layer, the pressure gradient produces curved streamlines at the edge of the boundary layer [68]. As a result of the curved streamlines, the streamwise velocity is reduced but the pressure gradient remains unchanged inside the boundary layer [68]. Thus, the balance between centripetal acceleration and pressure gradient is no longer upheld within the boundary layer. This imbalance results in a secondary flow in the boundary layer, called crossflow, that is perpendicular to the direction of the inviscid streamline [68]. There is a no-slip boundary condition at the wall of the geometry by which all flow, including crossflow, must abide. In order for the crossflow to vanish, an inflection point is created and this inflection point is the source of the crossflow instability [68]. The development of an inflection point in crossflow is shown in Figure 16. The crossflow instability appears as co-rotating vortices and only exist in a three-dimensional boundary layer [68].

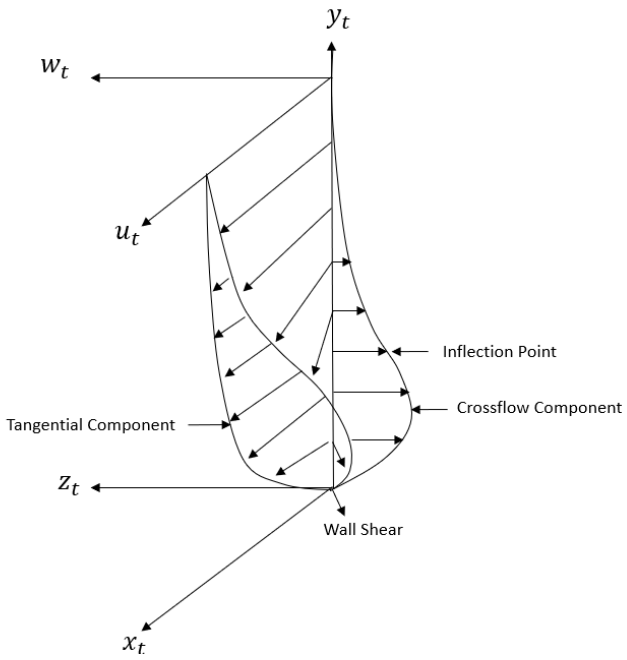

Figure 16. Crossflow Instability Schematic Adapted from [68]

Two types of crossflow instabilities are considered: stationary and traveling. Stationary crossflow instabilities occur through constant forcing functions, like roughness, and are named stationary because they occur at one place on the geometry and follow the streamlines moving through the generalized inflection point in the boundary layer [23]. Traveling crossflow instabilities are excited through freestream fluctuations like noise [20]. Opposite to the behavior of a stationary crossflow instability, traveling crossflow instabilities enter the boundary layer and causes disturbances which travel downstream in the flow. Both traveling and stationary crossflow instabilities can coexist since the two types are excited via different forcing factors. Through linear analysis, traveling crossflow instabilities were predicted to be more unstable even though stationary crossflow instabilities have larger initial amplitudes [20]. Although, under realistic flight conditions, the forcing factors that influence traveling crossflow instabilities, like freestream noise, are very low and thus stationary crossflow instabilities are more likely to cause transition.

An example of a geometry with a flowfield dominated by crossflow instabilities is the Hypersonic International Flight Research Experimentation Program Flight 5 Vehicle (HIFiRE-5). The HIFiRE-5 is a 2:1 elliptic cone whose transition was dominated by roughness induced stationary crossflow instabilities [20]. The elliptical leading edge of the HIFiRE-5 fostered the development and growth of crossflow instabilities which led to turbulent flow. The geometry of the AEDC Tunnel 9 test articles were axisymmetric and do not have an elliptical leading edge. Therefore, it was unlikely that the cause of increase heat transfer data in Figure 3 for the 12.7, 25.4, and 50.8 mm cases was due to crossflow instabilities.

4.3 First and Second Mack Modes.

The Rayleigh equation is a simplification of the Orr-Sommerfeld Equation discussed in Section 3.1. The Orr-Sommerfeld equation applies to incompressible flow. If the friction terms are neglected from the Orr-Sommerfeld Equation, then the Rayleigh Equation has been derived. Neglecting the friction terms is a valid assumption for high Reynolds number flows because the friction terms are multiplied by a factor $\frac{1}{Re}$ that the inertial terms are not multiplied by according to Equation 2.14. Therefore the friction terms become negligible. Neglecting the friction terms simplifies the fourth order Orr-Sommerfeld Equation to a second order ordinary differential equation (ODE).

$$(U - c)(\varphi'' - \alpha^2\varphi) - U''\varphi = 0 \tag{2.32}$$

In Equation 2.32, the U is the mean velocity vector, c represents the phase velocity of the wave, and φ is complex amplitude of the stream function. A solution set to the compressible Rayleigh Equation attributed to Mack and resulted in the First and Second Mack Mode instabilities [49].

The first mode instability is similar to low speed Tollmien-Schlichting waves and

is amplified when the wave fronts are oblique to the stream direction and diminished by wall cooling [50]. The second mode instability acts like a trapped acoustic wave between the wall and the sonic line as shown in Figure 17. The second mode instability is most amplified when the wavefronts are normal to the stream direction. It grows rapidly on cold walls and occurs at high Mach numbers [76]. A comparison between the behavior of first and second mode instabilities is provided in Figure 17. Transition prediction methodology such as Linear Stability Theory (LST) and the Parabolized Stability Equations (PSE) enable reliable analytic prediction of the first and second mode instabilities. The methods for transition prediction are discussed in Section 6.

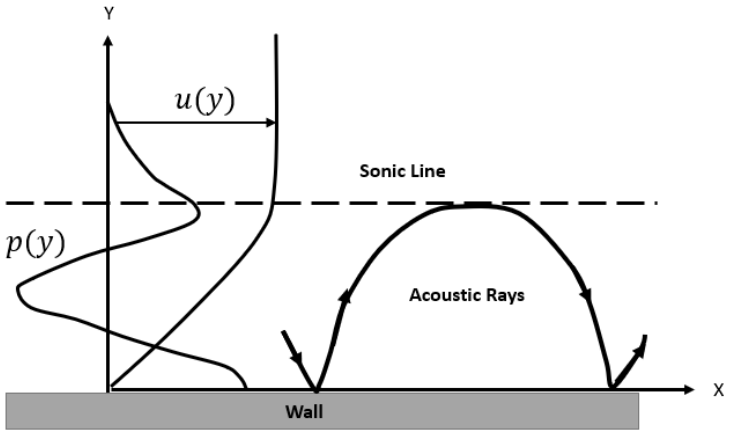

Figure 17. First and Second Mack Mode Instability Schematic Adapted from [59]

Casper et al. performed boundary layer transition experiments on a sharp 7° half-angle cone at the Sandia Hypersonic Wind Tunnel at Mach 5, 8, and 14. In the Mach 5 experiments, both first mode and second mode instabilities were detected. The Mach 8 and higher experiments revealed that transition was completely dominated by second mode disturbances [11]. Thus, experiments at higher Mach numbers are not expected to experience first mode instabilities. Second mode instabilities are the most likely modal cause of transition for axi-symmetric cones with low bluntness. The AEDC Tunnel 9 experiments experienced second mode dominated transition on

the cones with the nose radii of 0.152, 5.08, and 9.53 mm.

Second mode instabilities are identified by plotting the spectra of pressure fluctuations over the frequency as shown in Figure 18. Figure 18 was produced by Estorf [24] and reproduced by Schneider [76]. Estorf's experiments focused on measurements from a 7° sharp cone in the Purdue University's Boeing Air Force Office of Scientific Research (AFOSR) Mach 6 Quiet Tunnel (BAM6QT) and compared to the Mach 6 results from a conventional noise level Ludweig style wind tunnel at Technische Universität Braunschweig. More details on the effects of freestream noise on transition is provided in Section 5.2. However, the important message taken from Figure 18 as it pertains to the current section is that the clear peak in the pressure fluctuations occurred around 220 kHz for both the noisy and quiet conditions [76]. Therefore, the transition on Estrof's 7° sharp cone was second mode dominated from an instability with the frequency of 220 kHz.

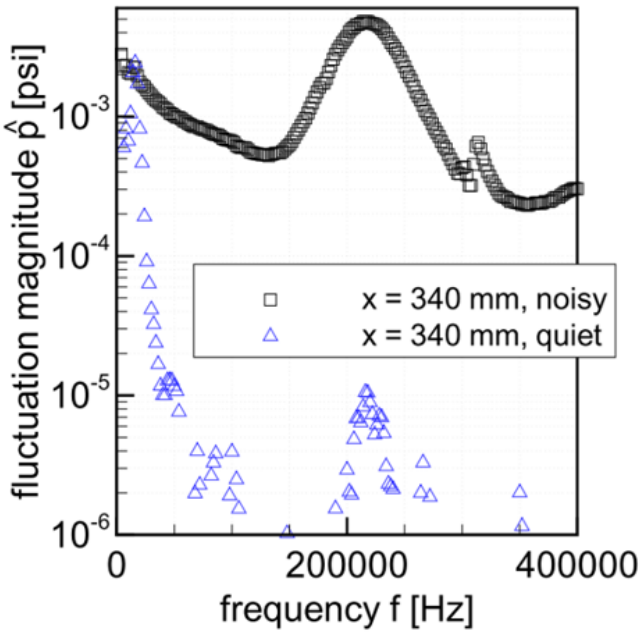

Figure 18. Pressure Fluctuation Spectra in Noisy vs Quiet Flow (used with permission) [76]

For the 7° half-angle cones with the nose radii of 12.7 mm, 25.4 mm, and 50.8 mm provided by AEDC Tunnel 9, second mode domination was the most likely instability if the instability was modal. However, as the nose radii increased to the three most blunt cases, no indication of second mode instability dominance appeared in the spectral content [59]. Therefore, the instability seen the AEDC Tunnel 9 experimental data for the 12.7, 25.4, and 50.8 mm nose radii cases was predicted to be non-modal.

4.4 Supersonic Mode.

The supersonic mode was discovered by Mack but had not received as extensive research rigor as the first and second Mack modes because the supersonic mode had a significantly smaller peak growth rate than the second mode for axi-symmetric cone applications [40]. However, recent research on a 5° half-angle blunt cone with hot wall conditions ($T_w/T_\infty > 1$) performed by Knisely and Zhong confirmed the existence of the supersonic mode instabilities as well as proved that under certain conditions the supersonic mode instabilities had a higher growth rate than the second mode instabilities [39]. Additionally, the supersonic mode had been shown to exist on an axi-symmetric cone with a cold isothermal wall [38].

The supersonic mode, also known as the spontaneous radiation of sound, occurs when an unstable second mode instability synchronizes with the slow acoustic spectrum causing the disturbance to travel upstream supersonically relative to the mean flow outside of the boundary layer [40]. A schematic of the supersonic mode is presented in Figure 19 where the regions of the flow were described in terms of the relative Mach number (M_r). The relative Mach number is defined as a comparison between the speed of the instability relative to the speed of the mean flow and was calculated by

$$M_r(y) = \frac{\bar{u}(y) - c_r}{\bar{a}(y)} \tag{2.33}$$

where $\bar{u}(y)$ is the local mean flow velocity tangential to the wall, $\bar{a}(y)$ is the local mean speed of sound, and c_r is the disturbance propagation speed. Figure 19 defined a near wall region were the relative Mach number was less than one. In this region the mean velocity was significantly slowed due to the no-slip boundary condition enforced at the wall and therefore the disturbance propagation was larger in comparison [40]. More information on the no-slip boundary condition enforced at the wall is available in Section 2.2. The sonic line at a relative Mach number of -1 acted as the barrier between the supersonic and subsonic region in which second mode instabilities experienced acoustic modulation [39]. Recall from Section 4.3 that second mode instabilities act like a trapped acoustic wave. Thus, in the supersonic region near the wall, the unstable second mode instabilities form. Figure 19 shows that the subsonic region existed between the relative Mach number of -1 and 1. In this region, the disturbance was traveling at a subsonic relative Mach number with respect to the local mean flow velocity tangential to the wall. Additionally, this region is where the "rope-like" wave pattern is observed. A second supersonic region formed when the relative Mach number was greater than one. In this region the disturbance was traveling upstream at a supersonic relative Mach number with respect to the freestream velocity which resulted in decaying Mach waves outside of the boundary layer [39]. The Mach wave angle (μ) is defined as $\arcsin(1/M_r)$ [39].

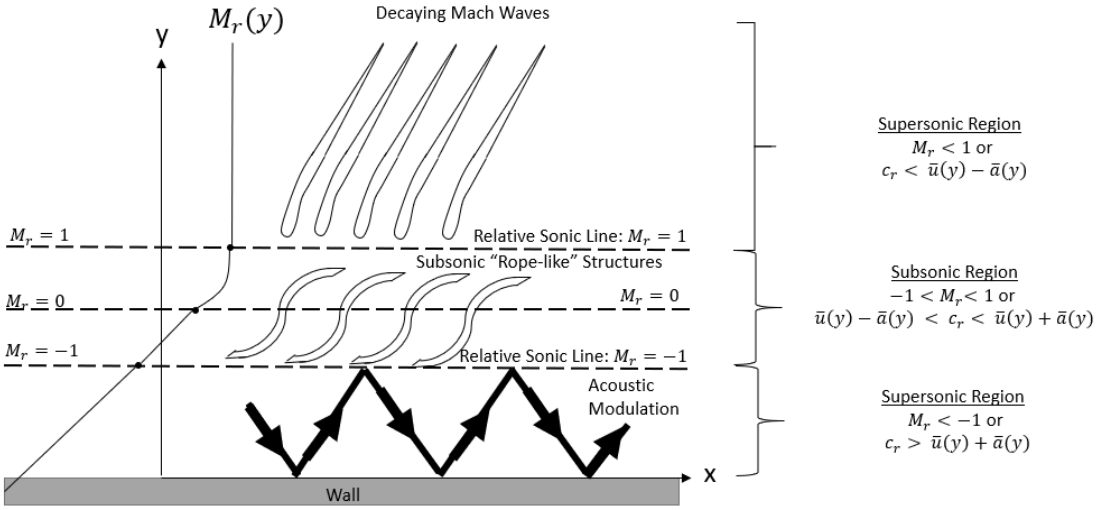

Figure 19. Supersonic Mode Schematic Adapted from [39]

4.5 Secondary Instabilities.

The linear growth regime of a disturbance is a period of exponential growth for an instability [20]. The term linear does not mean that the slope of the disturbance amplitude is growing linearly; it refers to the linearity of the disturbance itself. In the linear growth regime any non-linear interactions with other instabilities in the flow field are negligible. Linear growth of an instability can lead to secondary instabilities. The primary instability produces the large scale eddies. When the primary instability begins to breakdown into smaller scales or interacts with other large scale eddies, secondary instabilities form [60]. Secondary instabilities are a nonlinear phenomena which can lead to transition within the boundary layer.

Secondary instabilities are traditionally broken down into three categories. The first category of secondary instabilities is the Type I or the z-mode instabilities are defined as a high frequency mode which result from the the minimum in the spanwise gradient of the streamwise velocity component [52]. The Type II or the y-mode secondary instabilities are defined as a high frequency mode which result from the

local maximum of the wall normal gradient of the streamwise velocity component [52]. The final category of secondary instabilities is the Type III which are defined as low frequency modes which result from the spanwise gradient of the streamwise velocity component like the Type I secondary instabilities [52].

4.6 Non-Modal Instabilities.

For the blunt nose cones experiments performed by Stetson [79], Jewell et al. [35] and Moraru [59], first and second Mack mode instabilities did not describe the transition phenomenon observed on the blunt nose cones as it had for sharp nose cones. By precluding modal growth analysis, Figure 12 dictates that the transient growth mechanism of non-modal instabilities must be investigated as the cause to the onset of transition for blunt cones.

Paredes et al. used a reduced harmonic form of the linearized Navier-Stokes equations (RHLNSE) to study the modal and non-modal instability characteristics of the blunt nose cones described in Figure 20 from the experiments of Jewell et al. [62]. Jewell et al. tested a 7° half-angle cone in the Air Force Research Lab (AFRL) Mach 6 conventional wind tunnel and measured the transition onset location (ξ_T), the Mack mode N factors at the transition onset location (N_{MM}), and the corresponding frequency (F_{MM}) at the transition onset location.

Case	R_N [mm]	Re_∞ [x $10^6 m^{-1}$]	Re_{R_N} [x 10^3]	ξ_T [m]	$N_{MM}(\xi_T)$	$F_{MM}(\xi_T)$ [kHz]
I	0.508	91.5	46.48	0.103	7.77	1760
II	1.524	30.5	46.48	0.223	3.75	660
III	1.524	61.0	92.96	0.170	1.14	1000
IV	1.524	91.5	139.4	0.133	0.04	1340
V	2.540	91.5	232.4	0.147	-	-
VI	5.080	91.5	464.8	0.161	-	-
VII	15.24	30.5	464.8	-	-	-
VIII	15.24	61.0	929.6	0.227	-	-
IX	15.24	91.5	1394	0.051	-	-

Figure 20. Air Force Research Lab Blunt Nose Cone Configurations and Transition Parameters at M = 5.9 Adapted from [35]

Further explanation on how the N factors and corresponding frequency are related are provided in Section 6.2. Briefly, the N factor is an indication of how much an instability has grown or decayed given its current amplitude ($A(f, s)$) in comparison to its initial amplitude ($A_0(f)$).

$$e^N = \frac{A(f, s)}{A_0(f)} \tag{2.34}$$

To anchor the current discussion, consider the clearly modal transition case, Case I from Figure 20, because it has a nose radius and freestream Reynolds number which indicated a second mode instability dominated transition. For this case, the maximum N factor at the transition location was measured at 7.7 with a frequency of 1760 kHz. As the nose radius was increased, the N factor at the transition location decreased which indicated that the second mode instabilities were less amplified at the transition location [62]. Once the N factor decreased below a value of approximately 2, then the cause of transition was determined to have been non-modal [62].

For transient growth analysis, or non-modal instabilities growth, over blunt cones there are two regions of interest: the nose region and the frustum region [62]. The

research effort of Paredes et al. considered both statonary disturbances and traveling disturbances along the frustum [62]. Considering Cases II - IV from Figure 20, Figure 21 provides the contours of the N factor based on the total energy gain (N_E) as a function of frequency (F) and azimuthal wavenumber (m). From Figures 21a - 21d, it was concluded that if the nose Reynolds number (Re_{RN}) was increased via increasing the freestream Reynolds number of the nose radius, then the non-modal growth persisted to higher disturbance frequencies [62]. However, once the nose radius was increased to 5.08 mm for Case VI, the N factor associated with the total energy decreased. The Paredes et al. computational results confirmed the observations in the Jewell et al. experiments discussed in Reference [35]. In Figures 21a and 21b second mode instabilities were detected and the regions of modal growth are blacked out [62]. As further evidence that non-modal instabilities are the cause of transition for blunt cones, in Figure 21c, the planar waves yielded a new peak in N factors which was distinctly different from the second mode instabilities [62].

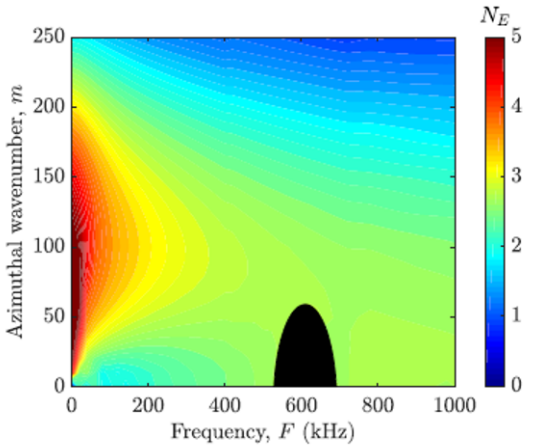

(a) Case II [62]

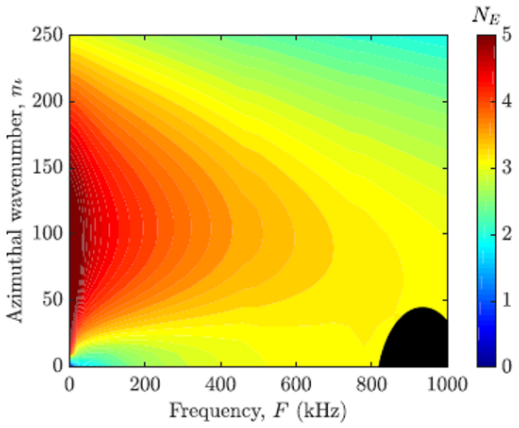

(b) Case III [62]

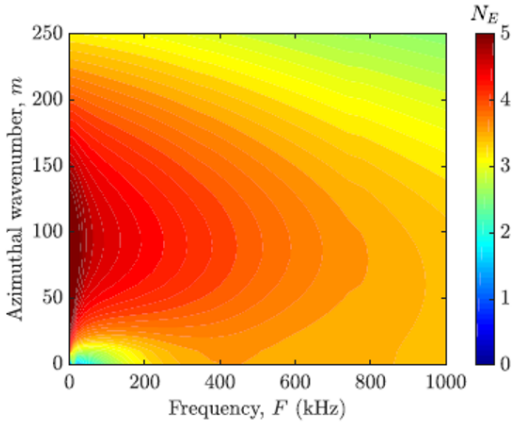

(c) Case IV [62]

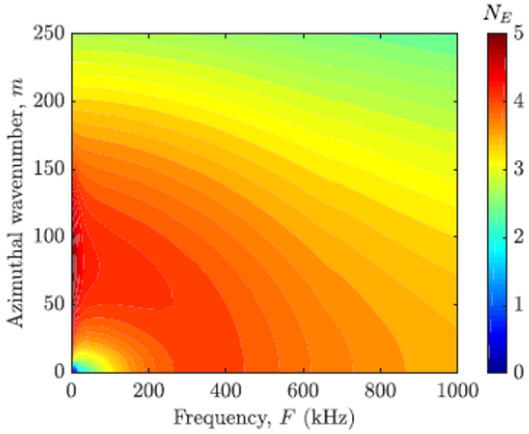

(d) Case V [62]

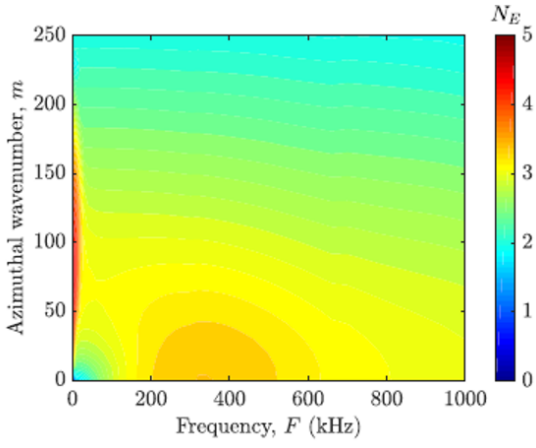

(e) Case VI [62]

Figure 21. Contours of N_E computed with RHLNSE [62]

Paredes et al. conducted computational research into the moderate bluntness region where non-modal growth could occur as a separate precursor to the modal growth experienced [62]. In essence, there are three regions of bluntness which follow a different path to transition. In the first, and most extensively understood region, the sharp nose cone would be dominated by second mode transition. As the nose radius increased to the second region of moderate bluntness the transition onset location would be delayed but would still be second mode dominated with a notable difference to the flowfield. Ahead of the second mode instabilities on the rear of the frustum, additional non-modal instabilities would form near the nose region. Once the second mode instabilities dominated the transition to turbulence, the non-modal instabilities would be of little consequence. When the third region of large bluntness was reached by increasing the nose radius, the second mode instabilities would no longer occur within the length of the cone and the non-modal transient growth would be the only instability leading to transition onset. The impact of the definition of the second region of moderate bluntness was an explanation for how a cone of increasing nose radius went from experiencing a second mode dominated transition to a non-modal transition. Although why the break with modal transition theory occurred is still an active area of research.

In support of the moderate bluntness region, the axial growth disturbance amplitude in terms of the N factors based on total energy (N_E) and kinetic energy (N_K) are shown in Figure 22 for Case II from Figure 20. In Figure 22 two peaks occurred for disturbance amplification. The first peak was attributed to the non-modal instability and the second peak was attributed to the second mode instability which occurred further down the cone [62]. The results of Figure 22 were consistent with the experimental results of Marineau et al. [55]. Therefore, in Case II it can be concluded that non-modal instabilities occurred prior to the onset of turbulence due to delayed

second mode instabilities as a results of bluntness.

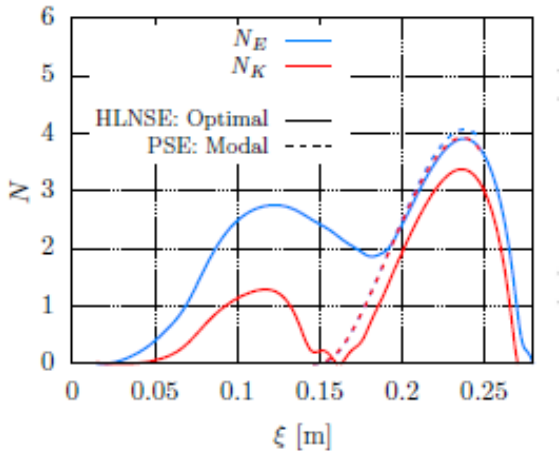

Figure 22. Evolution of the N-factor Based on the Total Energy and the Kinetic Energy [62]

4.7 Entropy Layer Instabilities.

An instability forms anytime an inflection point in the angular momentum of the flowfield [31]. If that condition is met, an instabilities will form in either the boundary layer or the entropy layer. Recall from Section 1.2 that the boundary layer eventually grows to "swallow" the entropy layer and that the entropy layer is a region of inherent vorticity. It is not well understood what happens to pre-existing instabilities in the entropy layer after the swallowing length or how the pre-existing entropy layer instabilities effect boundary layer transition.

Experiments performed by Stetson et al. measured instabilities over a blunt cone using hot wire anemometry [82]. The results revealed that the entropy layer disturbances grew slowly outside of the boundary layer, initially diminished as they entered the boundary layer, and then grew rapidly inside the boundary layer leading to transition [82]. This sequence of events following entropy layer instabilities was substantiated and further investigated by Greenwood and Schneider in Mach 6 flow

over a cone-ogive-cylinder geometry [31].

The power spectra shown in Figure 23 revealed that the instabilities measured by Greenwood and Schneider behaved differently than boundary layer instabilities [31]. Boundary layer instabilities are greatly affected by an increase in Reynolds number. However, Figure 23 demonstrated that as the Reynolds number increased, the peak frequencies corresponding to the entropy instabilities remained constant [31]. Another entropy layer instability trait which differentiated these experimentally measured instabilities from boundary layer instabilities was that the peak frequency remained constant in the streamwise direction [31]. The constant frequency values of the 30° cone-ogive-cylinder geometry are 26 and 35 kHz [31]. Greenwood and Schneider verified that the results were not due to vibrations or electrical noise [31]. Since the measured instabilities behaved differently than boundary layer instabilities it was concluded that the instabilities measured were uniquely entropy layer instabilities and these instabilities were the cause of transition [31].

The evolution of an entropy layer instability as described by Stetson et al. is depicted in Figure 23 with the data produced from the research efforts of Greenwood and Schneider. Between the streamwise positions of x = 0.58 m and x = 0.61 the entropy layer instability experienced modest growth in power spectra. Then, the entropy layer instability experiences brief decay in power spectra in the streamwise positions of x = 0.71 m and x = 0.81 m as the entropy layer was swallowed into the boundary layer [31]. Finally, at x = 0.91 m the entropy layer instability experienced a period of rapid growth to transition.

The interaction between the entropy layer and boundary layer represents another hypothesized explanation for the break with the second mode dominated transition phenomenon seen in Figure 3 experienced on cones with increasing nose radii. Although this research effort seeks to isolate the modeling of distributed surface rough-

ness to determine if it was the cause of the break with the second mode dominated transition phenomenon, important information from the other leading hypotheses was gleaned for the interpretation of the final results.

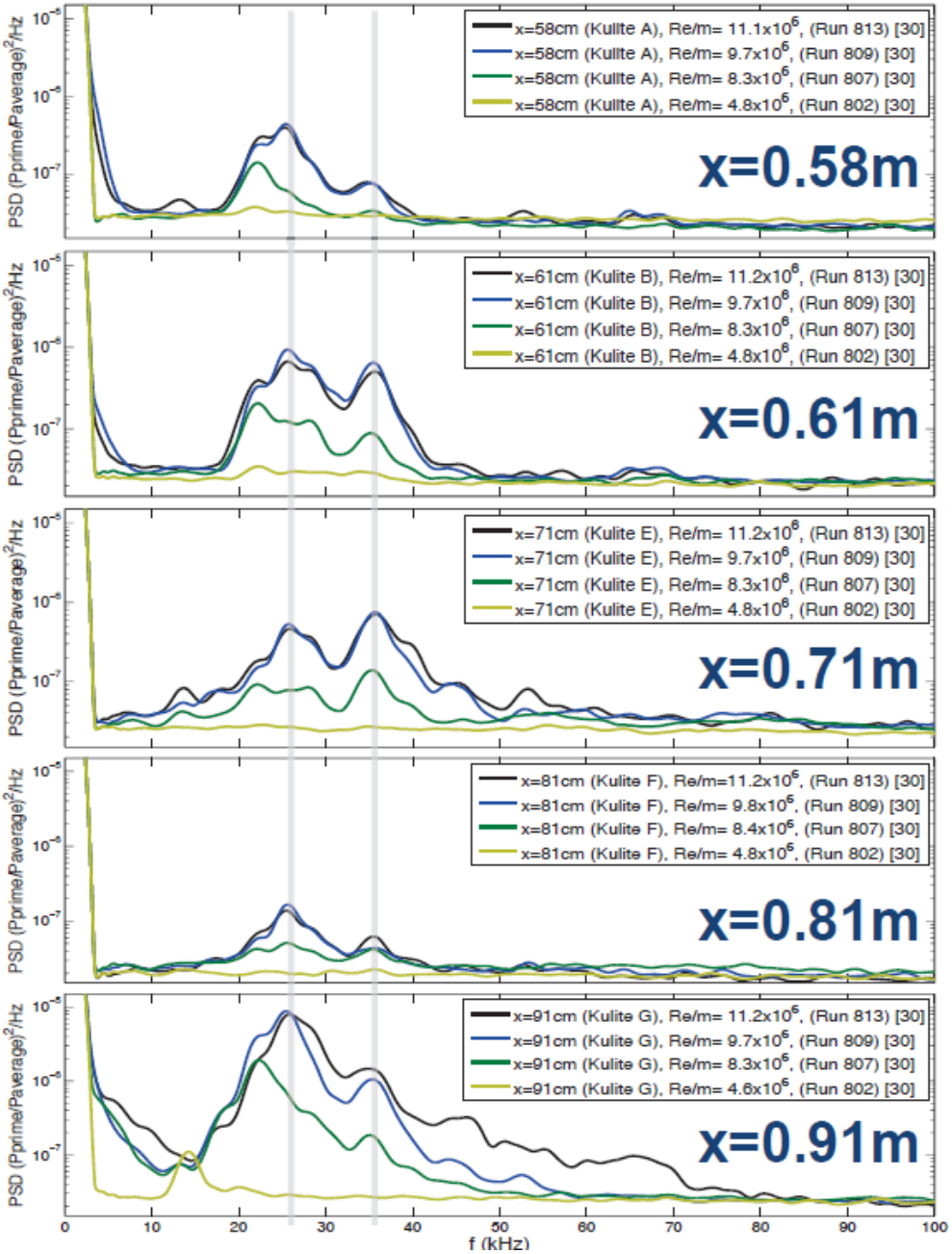

Figure 23. Power Spectra on 30° Cone-Ogive-Cylinder (used with permission) [31]

5 Factors that Influence Transition to Turbulence

As stated previously, instabilities are the mechanisms that cause transition in the boundary layer and the mechanisms that cause transition are an area of ongoing research. The study of the factors that influence transition occurs in parallel. The inability to predict transition is primarily a result of an incomplete understanding of the physical aspects of the phenomenon leading to transition and the inability to model all of them completely [79]. In Section 3, the Reynolds number was introduced as one factor that influences transition. However, transition can be influenced by countless factors including roughness, freestream noise, curvature, bluntness, angle of attack, suction, blowing, wall heating or cooling, and many more. Studies isolating each factor at a time are discussed below so that the aggregate knowledge can be applied to future work. However, to fully comprehend boundary layer transition the factors which influence transition to turbulence must also be studied in combination with each other since these factors which affect transition are not independent of each other and are not additive in effect [8].

5.1 Roughness.

AEDC Tunnel 9 postulated that the increased heat transfer rates seen in Figure 3 for nose radii 12.7, 25.4, and 50.8 mm were hypothesized to be due to distributed surface roughness of the test articles. Distributed surface roughness would incur a forcing function which would take the form of a non-modal instability. If the distributed surface roughness alone was a strong enough forcing function to cause transition to occur then the instabilities would face a period of transient growth before the onset of turbulence. Section 5.1.1 provides insight into the types of roughness and Section 5.1.2 discusses distributed surface roughness methodology created by Dinzl for research on the HIFiRE-5 [20].

5.1.1 Types of Roughness.

Roughness is considered in two forms: isolated and distributed. Isolated roughness, or discrete roughness elements (DREs), are singular, uniform elements placed on the geometry and the spacing of the elements corresponds to the excitement of a particular wavenumber. Figure 24 shows a depiction of how flow encounters an isolated roughness element. In front of the DRE, a small separation region forms and the flow splits around the isolated roughness element generating a wake with streamwise vorticity. DREs can affect transition via three modes: the wake with the streamwise vorticity has an unstable shear layer where an instability can form, the streamwise vorticity behind the DRE grows via the instability mechanisms discussed in Section 4, and roughness can interact with freestream disturbances [74]. A DRE functions by forcing a specific wavenumber to dominate the disturbance field even if it is not the most unstable wavenumber. In natural transition studies, usually many parameters play a role in which the aggregate leads to transition. However in DRE research, the forced transition determined by the design of the DRE obviates all other processes present in the experiment [21].

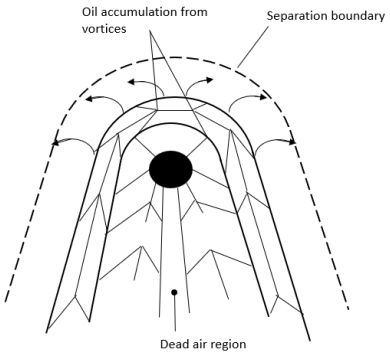

Figure 24. Flow Behavior Around Discrete Roughness Element Adapted from [88]

In DRE analysis, the height of the roughness element becomes a particular point of interest. The critical height of the roughness element is the height at which a single

roughness element begins to have an effect [75]. As the roughness height increased the transition location moved forward until the effective roughness height was reached. When the effective roughness height was reached the transition location no longer moves forward no matter the increase in height [75]. To determine the height of the roughness element causing transition, a power spectral density calculation can be performed. A power spectral density calculation is a Fourier analysis that takes the physical signal given by the instability and decomposes it into the continuum of frequencies for all time. For transition dominated by isolated roughness elements there will be a peak in the power spectral density indicating a specific frequency band in which the wave modeled instability occurred.

Distributed roughness consists of small random variations of the surface over an area of the body. A pertinent example of distributed roughness is the machine finish on the surface of the test article material. The distributed roughness varies on the order of microns over the smoothed surface. Since practically all common aerospace vehicles are made of materials that have a machine finish, this area of research is widely applicable. Another classic hypersonic example of distributed roughness is ablation. Ablation is the loss of surface material due to high temperatures during flight or tunnel experimentation. The ablation patterns created are material dependent and cause a changing surface topology of roughness throughout the flight. Ablation may cause instabilities to suddenly appear mid-flight due to the development of a new surface roughness topology.

On a distributed roughness surface, many individual disturbances occur simultaneously with different amplitudes and wavelengths and interact non-linearly. Therefore if the boundary layer transition was driven by nonlinear effects, then the linear stability analysis discussed in Section 6 will fail to predict transition for distributed roughness problems because it neglects all nonlinear effects.

5.1.2 Simulation of Distributed Roughness.

DREs cannot be used to simulate the variation of a distributed roughness pattern by simply placing them closer together and varying their heights because DREs create a disturbance that is unrealistically clean and the roughness elements cannot move or adjust the roughness height to mirror natural occurrences such as ablation. Specifically, a local DRE provides a specific disturbance at a specific frequency and distributed roughness provides a broadband disturbance in a range of frequencies. Therefore, instead of using numerous small, random DREs to simulate a roughness pattern, Dinzl developed an algorithm to simulate distributed roughness on the entire surface of a computational model. The basic principle of this technique is each surface node was shifted some distance from zero to the maximum roughness height in a uniform distribution [20]. The nodes in the boundary layer above the initially shifted nodes were also shifted with a hyperbolic tangent descent. Well before the boundary layer height, there was no detection of the perturbed grid below. Since every node was perturbed along the surface nonlinear interactions can be accurately simulated. The distributed grid roughness does not produce the same initial disturbance as a DRE with the same height due to the simulation of the nonlinear interactions [21]. The fundamentals of Dinzl's methodology were based on the contributions of Gronvall et al. who created a distributed roughness patch which resulted in computational data that quantitatively resembled smooth-body transition. [32].

Dinzl conducted a DNS research effort on the HIFiRE-5 geometry, a 2:1 elliptic shaped cone, to research the effects of distributed roughness and the resulting stationary crossflow instabilities. The distributed roughness heights varied from 0.5, 2, and 4 μm with three levels of DNS quality grid refinement at 63×10^6, 106×10^6, and 164×10^6 total cells for a quarter of the elliptical cone geometry [20]. Dinzl concluded that as the roughness height increased the heating pattern moved further down the

geometry. However, if the roughness pattern was the same and the only difference was adjusting the roughness height by a factor, the position of the stationary crossflow instability will not change [20].

Application of the distributed roughness algorithm developed by Dinzl required a smooth body grid. The algorithm read in the smooth body grid and shifted the nodes closest to the surface and the respective nodes above to produce the grid file with distributed roughness. When running the DNS simulation with an appropriate flow solver, the new roughness grid is utilized. Dinzl showed that the distributed roughness pattern has to be interpolated onto each level of grid refinement for quantitatively comparable data. In Figure 25a, random roughness patterns were applied to each level of grid refinement, and the resulting data was qualitatively similar but not quantitatively useful. However in Figure 25b, the roughness pattern generated was interpolated onto each level of refinement and the data became comparable quantitatively. In Figure 26, a physical look was provided for how the same roughness pattern was created on the same surface at different levels of refinement. The interpolation of the roughness pattern was a necessary requirement for proving grid independence with the roughness grids.

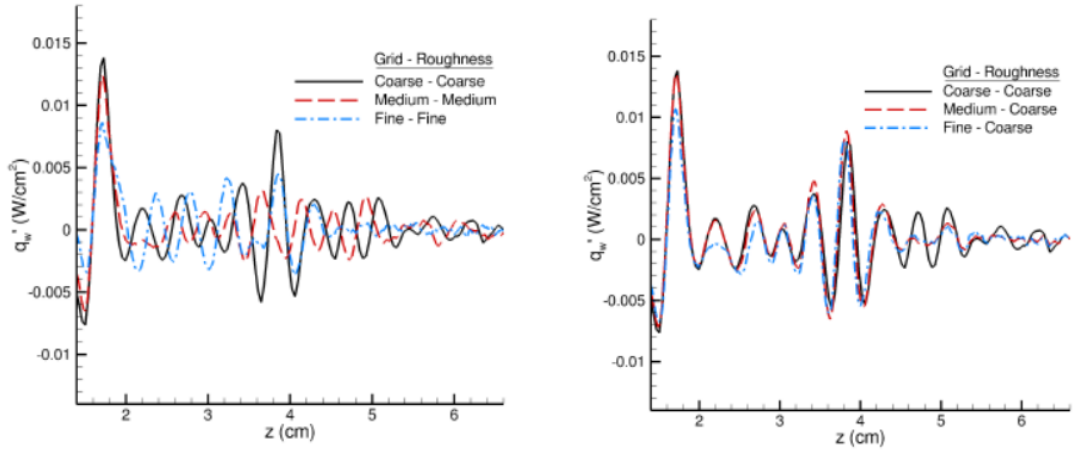

(a) Randomly Generated Roughness Pattern **(b) Interpolated Roughness Pattern**

Figure 25. HIFiRE-5 Heat Flux Data (used with permission) [21]

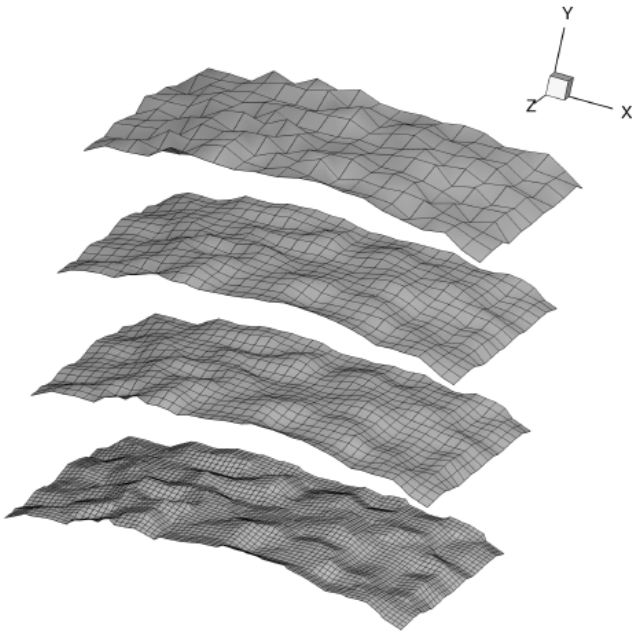

Figure 26. Interpolated Grids at Increasing Levels of Refinement (used with permission) [21]

It is important to note that Dinzl's method is grid density dependent. The computational mesh forces a distrubance at the highest wavenumber possible and is directly proportional to the grid cell density, therefore finer grids will provide larger forcing functions for the same distributed roughness pattern [21]. Similarly, if the grid is too coarse and the cell distance is longer than the wavelength of the instability traveling in the streamwise direction then the grid will fail to detect the instability. The mitigation steps taken in this research effort are described in Chapter 3 Section 2.1.

5.2 Freestream Noise Levels.

Hypersonic flight noise level data at sufficiently high frequencies is not prolific due to the expensive nature of hypersonic testing. From the flight data presented by Fisher and Dougherty, it was evident that hypersonic flight conditions were characterized by lower noise environments or low freestream fluctuations than conventional wind

tunnels [28]. Fisher and Dougherty experimented on a 5° half-angle cone which was mounted in front of an F-15 aircraft with a pitot tube and their experiments resulted in the conclusion that as the Mach number increased from Mach 0.5 to a maximum of Mach 2, the noise levels decreased [28], [27]. The reason for the decreased noise levels was a function of the smaller-scale turbulence at higher altitudes [71].

Conventional wind tunnels have noise levels as high as 5% while hypersonic flight noise conditions are one to two orders of magnitude smaller [12]. The noise percentage is calculated by the pressure fluctuations divided by the average pressure reading.

$$\text{Noise} = \frac{\text{rms}}{\text{Pitot}_{\text{avg}}} \cdot 100 \tag{2.35}$$

The noise is difficult to remove from conventional wind tunnel facilities because the acoustic disturbances radiate from the turbulent boundary layer present on the test section walls and throat [71]. Under the influence of such noisy conditions instabilities can be amplified that either would not be amplified at all or be amplified much sooner than if the noise conditions had been realistic to hypersonic flight conditions. The augmented amplification of instabilities leads to early transition locations. If hypersonic programs were to make developmental design decisions based on the transition locations measured in a conventional wind tunnel then the thermal protection system requirements would be higher, leading to more vehicle weight, lending itself to higher requirements that in the end could be completely unnecessary and very expensive.

The most cost effective and accurate solution to hypersonic transition research is conducting tests in quiet tunnels. Two notable quiet tunnels in existence today are the NASA Langley Research Center Quiet Tunnel and the Boeing AFOSR Mach 6 Quiet Tunnel. Beckwith of NASA Langley Research Center led the successful development of the first quiet tunnels [73]. Beckwith's work began in the late 1960s and yielded the first successful quiet tunnel which operated at Mach 3.5. Later a

Mach 6 quiet nozzle was built. Beckwith's trials and errors led to two fundamental discoveries which paved the way for the development of additional quiet tunnels. The first was the necessity of nozzle bleed slots upstream of the throat to remove Görtler instabilities in the concave region of the contraction which persisted into the convex region and jeopardized the existence of laminar flow for the test section [73]. Beckwith also found that in order to maintain a laminar boundary layer on the nozzle it was required that the throat be highly polished [73]. In order to meet the requirements of this fundamental second discovery of Beckwith, an air filter was required to filter out particles that would damage the highly polished nozzle [73]. For more details the NASA Langley quiet tunnel please see reference [73].

The Boeing AFOSR Mach 6 Quiet Tunnel (BAM6QT) at Purdue University has been the leading quiet tunnel for hypersonic boundary layer transition research. The BAM6QT made use of both Beckwith's most notable discoveries. The BAM6QT is a Ludwieg tube style wind tunnel and was made quiet by removing the turbulent boundary layer through bleed slots at the throat [11]. Once the turbulent boundary layer has left, a new laminar boundary layer can form without the freestream acoustic noise disturbances. By closing the bleed slot the BAM6QT is able to run as a conventional wind tunnel. For more details on the development or dual capabilities of the BAM6QT please see reference [73]. Additionally, the future of hypersonic boundary layer testing will include the University of Notre Dame's recently revealed Mach 6 hypersonic wind tunnel which will have the advantage of being the largest quiet tunnel in the United States.

Casper et al. conducted a direct comparison of conventional and quiet hypersonic wind tunnels [11]. The experimental model was a 7° half-angle cone placed at zero degrees angle of attack with unit Reynolds numbers between 3.3 and 15.4 x 10^6. Testing was conducted in the BAM6QT since it can facilitate testing as both a quiet wind

tunnel and as a conventional noisy tunnel. In Figure 27, the pressure power spectral density chart of the Casper et al. experiments is provided. From Figure 27 it was concluded that for both the noisy and the quiet flow conditions the flow was second mode dominated. For the quiet flow, cases the second mode waves centered around 220 kHz and for the noisy flow cases, the second mode waves centered around 330 kHz. Considering only the noisy flow data of Figure 27 shows that as the Reynolds number increased, the second mode instability peaked at a higher frequency. The increase in peak frequency for the second mode instability was because as the Reynolds number increased, the boundary layer became thinner. Thus the second mode instability transitioned at a higher frequency.

In all the noisy flow cases, transition occurred. Under quiet flow conditions, the transition location was significantly delayed and demonstrated completely laminar flow over the entire cone when placed under Mach 6 quiet flow, even at the locations that transition was detected under noisy flow conditions [11]. For the quiet flow conditions, the second mode instabilities were detected on the last sensor where the second mode instabilities for the noisy flow conditions were detected on the first sensor [11]. The Casper et al. experiments proved that noisy freestream conditions provoked earlier instability amplification and flow transition within the boundary layer.

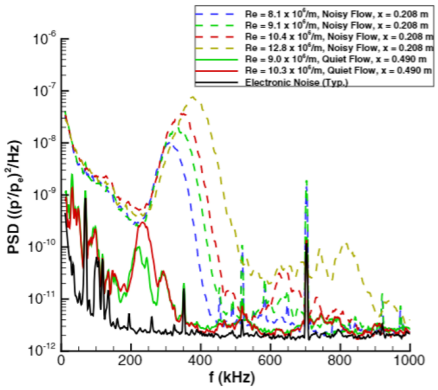

Figure 27. PSD of Second Mode Waves Under Noisy and Quiet Flow Conditions in the BAM6QT [11]

Low plotted the ratio of the transition Reynolds number with and without freestream turbulence against the freestream turbulence level provided in Figure 28 [46]. The freestream turbulence level was defined as the fluctuation component over the mean component of the velocity. The line of best fit provides a linear correlation for the data in Figure 28. Thus, it was concluded that as the freestream turbulence increased the transition Reynolds number will monotonically decreased. The AEDC Tunnel 9 is a conventional wind tunnel therefore freestream noise could be an influencing factor in the experimental transition data. The percent noise for the AEDC Tunnel 9 varied on the basis of Reynolds number and therefore is unique for each interchangeable nozzle. For the Mach 10 nozzle that was used in the Moraru research effort the percent noise was between 2.5 and 4% [43].

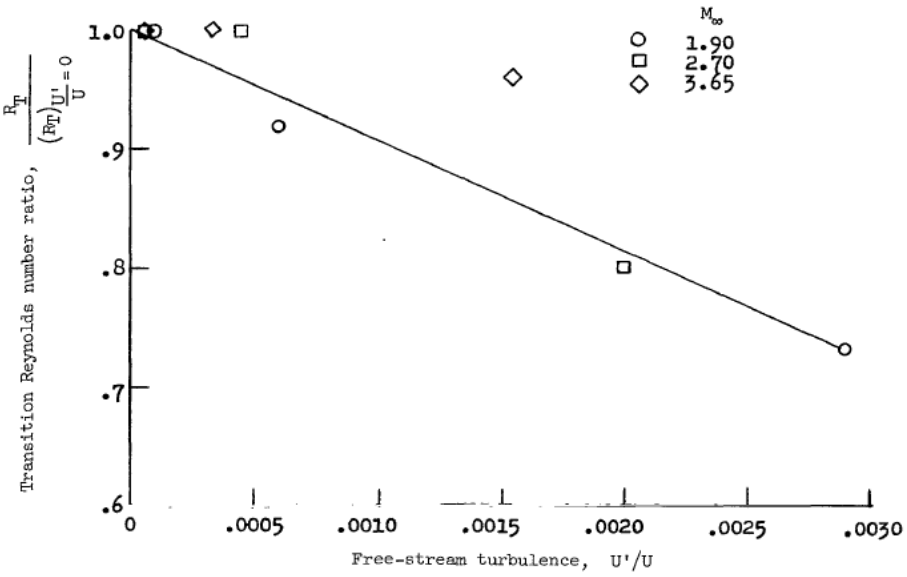

Figure 28. Effect of Turbulence Level on Transition [8]

5.3 Curvature.

The radius of curvature of the wall, R, governs the resulting Görtler instabilities as defined in Section 4.1. Mendez et al. performed DNS computations on a concave surface to investigate the effects of curvature on transition. From Figure 29, it was concluded that as the radius of curvature decreased, the critical Reynolds number was delayed. However from Figure 30, the Görtler number, governed by Equation 2.31, remains approximately unchanged. Since the Görtler number is a ratio of centrifugal forces to viscous forces, the Mendez et al. experiments indicated that for a given concave geometry, a transition point can be related through the Görtler number.

The nature of a Görtler instability can be described in terms of an upwash and a downwash region. The upwash movement pushes the low velocity flows to the wall and the downwash movement pushes the high velocity fluid from the freestream towards the wall [57]. The combination of these regions creates the vortical structures seen in Figure 14. Figure 31 indicates how the coefficient of friction was influenced by the radius of curvature. In the upwash region, represented in the blue line, the coefficient of friction was barely influenced by the increasing radius of curvature. On the other hand, in the downwash region represented in the orange line of Figure 31, initially the coefficient of friction increased with increased radius of curvature until a distinct maximum was reached. Then the coefficient of curvature began to decrease. In general, as the radius of curvature decreased, the coefficient of friction increased [57].

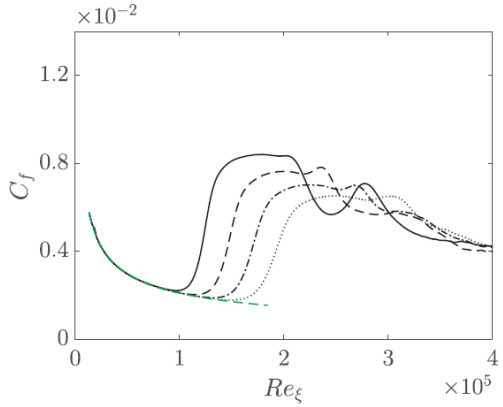

Figure 29. Coefficient of Friction versus Reynolds number at the start of transition (used with permission) [57]

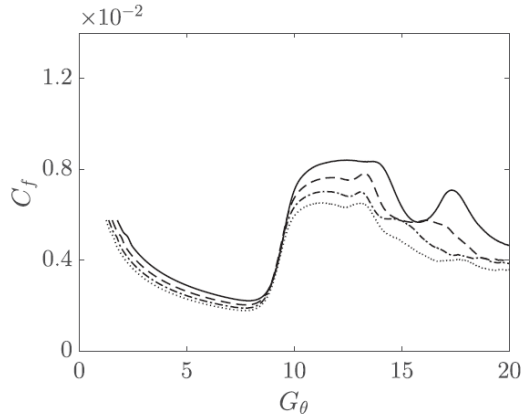

Figure 30. Coefficient of Friction versus Görtler number (used with permission) [57]

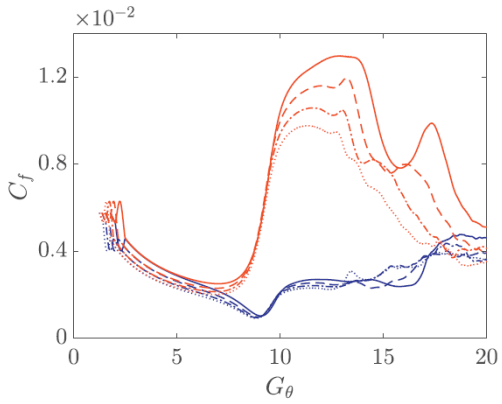

Figure 31. Coefficient of Friction at upwash and downwash versus Görtler number (used with permission) [57]

5.4 Bluntness.

In general boundary layer studies, for a cone to be considered sharp the nose radius, R_N, should be less than one millimeter. Cones with nose radii higher than the sharp nose cone criteria are considered blunt. Relating this definition of sharp and blunt cones to the six, 7° half-angle cones tested by AEDC Tunnel 9, the first cone with the nose radius of 0.152 mm is the only classically defined sharp cone.

In general, increasing the nose radius resulted in a delay in transition because the flow conditions behind the normal shock that formed on the front of the nose caused a

decreased local Reynolds number [8]. This trend was attributed to the reduction of the local Reynolds number resulting from total pressure losses through the bow shock and experiments by Stetson provided substantiation [79]. Using the Reynolds number as a tool for interpreting the effects of nose bluntness initially provided valuable insight to the hypersonic boundary layer transition over blunt cones problem. However, it is an over simplification of the problem to use the Reynolds number correlations as the only interpretation parameter. Stetson observed that as the nose bluntness increased from sharp to blunt there was a shift in the dominant mechanisms to transition [79]. Therefore, the Reynolds number correlations must be considered in combination with other parameters when analyzing boundary layer transition over blunt cones. Specifically, Stetson analyzed the boundary layer transition for blunt cones in terms of the amount of entropy layer which had been entrained in the boundary layer.

Stetson conducted experiments in the Flight Dynamics Laboratory (FDL) Mach 6 wind tunnel with 8° half-angle cones [79]. The cones had an increasing bluntness ratio of 0, 0.01, 0.02, 0.03, 0.04, 0.05, 0.10, 0.15, 0.20, 0.25, and 0.30 where bluntness ratio (B) was defined as

$$B = \frac{R_N}{R_B} \tag{2.36}$$

where R_N was the nose radius and R_B was the base radius [79]. As the bluntness ratio increased, Stetson defined three regions by the consistent trends observed in the experimental data. The three regions were defined by the surface distance to the onset transition location for blunt cones (X_{TB}) divided by the entropy layer swallowing distance (X_{SW}) [79]. Region 1 had the least amount of bluntness and Region 3 had the most amount of bluntness.

The first region was defined as $X_{TB}/X_{SW} \approx 1.0$ [79]. In this first region the entropy layer was completely or near completely swallowed by the boundary layer [79]. This first region occurred on cones with small bluntness ratios. As the nose

radius increased from sharp to blunt the transition location moved further down the frustum and the transition Reynolds number slightly decreased [79]. The behavior of this region was described by the established second mode dominated transition precedent. Initial increases to the nose radius resulted in an increased transition location (X_T). The AEDC Tunnel 9 data between the nose radii of 0.152 mm and 5.08 mm presented in Figure 3 displayed identical behavior to the first region as defined by Stetson.

The second region was defined as $X_{TB}/X_{SW} \approx 0.10$ [79]. As the nose radius continued to increase, the transition Reynolds number greatly reduced [79]. In the first region the Reynolds number only slightly reduced and therefore the large reduction in Reynolds number signaled to Stetson that there was a change in dominant factors influencing transition [79]. The local unit Reynolds number was influenced by the freesteam Mach number as well as the location within the entropy layer [79]. Stetson researched the adverse pressure gradient which forms to correct the over-expansion of the high pressure gas generated by the bow shock as the dominant factor influencing transition and concluded that the adverse pressure gradient was not the dominate factor [79]. The factors influencing this region of transition are still not well understood.

The third region was defined as $X_{TB}/X_{SW} < 0.03$ [79]. Increasing the nose radius to considerable bluntness resulted in four observations. First, the transition location data was not repeatable [79]. Second, on the axi-symmetric cones the asymmetric transition patterns occurred on experiments with zero angle of attack [79]. Third, the transition region was much longer than the other two regions [79]. Fourth, the frustum transition was sensitive to the roughness on the nose [79]. Stetson correlated the third region to distributed surface roughness on the nose [79]. Stetson's success in correlating the third region to distributed surface roughness on the nose fuels the

motivation in computationally simulating distributed surface roughness on the AEDC Tunnel 9 blunt cones.

Figure 32 plots the start of transition Reynolds number based on the streamwise coordinate (Re_{ξ_T}) against the Reynolds number based on nose radius (Re_{R_N}) for the Stetson experiments and experiments performed by Aleksandrova et al. [1], [79]. Both experiments were performed at Mach 6 and the diamond data points correspond to the Stetson experiments and the star data points correspond to the Aleksandrova et al. experiments. The data demonstrated the two regions of bluntness delineated at $Re_{R_N} = 1.3 \times 10^5$ [63]. In the region less than $Re_{R_N} = 1.3 \times 10^5$, the transition location moved downstream as the nose radius increased. In the region greater than $Re_{R_N} = 1.3 \times 10^5$, the transition location either ceased to move downstream or reversed and moved upstream [63]. The Aleksandrova et al. experimental data bolstered the three regions defined by Stetson. The qualitative similarities are definitive, and the quantitative differences are hypothesized to be due to disturbances caused by distributed surface roughness on the nose or differences in freestream tunnel noise.

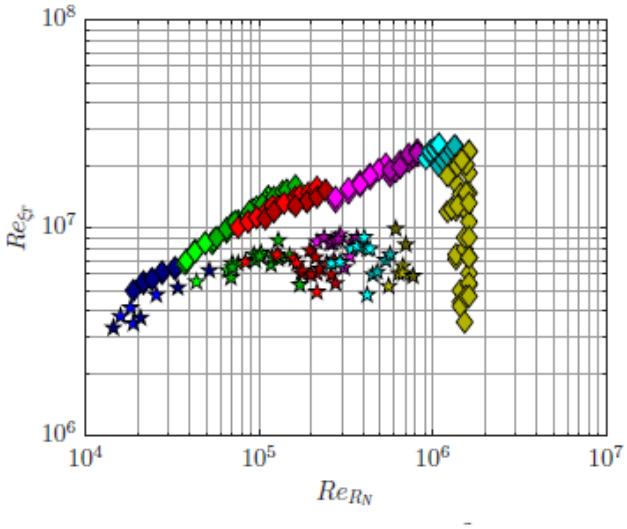

Figure 32. Transition Reynolds Number Based on Freestream as a Function of the Nose Reynolds Number [63]

Paredes et al. explored the possibility of entropy layer swallowing as a possible source of boundary layer instabilities for the AEDC Tunnel 9 7° blunt cones from Figure 1 and found that for all nose radii cases, transition occurred before the entropy layer is swallowed [63]. The analysis of the pressure power spectral density (PSD) did not reveal amplification of entropy layer instabilities for the AEDC Tunnel 9 configurations. Therefore, the non-modal mechanisms caused by distributed surface roughness are still the leading hypothesis for cause of transition for the AEDC Tunnel 9 experiments.

Due to the multiplicity of dominant factors within all boundary layer transition problems it is often difficult to isolate the cause of transition. Stetson documented this multiplicity between bluntness and surface roughness in [79]. For cones with a small amount of nose bluntness, the level of roughness on the nose had no effect on the transition [79]. However, for cones with a large amount of bluntness, smaller levels of surface roughness resulted in higher transition Reynolds numbers or completely laminar flow over the test article. The conceptualization of this research effort is an artifact of the combined study of bluntness and roughness performed by Stetson [79] as well as the successful distributed surface roughness research efforts conducted by Dinzl on the HIFiRE-5 [21].

5.5 Angle of Attack.

The angle of attack (AOA) does not affect whether transition will occur, but it does affect where the transition location occurred on the body. This section is limited to the discussion of the effects on angle of attack on axi-symmetric cones. Figure 33 shows an aggregate of sharp nose cone transition data at angle of attack created by Stetson and some definitive trends emerged. Increased AOA caused the transition front to move away from the nose on the windside and caused the transition front

to move towards the nose on the leeside [54]. The transition front on sharp cones moved away from the nose on the windward ray because the angle of attack caused an increase in local Reynolds number and decrease in the local Mach number [78]. Furthermore, the boundary layer for sharp cones was more stable on the windward side and less stable on the leeward side [58]. Stetson stated the cause of the differing magnitudes in Figure 33 is unknown [78]. As mentioned previously, the factors that affect transition are numerous and not additive. Therefore, it is likely that each of the experiments listed in Figure 33 had a unique surface roughness level and were tested in a conventional wind tunnels each with a unique level of freestream noise. Other additional influencing factors could have led to the angle of attack effecting the transition location with a different magnitude.

Stetson performed angle of attack experiments on an 8° half-angle cone at Mach 6. The experimental cones had both a sharp tip nose and blunt nose tips with the bluntness ratios of 0.02, 0.05, 0.10, and 0.15 [78]. The bluntness ratio was defined as nose radius divided by the base radius in Equation 2.36. In Figure 34, the transitions distance (X_T) was normalized by the transition distance on the sharp nose 8° half-angle cones at zero angle of attack and was plotted against the angle of attack (α) normalized by the cone half-angle (θ_c). In Figure 34, the sharp nose cone transition followed the trends outlined previously; however, the blunt nose cones trends differed. For small angles of attack the trend matched the sharp nose cone trend and there was rearward movement of the transition location. For larger angles of attack, the trend reversed and there was forward movement of the transition location. Stetson postulated that the cause of this trend reversal was due to the boundary layer profile shape; specifically, that a blunt nose cone has a more stable shape with angle attack [78]. Moraru conducted an angle of attack study for the AEDC Tunnel 9 geometries of interest to this research effort and the results are available in Reference [59].

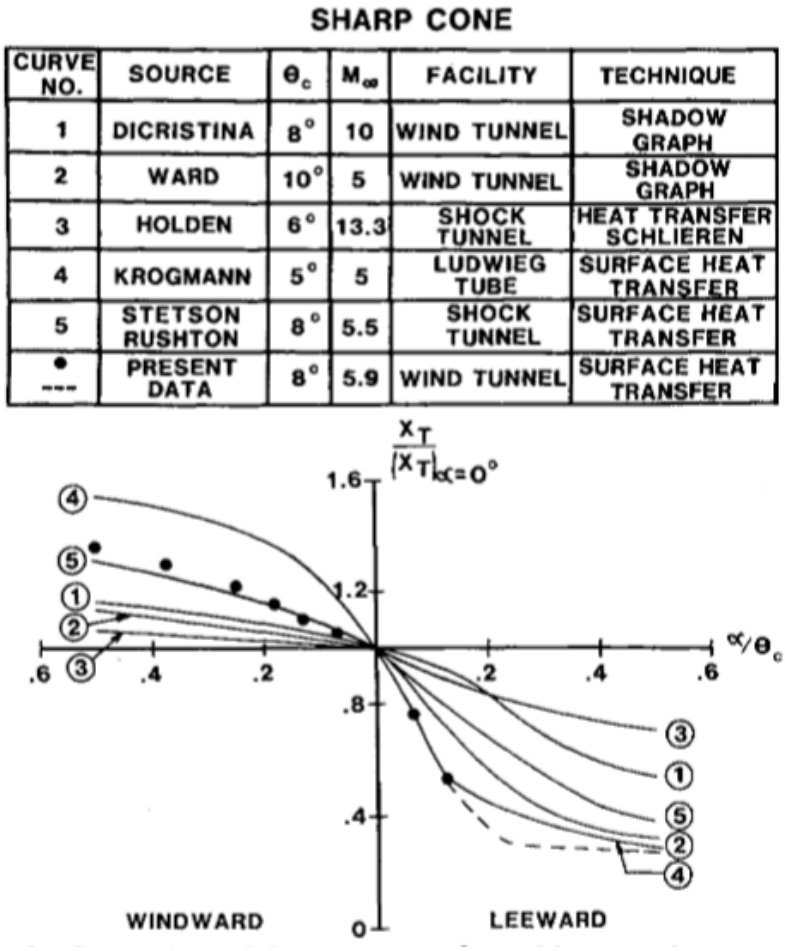

Figure 33. Transition Comparions on a Sharp Nose Cones at Angle of Attack [78]

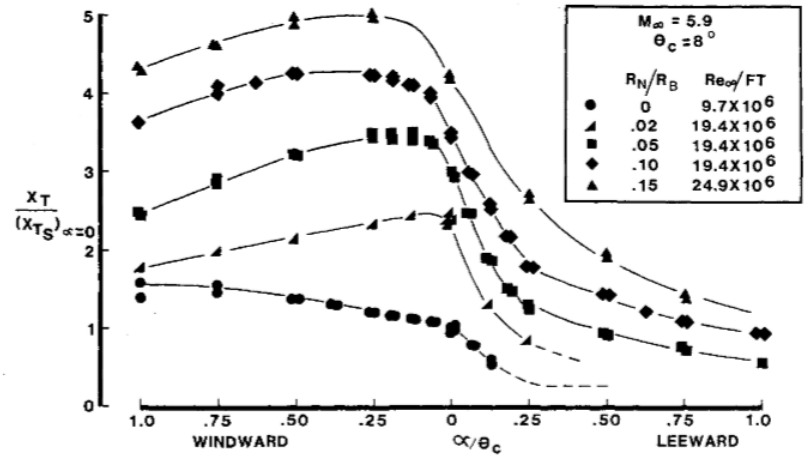

Figure 34. Transition on Sharp and Blunt 8° Half-Angle Cones [78]

5.6 Suction and Blowing.

Suction and blowing are boundary conditions which can be used to control the boundary layer to prevent the separation of turbulent flow. Tangential blowing is to add energy to the fluid in the boundary layer by tangentially blowing higher velocity fluid out from inside the body [69]. As a result, the boundary layer kinetic energy and freestream kinetic energy match and the risk of separation is therefore reduced.

Suction exists in two forms: distributed suction and discrete suction [5]. Distributed suction occurs in heavily porous materials and therefore this type of suction is excluded from this discussion. Discrete suctionis used as a method of decreasing the boundary layer height. When the boundary layer height is reduced, the resultant laminar profile has a higher limit of stability [69]. The relevant length scale for Reynolds number calculation when determining the boundary layer transition is often the boundary layer height (Re_δ)

$$Re_\delta = \frac{U_\infty \delta}{\nu} \tag{2.37}$$

where U_∞ is the freestream velocity, δ is the boundary layer height, and ν is the kinematic viscosity. Thus, as the boundary layer height decreases so does the Reynolds number. By reducing the boundary layer height the Reynolds number can be reduced enough to delay or prevent transition according to the Orr-Sommerfeld Equation [8].

Azim et al. provided a numerical investigation on a NACA 4412 airfoil that provided contextual parameters for using suction as a means of delaying transition [5]. Figure 35 demonstrates that at low AOA the effects of suction in reducing the lift to drag ratio was high and at high AOA the effects of suction in reducing the lift to drag ratio were minimal. Therefore it can be concluded that it would be insufficient to use suction throughout a full flight trajectory as a means of preventing separation.

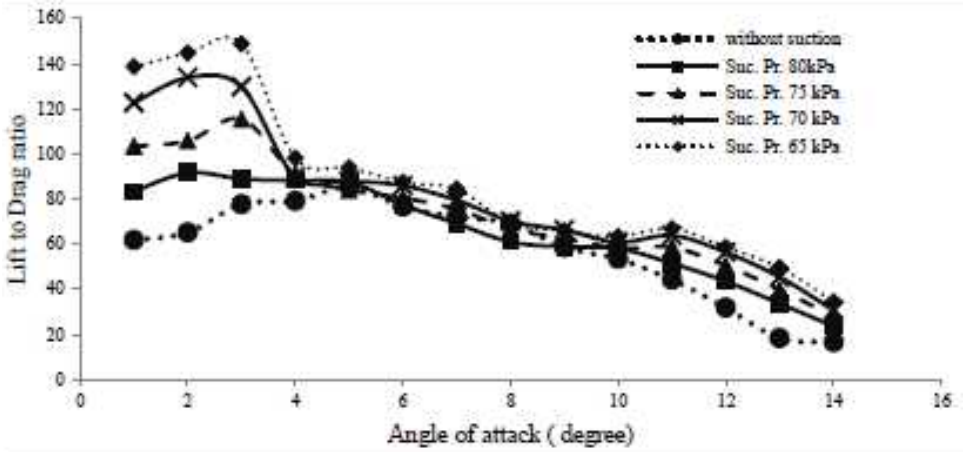

Figure 35. Change of lift to drag ratio with AOA for different suction pressures [5]

5.7 Wall Temperature.

Cooling is heat transfer from the boundary layer to the wall while heating is heat transfer from the wall to the boundary layer. In general, cooling has a stabilizing effect for instabilities in the boundary layer and heating has a destabilizing effect for instabilities in the boundary layer [8]. The reason for this phenomenon can be found in the relationship between temperature and viscosity. Equation 2.38 is the velocity profile at the wall of a flat plate at zero angle of attack [69]

$$\left(\frac{d^2U}{dy^2}\right)_w = -\frac{1}{\mu_w}\left(\frac{d\mu}{dy}\right)_w\left(\frac{dU}{dy}\right)_w \tag{2.38}$$

In Equation 2.38, the velocity gradient at the wall, $\left(\frac{dU}{dy}\right)_w$ is positive definite. If the temperature gradient at the wall is negative (i.e. cooling) then $\left(\frac{d\mu}{dy}\right)_w$ will also be negative. Thus, for cooling the velocity profile at the wall is positive. This positive profile is not sustained through the full height of the boundary layer [69]. The positive profile inside the boundary layer changes via a point of inflection, $\frac{d^2U}{dy^2} = 0$.

In experiments performed by Fedorov et al. on a 7° half-angle cone with a sharp nose radius the strong relationship between wall heating and cooling and the boundary layer height was exemplified. Fedorov et al. chose to run Mach 10 experiments which employed weak and strong cooling and heating and compared the results to a baseline of no heating source [25]. In Figure 36, the stabilizing effects of cooling resulted from the reduced boundary layer thickness. Conversely, the weak and strong wall heating caused the boundary layer thickness to increase from the no heating source line in Figure 36. Thus wall heating had a destabilizing effect on boundary layer transition. In Section 4.3, it was established that first mode instabilities act opposite to each other under the influence of wall cooling. The trends stated in this section for wall heating and cooling apply to second mode dominated flows.

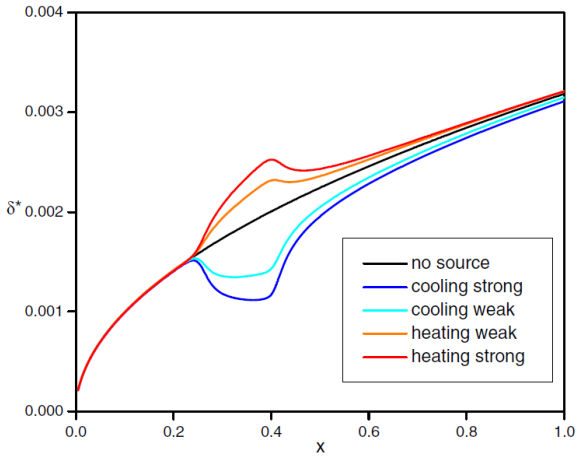

Figure 36. Effects of Wall Heating and Cooling on Boundary Layer Thickness (used with permission) [25]

6 Transition Prediction Methodology

Many of the current transition prediction methodologies are circumstantial and each existing prediction methodology applies to a limited subset of cases. The best models exist for second mode dominated, sharp nose cones. For the blunt nose cases,

which are applicable to this research effort, commonly used transition prediction methods fail to accurately predict transition. In the subsequent sections the merits and applicability of common prediction transition methodologies are discussed. Since there is no transition prediction methodology that simultaneously encompasses all linear and nonlinear effects that can lead to transition, direct numerical simulation (DNS) became the preferred methodology for investigating distributed surface roughness has the reason behind the increased heat transfer data presented in the experimental results from AEDC Tunnel 9 in Figure 2. However, even the DNS method of transition prediction methodology is only as good as the model of the influencing factors.

6.1 Correlations Based on Roughness Height.

According to Braslow, Schiller was the first to propose a Reynolds number (Re_k) based on roughness height (k) and friction velocity (v_*) [8].

$$Re_{Sc} = \frac{\rho v_* k}{\mu} \tag{2.39}$$

$$v_* = \sqrt{\frac{\tau}{\rho}} \tag{2.40}$$

$$\tau = \mu \frac{du}{dy} \tag{2.41}$$

Where τ is the local shear stress, ρ is the freestream density, μ is the freestream dynamic viscosity, and $\frac{du}{dy}$ is the slope of the linear portion of the laminar boundary-layer velocity profile. The definitions for the friction velocity and the local shear stress can then be substituted into the Schiller Reynolds number (Re_{Sc}) to obtain the following relationship.

$$Re_{Sc} = \sqrt{\frac{\mu \frac{du}{dy}}{\rho}} \frac{\rho k}{\mu} \tag{2.42}$$

Equation 2.42 was simplified to obtain the definition for velocity at the top of the roughness element (u_k)

$$u_k = k\frac{du}{dy} \tag{2.43}$$

where k is the roughness element height. The Schiller Reynolds number was then related to a roughness height Reynolds number (Re_k) by the following derivation [8].

$$Re_{Sc}^2 = \frac{\mu\frac{du}{dy}}{\rho}\frac{\rho^2 k^2}{\mu^2} = \frac{du}{dy}\frac{\rho k^2}{\mu} = \frac{u_k}{k}\frac{\rho k^2}{\mu} = \frac{\rho u_k k}{\mu} \tag{2.44}$$

$$Re_{Sc} = \sqrt{Re_k} \tag{2.45}$$

Figure 37 plotted the Reynolds number based on roughness height for transition ($Re_{k,t}$) against the roughness height nondimensionalized with the diameter of the roughness element (d). For the low speed data provided in Figure 37, there was a factor of two relationship between the square root of Re_k and the nondimensional roughness height [8]. This integer correlation between the Schiller Reynolds number and nondimensional roughness height is often used to indicate the ability of a discrete roughness element (DRE) to cause transition.

However, as Schneider identified this proportional relationship only applies to the linear region of the boundary layer and therefore this relationship is not applicable to hypersonic flow [74]. The parameter Re_k was initially a step forward in the transition prediction area of knowledge because it provided the ability to indicate if a roughness element would induce turbulence. As transition continued to be researched, it became clear that simple parameters such as Re_k at the start of transition and roughness height would not suffice because relationships with only two parameters fail to include enough factors to accurately describe the problem.

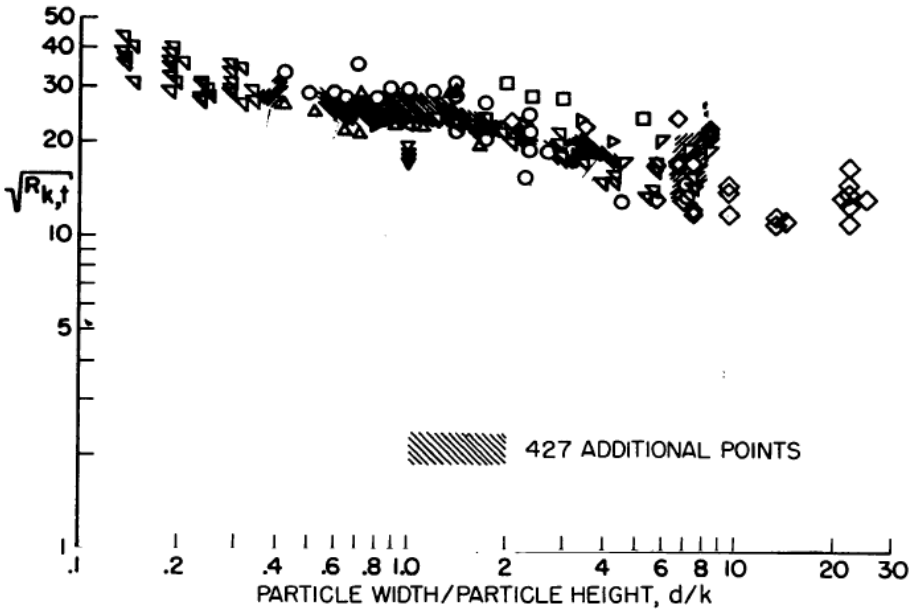

Figure 37. Transition Correlation [8]

6.2 Mack's Amplitude Method.

Mack's Amplitude Method, or the e^N Method, has been widely used to study hypersonic boundary layer transition and is the bedrock method of Linear Stability Theory (LST). The e^N method is employed by solving the Linearized Navier-Stokes Equations for spatial eigenvalues which represent the growth rate of the disturbance at a streamwise location. The N factor is a representation of how much the instability has grown at a given amplitude of the instability wave in comparison to the max amplitude of the instability wave. The N factor is calculated by

$$e^{N(f,s)} = \frac{A(f,s)}{A_0(f)} \tag{2.46}$$

where $A(f,s)$ is the amplitude of a disturbance at a particular streamwise location (s) and $A_0(f)$ is the amplitude of the initial disturbance. This method was built on the assumption that the perturbations are small and the interactions of the perturbations

(i.e. nonlinear effects) are negligible. Therefore the Navier-Stokes equations were linearized.

The e^N Method is a semi-empirical method that is used to correlate the start of transition to the integrated growth of linear instability waves. Larger N factors caused by larger forcing functions cause transition to occur earlier. As the frequency of the forcing function is increased, the e^N methodology yields decreased N factors. Consequently, smaller N factors delay the onset of transition. Typical transition N factors for conventional wind tunnel experiments on axi-symmetric cones with sharp noses are between 5-10 [20]. The advantages of using the e^N Method are that its wide usage and understanding coupled with the accurately modeled linear amplification process of the modal waves [83]. Thus the e^N method proved effective for predicting transition onset location for sharp nose cones which were dominated by second mode instabilities. However, for blunt nose cones, transition has been observed at much lower N factors. The reason for observing transition at lower N factors is related to the disadvantages of the e^N Method. These disadvantages are that the receptivity process, the possible decaying process of modal waves in the linear stage of evolution, nonlinear interaction, nonlinear breakdown effects, and roughness interaction are neglected [83]. Depending on the problem, only accounting for the linear growth of an instability might be appropriate because the nonlinear effects are negligible; such as sharp cones with the transition process dominated by second mode instabilities. Additionally, accurate application of this method requires accurate measurements of initial disturbances (A_0) to produce a realistic N factor and these measurements become even more uncertain at high speeds.

In accordance with Mack's methodology, integration is performed over the range of frequencies (f) that represented the unstable second-mode band $[f_1, f_2]$. This

integration yields the normalized second-mode amplitude at location s [53].

$$A^2(s) = \int_{f_1}^{f_2} a_0^2(f) e^{2N(s,f)} df \tag{2.47}$$

Where $A(s)$ is the pressure fluctuation root-mean-squared (RMS) normalized by the mean edge pressure at a specific streamwise surface coordinate and $a_0(f)$ is the pressure spectral amplitude on surface normalized by mean edge pressure for a specific frequency at the stagnation point. Traditionally, the N factor is obtained from linear stability theory or from application of the Parabolized Stability Equations (PSE). However, Marineau et al. [54] asserted that the integral in Equation 2.47 can be simplified to

$$A_T^2 = C_1^2 a_0^2(f_T) e^{2N(f_T)} \Delta f \tag{2.48}$$

where A_T is is the pressure fluctuation RMS normalized by the mean edge pressure at the start of transition, $a_0(f_T)$ is the pressure spectral amplitude on surface normalized by mean edge pressure for the frequency at the start of transition, and Δf is the second-mode bandwidth. The constant C_1 is an empirical constant that Marineau et al. set to 0.48 [53].

For the AEDC Tunnel 9 measurements, A_T is assumed as 60% of the maximum amplitude (A_{max}) and the maximum N factor for the start of transition (N_T) is calculated through the following relation.

$$N_T \approx ln\left(\frac{1.25 A_{max}}{A_0(f_T)}\right) \tag{2.49}$$

Using these relations, Marineau et al. [53] built an algorithm to predict transition location that converged in less than ten iterations with a standard error of 14% from

experimental data. Marineau et al. also repeated the calculations using the standard N factor of 5.5 for a conventional noisy tunnel and found a standard error of 43% in transition prediction [53]. Evidently, the empirical relations that Marineau et al. developed greatly reduced the standard error in the transition location predictions and the standard N factor of 5.5, which was based on no specific level of freestream noise fluctuations, was only a mediocre estimate. However, the Marineau et al. relationships relied on the empirical value of C_1 and the tunnel specific empirical relationship A_T was 60% of A_{max}. Therefore, these equations are only applicable to AEDC Tunnel 9 and every hypersonic tunnel would have to develop an unique set of empirical relationships. While this method has proven useful for the practical engineering happening today, it will be necessary to eventually move beyond empiricism and into solid physics for further understanding of boundary layer transition.

6.3 Pate Correlation.

The Pate correlation successfully predicted transition on sharp cones and flat plates at hypersonic speeds by using a model for the spectral amplitudes of the freestream noise [53]. This model replaced the the pitot pressure measurements used in the e^N Method with empirical relationships for conventional wind tunnels. The success of the Pate Correlation was attributed to the fact that transition Reynolds number decreased with increased noise as discussed in Section 5.2. The Pate Correlation is [71]

$$(Re_t)_\delta = \frac{48.5 C_F^{-1.40}[0.8 + 0.2(C_1/C)]}{\sqrt{\delta^*/C}} \tag{2.50}$$

where $(Re_t)_\delta$ is the Reynolds number for the end of transition based on local conditions, δ^* is the turbulent boundary layer displacement thickness in the tunnel section determined by Equation 2.3, C is the tunnel test-section circumference, C_1 is the circumference of a 30.5 $\times$ 30.5 cm tunnel and C_F is the mean turbulence skin fric-

tion coefficient in the tunnel test section. Once the Reynolds number at the end of transition is known, the Pate Noise Parameter (P_N) is calculated.

$$P_N = \frac{(Re_t)_\delta \sqrt{\delta^*/C}}{0.8 + 0.2(C_1/C)} \tag{2.51}$$

In Figure 38 the Pate Noise Parameter and the coefficient of friction (C_F) for the test section are plotted using experimental data from eleven different conventional tunnels and calculated through the Pate Correlation. Excellent agreement is seen for the sharp nose cones. Therefore the Pate Correlation may correctly predict the AEDC Tunnel 9 cone with a nose radius of 0.152 mm but this method will not be sufficient for predicting transition on the blunt nose radii of 12.7, 25.4, and 50.8 mm.

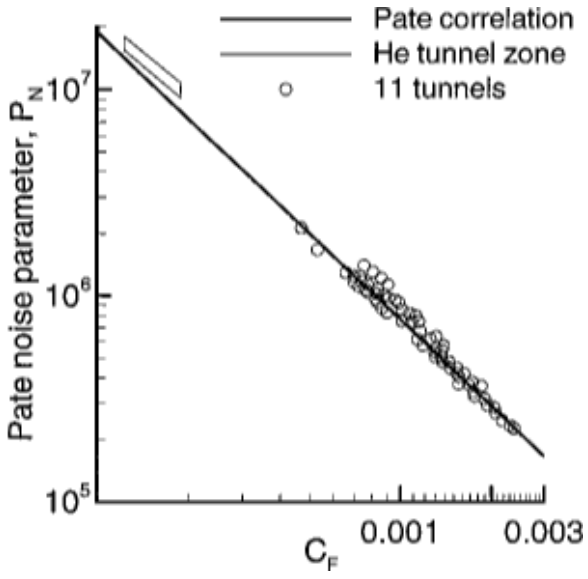

Figure 38. Correlation of Transition on Sharp Cones via the Pate Noise Parameter and Coefficient of Friction (used with permission) [71]

6.4 Parabolized Stability Equations.

The Parabolized Stability Equations (PSE) are a non-empirical method of transition prediction for modal instabilities. PSE includes some nonlinear effects and therefore has the potential to advance the mathematical models used in transition prediction. However, PSE still excludes surface roughness and internal shock physics and it is difficult to test the theory with a wide set of good data [71]. There is limited flight data at hypersonic speeds, and even with the flight data that is available it is unlikely that enough data was taken over the entire geometry to pinpoint the location of transition within reasonable certainty. On the other hand, there are more hypersonic experimental data available, but the experimental data are often plagued by freestream disturbances in the form of noise. A conventional wind tunnel has freestream noise levels of 1-5% and the flight condition freestream noise levels are one to two orders of magnitude lower. Quiet tunnels provide data at a lower noise level than the conventional wind tunnels; however, the noise level of a quiet tunnel is larger than the noise level of hypersonic flight conditions. Higher freestream noise causes transition to occur further upstream on the geometry; therefore, the hypersonic experimental data set is not suitable to verify PSE.

The most recent attempt to reduce the number of assumption made in transition prediction methodology are the biglobal and trigolbal stability methods. Global stability methods are appealing from a mathematical modeling point of view but they have a high computational cost while sustaining the same disadvantage as PSE in that they are largely unverified by viable hypersonic flight data [20]. As established in Section 4, the cause of the heat transfer increase on the AEDC Tunnel 9 7° half-angle blunt cones with nose radii of 12.7, 25.4, and 50.8 mm was non-modal. Mathematical models such as PSE, biglobal and trigobal apply better estimates for transition but still neglect key non-modal elements of this research effort; namely distributed surface

roughness. Therefore PSE, biglobal, and triglobal methods cannot be applied to this research problem.

6.5 Input Output Analysis.

Traditional Linear Stability Theory (LST) accurately predicted the transition location for sharp cones but ceased to accurately predict the transition location for blunt cones because of the assumption that all flow is parallel at the nose. For blunt nose cones, such as the 7° half-angle cones from the AEDC Tunnel 9 experiments, the curved bow shock created highly non-parallel flow at the stagnation point. The Parabolized Stability Equations (PSE) did not assume parallel flow but assumed that the baseflow does not change rapidly in comparison to the wavelength of the instability [16]. Once again, the PSE methodology was extremely effective for modal transition experienced with sharp nose cones but failed to accurately predict the transition of blunt nose cones. Currently under research by the University of Minnesota is the methodology to predict transition on blunt cones using the input-output analysis method [17]. The input-output analysis method no longer assumes parallel flow. Instead, the input-output analysis method extracts the Jacobian from the flow solver and solves for the maximum gain through input-output analysis.

Mathematically, both LST and input-output analysis start by extracting the Jacobian (A) from the flow solver which solved the linearized governing equations. If the problem were to be solved using LST, an eigenvalue solution methodology would be applied such that $\dot{x} = Ax$ where x represents the system. However, using input-output analysis, an additional term was added to the system

$$\dot{x} = Ax + Bf \tag{2.52}$$

where f is an input forcing function and B controls the magnitude and location of

forcing [16]. Additionally the system is defined by,

$$y = Cx \tag{2.53}$$

where y represents the outputs and C maps the state into the outputs [16]. The inputs and outputs are related through the Fourier transformation yielding

$$\hat{y} = C(-i\omega I - A)^{-1}B\hat{f} = H\hat{f} \tag{2.54}$$

where H controls the response to ω, the harmonic forcing frequency [16]. Then, the maximum gain is computed via

$$H = U \sum V^* \tag{2.55}$$

where U is a matrix representing the optimal response and V is a matrix representing the optimal forcing f at the input location [16]. Equation 2.55 is solved iteratively for the optimal input and output functions [16].

Figure 39 demonstrates the fundamental difference between PSE and the input-output analysis. In Figure 39a, PSE methodology is shown which allows for the instability modes to be identified and then either amplified or dampened downstream appropriately. Figure 39b demonstrates the globalized, feedback system that is the defining characteristic of the input-output analysis process which does make any limiting assumptions about the flow. The communication between the red line and the blue line in Figure 39b is accomplished through the global operator which is absent in traditional PSE. More information on the input-output analysis is available in Reference [16].

Cook et al. applied the input-output analysis method to a 7° cone with a blunt nose

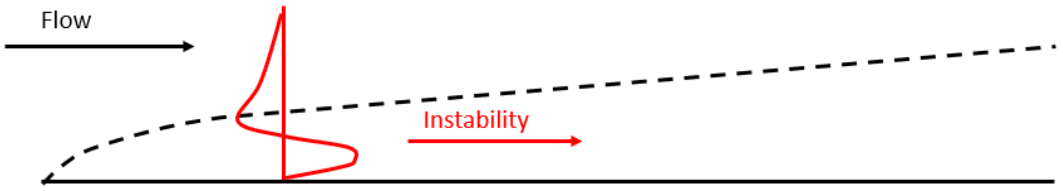

(a) PSE analysis Adapted from [16]

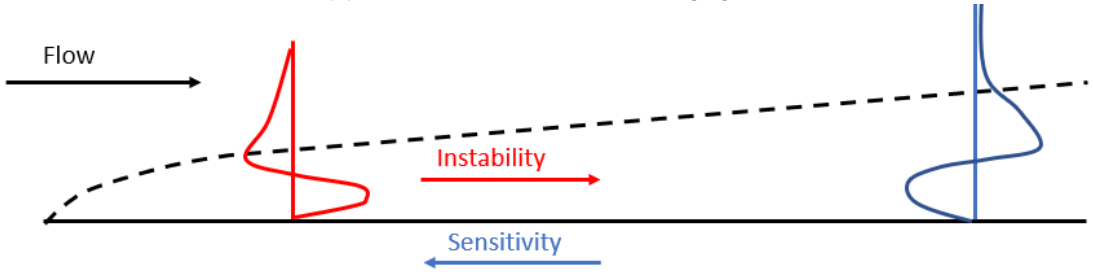

(b) Input-Output Analysis Adapted from [16]

Figure 39. Linearized dynamics of boundary layer fluctuations Adapted from [16]

radius of 381 mm at Mach 6 flow [16]. The results yielded two areas of instabilities. Transition occurred due to delayed second mode instabilities detected near the end of the cone seen in "rope-like" structure. The established second mode behavior dictates that as the nose radius is increased, the onset transition location moves downstream. However, as the nose radius increased, a second area of instabilities emerged near the nose region. These instabilities near the nose of the cone have a different structure than the second mode instabilities. Recall from Section 4.6 that Paredes et al. asserted that cones with moderate bluntness would experience two areas of instabilities. The first area would be the delayed second mode instabilities and the second area would be non-modal instabilities formed at the front of the cone [62]. Therefore the results of the input-output analysis performed by Cook et al. are in alignment with the findings of Paredes et al. with a notable exception. Cook et al. assert that the cause of the instabilities at the nose are a result of entropy layer instabilities because they exist above the boundary layer and below the entropy layer [16]. Paredes et al. concluded

that the non-modal instabilities seen at the nose were a function of surface roughness [62] and did not conform to entropy layer instability characteristics [63].

The input-output analysis is applicable to all complex flow geometries including non-modal effects and could provide breakthrough technology in the field of boundary layer transition. This analysis is only currently available for two dimensions but is under active development at the University of Minnesota to be extended for three dimensional applicability.

6.6 Direct Numerical Simulation.

Direct Numerical Simulation (DNS) solves the Navier Stokes Equations resolving all the scales of motion, with appropriate initial and boundary conditions for the entire flowfield [64]. The benefit of using DNS is the ability to analyze the entire flowfield. On the other hand, since the flowfield resolution requirements are high, the computational costs are hefty. The computational cost scales with the Reynolds number cubed [64] and therefore DNS is of limited applicability; especially at hypersonic speeds. Often times, modeling the boundary layer scales through large-eddy simulations (LES) becomes preferable to bypass the large computational cost of DNS [64] and obtain simulations that are sufficient to make sound engineering judgments. Using LES or any derivative LES models would be insufficient for capturing the instability physics in the boundary layer and would not aid in identifying the phenomenon shown in Figure 2 for the blunt nose radii. Therefore a DNS simulation was run on the 7° half-angle cones with the nose radii of 9.53 and 12.7 mm as shown in Figure 1. In efforts of combat the high computational costs only a slice of the cones were modeled and the appropriate use of boundary conditions. For more details of the modeling methodology please see Chapter 3.

Precedent for using DNS together with hypersonic wind tunnel experiments was

demonstrated in the ongoing Boundary Layer Transition (BOLT) program. The BOLT program is an Air Force Office of Scientific Research (AFOSR) program run by the Johns Hopkins Applied Physics Lab (APL) and supported by the Air Force Research Labs (AFRL), the University of Minnesota, Purdue University, and Texas A& M University. The purpose of the BOLT program is to extend modern understanding of boundary layer transition via a partnership between computational simulation and ground tests [42].

Experimental testing occurred on the BOLT Geometry at the Texas A& M University conventional wind tunnel and in Purdue University's BAM6QT Tunnel which has noise conditions much closer to hypersonic flight test than conventional wind tunnels [42]. Specific details on the modeling, wind tunnels, and data collection for each of the experiments are available in Reference [42]. The DNS computations were conducted at the University of Minnesota by Thome [42]. Consistent heat flux patterns were shown which indicated that the heat flux pattern present on the BOLT geometry in Mach 6 flow overcame the noise differential between the conventional and quiet tunnels. The BOLT program is specifically applicable to the present research effort because under the quiet flow conditions and the DNS results, there were no modal instabilities detected as the cause of transition. Thus, the BOLT program validated the current research methodology of performing a DNS to replicate the AEDC Tunnel 9 7° half-angle blunt cones laid forth in detail in Chapter 3.

7 Computational Fluid Dynamics

The majority of the CFD decisions were made to mirror the AEDC Tunnel 9 experiments and therefore the DNS specifications and justifications are provided in Chapter 3. However, the decision to use structured or unstructured grids required consultation of previous studies.

7.1 Grid Considerations.

There are two main types of grids: unstructured and structured. Unstructured grids are comprised of tetrahedra, prisms, pyramids, and hexahedral shapes providing flexibility in complex structures. On the other hand, structured grids are grids that use cells that are only hexahedral shapes. When dealing with complicated geometries or geometries with curved surfaces, unstructured grids are less work intensive to create. Due to the ease of creation, unstructured grids have gained popularity [18]. However, the unit vectors of the cell centers of tetrahedrons, prisms, and pyramids are skewed from the unit vectors of the hexahedral. Therefore the CFD solution of a finite volume solver is less accurate when using an unstructured grid. Increasing the grid density to force the unit vectors of unstructured grid elements to tend towards the Cartesian directions is an effective way to combat this concern of unstructured grids. However, many unstructured grids use structured cells in the boundary layer region to achieve a higher degree of flow alignment [18]. Regardless of the type of grid, each cell undergoes a transformation from the physical domain to the computational domain. This transformation is shown in Figure 40 for an unstructured grid. Since the computational domain is always comprised of rectangular cells, error can be introduced on unstructured grids that would not otherwise be introduced from structured grids. Unstructured grids often require lower-order flux schemes which introduces artificial viscous dissipation to remain stable. On the other hand, structured grids can apply higher-order flux schemes which contain lower viscous dissipation to achieve a more accurate solution.

Liao et al. researched the applicability of unstructured grids in boundary layer transition DNS [45]. Four geometries were considered in the Liao et al. research: flat plate, infinite swept wing, gloved wing, and full G-III aircraft. For all cases excellent agreement between the structured and unstructured grids was achieved [45]. However,

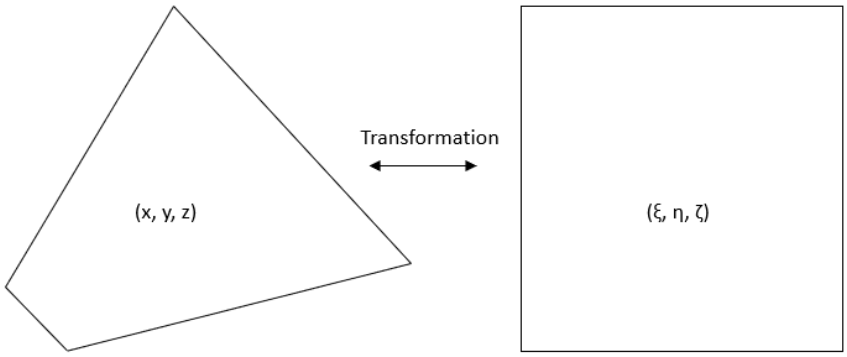

Figure 40. Transformation of a Physical Cell into a Computational Cell Adapted from [18]

the computational resources necessary for the structured and unstructured grids were not kept constant for each geometry. For example, the flat plate structured grid had 49,601 grid cells and the flat plate unstructured grid required 14.4 million tetrahedron nodes to match the structured solution [45]. The unstructured grid required several order of magnitude more cells to achieve the same solution as a structured grid and more cells require more computational resources.

Despite the ease of creation and the growing acceptance of unstructured grids, structured grids were determined to be the best grid type for the current research application. Structured grids require less computational resources due to the inherent orthogonality of the normal vectors, alignment with the shocks, allow for the proper resolution of the boundary layer, and introduce less error into the solution during the computational mapping. Discussion of the structured grids created for this research effort is available in Chapter 3 Section 2.1.

8 Concluding Remarks

Chapter 2 covered transition doctrine, modern modal theory, enumeration of factors which influence transition, transition prediction methodology, and relevant CFD considerations. From the amassed knowledge of the accredited literature, it is concluded that the increase in heat transfer data seen by the AEDC Tunnel 9 on the 7° half-angle cones with nose radii of 12.7, 25.4, and 50.8 mm in Figure 2 was non-modal. Current prediction methodology requires modal transition mechanisms to obtain credible results therefore this research effort presents a DNS as the appropriate methodology to determine the cause of transitional flow in the three most blunt nose radii cases. The methodology for the DNS calculations is presented in Chapter 3.

III. Methodology

Boundary layer transition onset data collected by the Arnold Engineering Development Center (AEDC) Hypervelocity Wind Tunnel 9 on six, 7° half-angle cones at Mach 10 with increasing nose radii demonstrated a departure from modern modal transition theory. It was expected that the transition location would move aft on the geometry as the nose radius was increased as this is the established precedent for second mode dominated transition [72]. However, as the nose radius increased from 9.5 mm to 12.7 mm the downstream movement of the transition onset location was negligible and indicated a break in the established second mode dominated precedent. The cause of the non-modal transition is not known. The goal of this research effort was to explore distributed roughness as a possible cause for the non-modal transition observed on 7° half-angle cones with the nose radius of 12.7 mm. The nose radius of 9.53 mm was also included in the simulations as an anchor point to the research as it was the last case to have experienced second mode dominated transition. To accomplish this research, Section 1 reviews the experimental details of the data of which this research effort endeavored to recreate. Section 2 covers the generation of the computational domain using LINK3D$^{\text{TM}}$ as the grid generation software. Section 3 provides relevant solution analysis for the smooth body CFD simulation using US3D as the flow solver, discusses grid independence, and narrated the creation of the distributed roughness grids. Section 4 details the approach to the time accurate simulations performed to complete the research objectives. Chapter 3 concludes with Section 5 which provides the methodology to compute the pressure power spectral density plots from the DNS results.

1 AEDC Hypervelocity Wind Tunnel 9 Experiments

White Oak, Maryland is the home of the AEDC Tunnel 9 facility pictured in Figure 41. AEDC Tunnel 9 is a nitrogen blowdown facility with a maximum test period of 15 seconds. The experimental data which framed this research effort was taken at Mach 10; however, AEDC Tunnel 9 has four commutable nozzles which achieves flow at Mach 7, 8, 10 and 14 [54]. Correspondingly, AEDC Tunnel 9 achieves unit Reynolds numbers ranging from 0.164×10^6/m to 157×10^6 /m [54]. The AEDC Tunnel 9 is known for two distinct advantages when compared to other hypersonic conventional wind tunnels. First, it has a large test section measuring at 3.6 m in length and 1.5 m in diameter which allows for large-scale models. The second advantage is the hydraulic pitching system that allows for extensive angle of attack studies. For more information on the AEDC Tunnel 9 please see Reference [56].

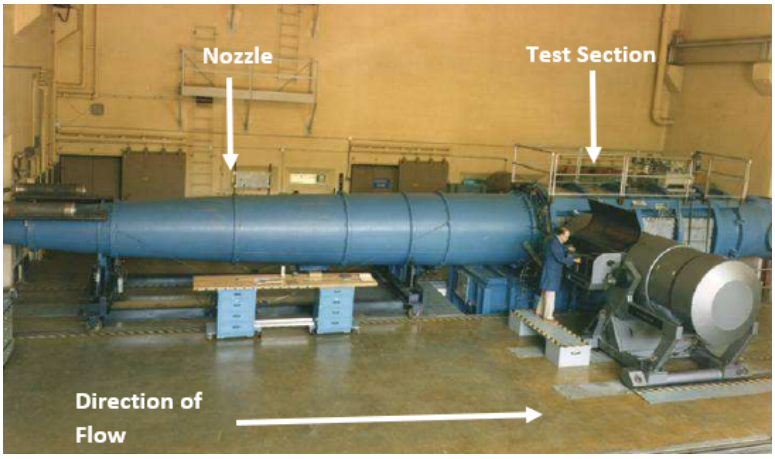

Figure 41. AEDC Tunnel 9 Test Cell with Mach 10 Nozzle [54]

1.1 Operating Conditions.

Moraru performed hypersonic boundary layer transition measurements with the Mach 10 nozzle on 7° half-angle cones with nose radii of 0.152, 5.08, 9.53, 12.7,

25.4, and 50.8 mm at varying angle of attack in the AEDC Tunnel 9 with the goal of contributing to the comprehension of the mechanisms which cause boundary layer transition by isolating specific influencing factors while taking advantage of the unique features of AEDC Tunnel 9 [59]. Moraru observed an unexplained break with modern modal transition phenomena which was also previously documented by Stetson [79]. The unexplained break with modern modal transition phenomena was observed at zero angle of attack. Therefore this research effort was performed at zero angle of attack. The operating conditions of Moraru's Run 3747 were chosen to emulate in the CFD simulation because this run had the smallest unit Reynolds number for the nose radii of interest. Moraru's Run 3747 had a unit Reynolds number of 16.9×10^6 /m, a Mach number (M) of 9.79, a total pressure (P_0) of 22.7 MPa, and a total temperature (T_0) of 983 K. The other runs at a similar unit Reynolds number had operating conditions very similar to Run 3747 and the differences were attributed to the difficulty in exact repeatability when conducting hypersonic experimental research. A smaller Reynolds number was desired for conserving computational resources as discussed in Chapter 2 Section 6.6.

Using isentropic relationships and the equation of state from Reference [4], the operating conditions were calculated and are provided in Table 1. The ratio of specific heats (γ) was set equal to 1.4 in accordance with diatomic molecules such as Nitrogen which was the test gas used in AEDC Tunnel 9. The specific gas constant for Nitrogen (R) was 296.8 $\frac{\mathrm{J}}{\mathrm{kg \cdot K}}$.

The AEDC Tunnel 9 is a pure nitrogen blow down facility therefore this research effort required the dynamic viscosity value for pure nitrogen to estimate the initial wall spacing further discussed in Section 2.3. However, for the actual simulations, the US3D flowsolver included a nitrogen viscosity model designed to simulate the pure nitrogen experimental conditions of the AEDC Tunnel 9 facility. Thus, estima-

tion of the dynamic viscosity for the initial spacing calculations was done through Sutherland's Law, an empirical relationship,

$$\mu = \mu_0 \frac{a}{b} \left(\frac{T}{T_0} \right)^{\frac{3}{2}} \tag{3.1}$$

where μ_0 is the reference viscosity at the Total Temperature. The values of a and b were empirical relationships defined as

$$a = 0.555 T_0 + C \tag{3.2}$$

$$b = 0.555 T + C \tag{3.3}$$

where C is the Sutherland Constant unique to each composition of gas. For Nitrogen, the value of C was 111. Equation 3.1 yields a dynamic viscosity of 2.99 x $10^{-6} \frac{\text{kg}}{\text{m·s}}$. Kinematic viscosity ($\nu$) was calculated from the dynamic viscosity and the density listed in Table 1, which yielded a value of 7.0 x 10^{-5} $\frac{\text{m}^2}{\text{s}}$.

The value of the specific heat at constant volume (c_v) from Table 1 was used to calculate the total enthalpy of the flow (H_0)

$$H_0 = \frac{P}{\rho} + c_v T + \frac{1}{2} V_\infty^2 \tag{3.4}$$

Equation 3.4 yielded a total enthalpy of 1.02 x $10^6 \frac{\text{J}}{\text{kg}}$ which was then used in the calculation of the Stanton number for all DNS calculations preformed in this research via Equation 1.1. By nature of Equation 3.4, hypersonic flows at flight conditions are characterized by high enthalpy value. However, the AEDC Tunnel 9 facility operates at low enthalpy conditions.

Finally, the Reynolds number based on the length of the cone (Re_L) was calculated

using the freestream velocity and the length of the cone.

$$Re_L = \frac{V_\infty L}{\nu} \tag{3.5}$$

The value of the Reynolds number based on length was 3.07×10^7. All of the conditions described in this section became the conditions for the smooth and rough grid DNS efforts.

Table 1. Operating Conditions

Variable	Value
P	616.09 Pa
T	48.74 K
V_∞	1393.23 $\frac{\mathrm{m}}{\mathrm{s}}$
ρ	0.04 $\frac{\mathrm{kg}}{\mathrm{m}^3}$
C_p	1038.8 $\frac{\mathrm{J}}{\mathrm{kg \cdot K}}$
C_v	742 $\frac{\mathrm{J}}{\mathrm{kg \cdot K}}$
γ	1.4
R	296.8 $\frac{\mathrm{J}}{\mathrm{kg \cdot K}}$
μ	7.0 x 10^{-5} $\frac{\mathrm{m}^2}{\mathrm{s}}$
H_0	1.02 x 10^6 $\frac{\mathrm{m}^2}{\mathrm{s}^2}$
Re_L	3.07 x 10^7

1.2 Uncertainty in Experimental Results.

Figure 42 depicts a representative 7° half-angle cone with the approximate placement of the sensors labeled for the experiments conducted by Moraru [59]. The sensors were placed along the 0°, 90°, and 180° rays in the streamwise direction. The red coaxail thermocouple sensors labeled in Figure 42 were utilized to measure temperature on the surface of the model [59]. From a sustained increase in temperature on the surface of the model, the onset of transitional was deduced for each nose radius tested. Labeled in green in Figure 42 were the PCB 132A31 sensors which measured fluctuations but not the mean pressure levels because these sensors had

a low-frequency response of 11 kHz and a resonant frequency greater than 1 MHz [59]. The blue and orange sensors in Figure 42 were the Kulite XCS-093 pressure transducer which were used to obtain mean pressure and pressure fluctuations [59].

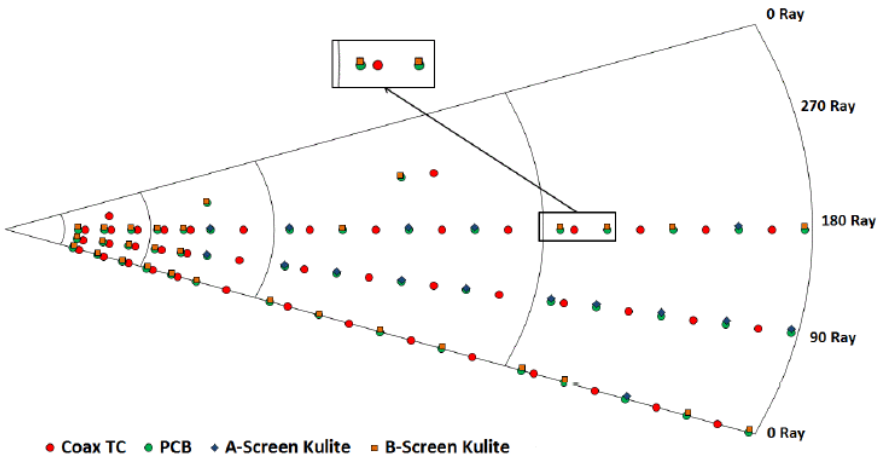

Figure 42. Flattened view of the cone showing the approximate instrumentation layout [54]

The start of transition location was estimated at the location of the first thermocouple sensor which detected a sustained increase in surface modal temperature from the laminar CFD calculations performed by Moraru and the experimental uncertainty in the start of transition location was estimated as equal to the sensor spacing of approximately 0.13 m [59]. Experimentally, the measurement of model surface temperature were definitively known at the location of each sensor and then unknown until the next sensor. Realistically, the start of transitional flow causing the increase in model surface temperature could occur between two thermocouple sensors but the start of transition cannot be estimated until the next sensor. No other uncertainties are considered in Moraru's experiments. Figure 43 demonstrates the range of plausible start of transition locations for each nose radii by plotting the nose radii (R_N) against the start of transition location (S_T) and using error bars equal to the

senor spacing. For reference, the nose radii were 0.152, 5.08, 9.53, 12.7, 25.4, and 50.8 mm and the geometries were pictured in Figure 1. It is worth noting the trend reversal of transition location seen between a nose radii of 12.7 mm and 25.4 mm fell outside of the range of uncertainty considered by Moraru and therefore the observed experimental phenomena cannot be attributed to experimental uncertainty.

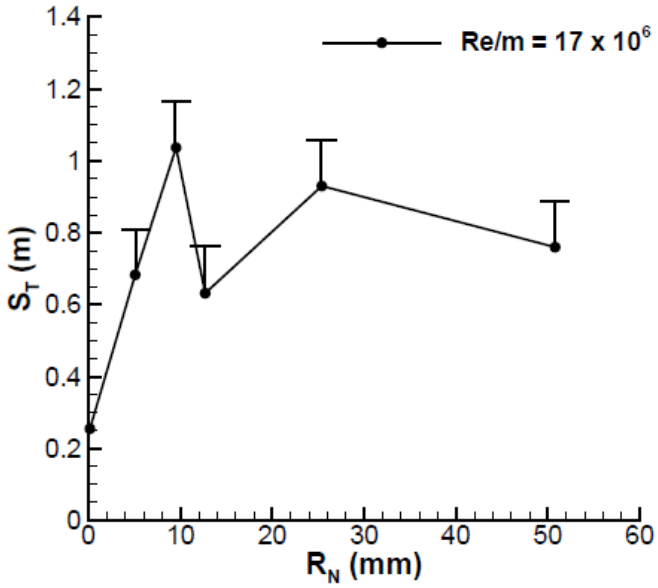

Figure 43. Start of Transition Location as a Function of Nose Radius at Re $= 17 \times 10^6$ **/m with Uncertainty Bars (used with permission) [59]**

In Figure 43 the error bars only extended in one direction and it is the present author's interpretation that this was because the uncertainty measurements only accounted for the sensor spacing. Since the location always increased in the streamwise direction, the error bars reflected that spatial increase by only extending one direction. If more sources of uncertainty were considered (i.e. instrumentation uncertainty) then the error bars would have extended the corresponding amount in both directions.

Although the possibility of unaccountable error exists in the AEDC Tunnel 9 experiments, its existence would not negate the credibility of the evidence of the

non-modal transition seen in Figure 2. The second mode dominated transition trend between the 0.152, 5.08, and 9.53 mm nose radii suddenly and completely gave way to the non-modal nature of the larger nose radii of 12.7, 25.4, and 50.8 mm nose radii regardless of the uncertainty in the onset transition location due to the sensor spacing or unaccounted for uncertainty in measured quantities.

1.3 Second Mode Instability Detection for Experimental Data.

A pressure power spectral density (PSD) calculation was performed on the experimental data from the AEDC Tunnel 9 experiments by Moraru to determine if transition was dominated by an instability corresponding to a specific frequency forced by a specific wavenumber [59]. If transition had occurred due to a specific wavenumber, then a spike would occur within a small frequency range in the PSD. The frequency at which the spike occurred would be indicative of the mode of transition if the instability was modal. If the mode of transition was non-modal then no clear spike would occur.

The pressure power spectral density shows how the magnitude of the energy changed as a function of frequency for the complete time history. Figure 44 presents the experimental frequency content for the blunt nose cones with nose radii of 9.53 and 12.7 mm calculated by Moraru [59]. The cone with a nose radius of 9.53 mm was the last cone which exhibited second mode dominated transition behavior according to Figure 2. The data which comprised Figure 44a revealed a second mode instability waves had occurred in the frequency range of 150-200 kHz. The second mode instability occurred at streamwise location (s) of 1.011 m which remained in the linear growth phase until 1.228 m [59]. The data at 1.356 m in Figure 44a suggested that the waves had begun to break down as characteristic for fully turbulent flow; however, at 1.484 m, the last sensor in the streamwise direction, a small peak formed. The

final small peak indicated that the flow was not fully turbulent flow and therefore the flow was still transitional [59]. The finding that the 9.53 mm nose radius did not achieve fully turbulent flow was in alignment with the 9.53 mm nose radius heat flux data in Figure 2 because the 9.53 mm nose radius did not "settle" into a region of full turbulent flow after the initial spike as was characteristic of the 0.152 and 5.08 mm nose radii cases.

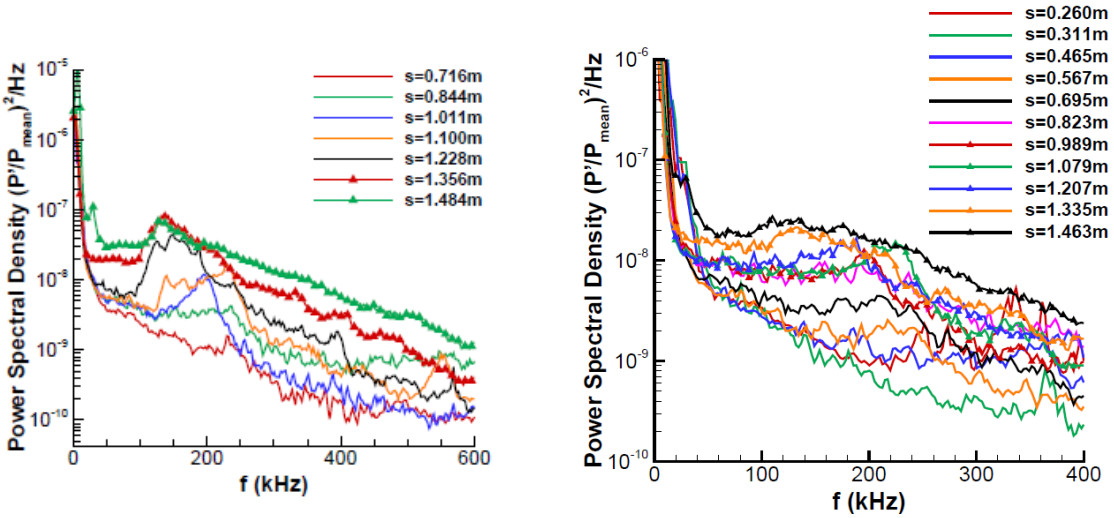

(a) R_N **= 9.5 mm [59]**

(b) R_N **= 12.7 mm [59]**

Figure 44. Pressure Power Spectral Density of 7° Axi-Symmetric Cones (used with permission) [59]

Moraru stated that no clear energetic peaks occurred which corresponded to the streamwise locations at which the heat transfer data confirmed transitional flow for the 12.7, 25.4, and 50.8 mm nose radii cases; thus indicating that the cause of transition was non-modal [59]. However, the present author identified a possible spike in the experimental pressure PSD for the 12.7 mm nose case upon which cross examination with the computational PSD is provided in Section 5. Analysis of the 12.7 mm nose radius case shown in Figure 44b revealed a possible spike in frequency content which had occurred at a frequency of approximately 200 kHz between the streamwise locations of 0.311 m and 0.567 m. The spike noted by the present author occurred

at pressure PSD values of less than 10^{-8} $\frac{1}{\text{Hz}}$ which did not constitute a second mode instability. In comparison, the second mode instability associated with the 9.53 mm nose radius case which occurred in Figure 44a occurred at a larger pressure PSD value of 10^{-7} $\frac{1}{\text{Hz}}$.

2 The Computational Domain

Grid generation required three steps: creation of a model for the geometry, design of surface and volume topologies, and mesh refinement. Figure 45 shows the model of the 7° half-angle cone with the applied boundary conditions. The goal was to create a grid to span the distance in between the cone and the shock surface where the relevant flow features formed, such as the boundary layer. Details on the topology evolution utilized to create the computational domain is discussed in Section 2.1, an explanation of the the boundary conditions assigned to the model surfaces is provided in Section 2.2 and the grid considerations made to accurately model the boundary layer is presented in Section 2.3.

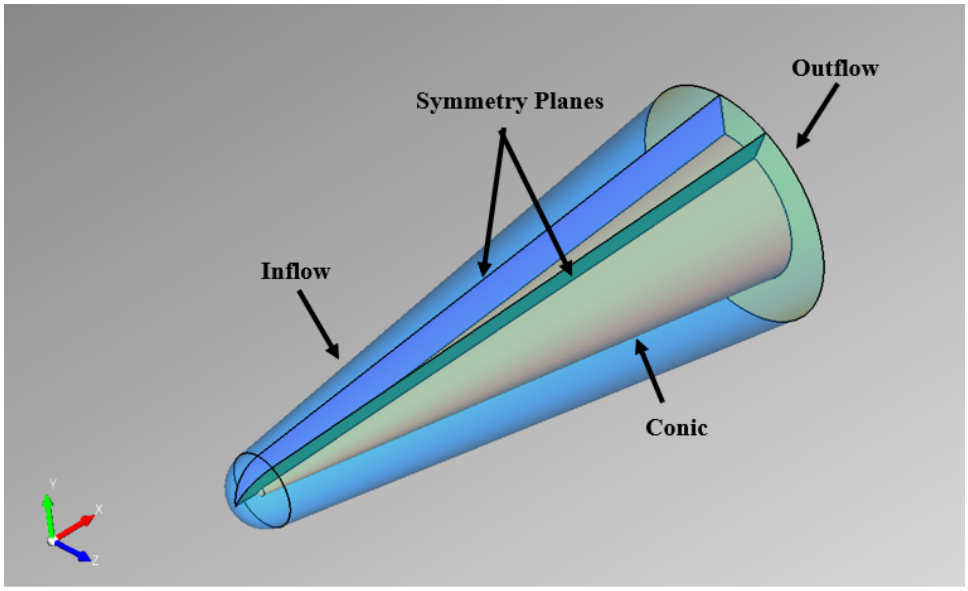

Figure 45. 7° Half-Angle Cone with Applied Boundary Conditions

2.1 Grid Generation.

The decision to create structured grids was based on the need for the utilization of less computational resources, shock alignment, proper boundary layer resolution, and the ability to use higher order flux schemes with low viscous dissipation as discussed in Section 7.1. Therefore the structured gridding software created by GoHypersonic Inc, LINK3D^{TM}, was chosen as the grid generator tool. To create the computational domain between the surface of the cone and the surface of the shock surface, a two-dimensional topology was created on the surface of the cone and extruded in the third direction to the shock cone. The three-dimensional extrusion created the volume mesh. The grid was generated from the topology. Two levels of refinement were generated per nose radius (R_N) for a total of four smooth body grids. The coarse grid contained 62 millions cells and the fine grid contained 124 million cells. The decision to not make a third level of refinement, either more coarse or more fine, was based on the resource limitations of the US3D code, the findings of the instability resolution case study discussed in the present section, and the numerical evidence provided in the grid convergence study provided in Section 3.3.

An instability resolution case study was conducted on the grids produced in LINK3D^{TM} to determine if the grid would be able to capture appropriate frequency content so that the DNS results could be compared to the experimental results for qualitative similarities. Appropriate frequency content was determined from the experimental pressure PSDs provided in Figures 44a and 44b. For a nose radius of 9.53 mm the maximum frequency collected was 600 kHz; however Figure 44a revealed that a peak of 150-200 kHz would be a frequency range of particular interest. The nose radius of 12.7 mm had a maximum collected frequency of 400 kHz with a possible peak in frequency occurring at 200 kHz. Therefore, the maximum collected frequency for the 9.53 mm case was 600 kHz and the maximum collected frequency for the 12.7 mm

case was 400 kHz. The frequencies of interest fall below the maximum collected frequencies and therefore were automatically appropriately accounted in the instability resolution case study.

Instability resolution was defined as the number a grid cells an instability of a particular frequency would occupy on the grid. Two previous distributed roughness DNS research efforts informed the definition of sufficient instability resolution for the current research effort. In the HIFiRE-5 DNS conducted by Dinzl, sufficient grid resolution was achieved when the highest frequency of interest obtained an instability resolution of 15 grid cells on the grid with the highest grid cell density [20]. Additionally, the DNS research effort conducted by Kostak et al. on the AFOSR Boundary Layer Transition (BOLT) geometry declared sufficient grid resolution when the instability resolution equaled 10 grid cells at the highest frequency of interest [42]. For the current research effort, the Kostak et al. measure of sufficient grid resolution was applied. The fine grids were deemed acceptable when the instability resolution achieved 8-10 cells and the coarse grids were deemed acceptable when the instability resolution reached 2-3 cells. In effect, the coarse grid was designed to reliably detect instabilities and the fine grid was designed to reliably detect instabilities and allow for their evolution to be observed. Since the coarse grid was designed to reliably detect instabilities, a coarser grid would be of little use to this research effort. If a finer grid was created, then the Dinzl standard of an instability resolution of 15 cells could have been applied. However, due to the flow solver limitation a grid above 200 million cells was impermissible. Therefore the largest grids were restricted to 124 million cells. A full discussion of all of the factors pertaining to the grid size decision is available in Section 3.3.

To determine the number of spatial grid cells an instability at the maximum collected frequencies of 400 or 600 kHz would occupy, a sample grid cell was chosen

on the nose, on the first third of the cone body, and on the last third of the cone body to measure the cell spacing, Δx. This distance represented a sample wavelength in the following relations. The frequency (f) of a disturbance is related to the wave number (k) by

$$k = \frac{2\pi f}{v} \tag{3.6}$$

where v is the velocity and subsequently the wavelength (λ) can be calculated through the following relationship.

$$\lambda = \frac{2\pi}{k} \tag{3.7}$$

Equation 3.6 was combined with Equation 3.7 to create an equation for the maximum supported frequency per grid cell.

$$\lambda = \frac{v}{f} \tag{3.8}$$

The ideal maximum supported frequency would be multiples of the maximum collected frequency measured from the pressure PSD calculations. To obtain the number of spatial grid cells a temporal frequency would travel, assuming similarly sized neighboring cells, the maximum supported frequency was divided by the maximum collected frequency or the frequency of interest depending on the nose radius. The result yielded the minimum number of grid cells an instability with the highest collected frequency would occupy spatially on the grid. This process was performed on all grids generated for this research effort and the results of the wavenumber study drove the evolution of the topology and constituted the criteria of an acceptable topology for the final iteration of topology design.

Computational resource availability was in the forefront of experimental design work for this research project. High computational resources were needed to complete a DNS at a unit Reynolds number of 16.9×10^6 /m. Therefore the size of the computational domain was an early question of critical importance. Similar research

efforts, such as the HIFiRE-5 DNS completed by Dinzl, used a quarter slice of the geometry [21]. However, the 7° half-angle cones used in this research effort were axi-symmetric and therefore did not produce inhomogeneous flow in the azimuthal direction. Therefore, the slice of the cone was not limited to the axis plane symmetry. Furthermore, to achieve proper instability resolution in the spanwise direction for the coarse (2-3 cells) and fine (8-10 cells) grids using a quarter geometry, an unavailable amount of computational resources would have been necessary. Therefore, a 30° slice was chosen as the computational domain for this research effort.

A singularity is a grid point comprised of any number of topology lines other than the standard four lines. Singularity points are useful for turning the grid to meet the needs of curved geometry while maintaining high flexibility for grid cell density. However, a singularity adds skew to the cells. Skew is defined as how far the angles of the hexahedral elements were shifted from 90° and the metrics used by LINK3D^{TM} to measure total skew of the grid are minimum orthogonality and maximum stretching. The minimum orthogonality metric is an average of how far away the grid cells are from the ideal case of ninety degrees. The maximum stretching metric is an average of how different the three dimensional grid cell dimensions are from a perfectly symmetrical hexahedron. Ideal topologies have orthogonality and stretching numbers of one. When singularities are employed on a grid topology, the hexahedral elements are stretched to fill the awkward shapes forced by the singularity. The first topology, shown by the black lines in Figure 46, attempted to minimize the number of singularities to minimize the effect of skew on the grid. The topology depicted in Figure 46 had only one singularity at the nose and the body was comprised of two long rectangles. This topology achieved the minimum orthogonality and maximum stretching numbers closest to one in comparison to future topologies; however, these are only secondary metrics for an acceptable grid. The primary metric of an acceptable grid

was sufficient instability resolution.

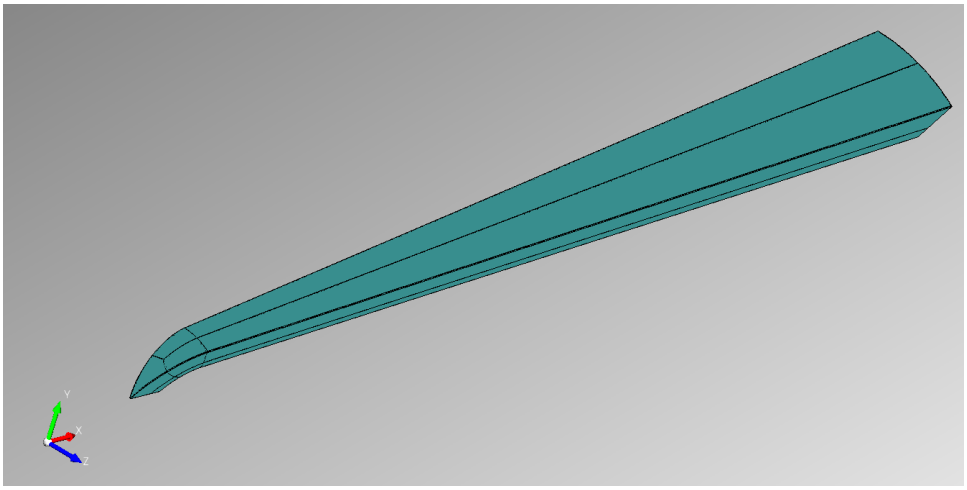

Figure 46. Topology with Nose Singularity

Using the 12.7 mm nose radius case in the coarse grid as an example case, the grid on the nose of the cone was able to support instabilities with frequencies of 400 kHz over about 5.5 cells. For a coarse grid, which defined sufficient instability resolution as 2-3 cells, this result of 5.5 cells indicated sufficient instability resolution in the streamwise direction. Therefore, this nose topology was deemed acceptable and was applied to all future design iterations of the topology and for all geometries. As the refinement of the entire grid density increased, the number of cells a 400 kHz instability would occupy on the nose increased as well. For example, in the fine level of grid refinement for the 12.7 mm case the nose grid was able to support an instability of 400 kHz over 10.2 cells.

The example case of a nose radius of 12.7 mm on the coarse grid of 62 million cells was chosen to illustrate the following concepts of the topology design iterations guided by the instability resolution case study. On the body of the cone with a 12.7 mm nose radius in the coarse grid example case, an instability of 400 kHz was supported for 4.3 grid cells in the front third of the cone body and less than one grid cell in the last third of the cone body. Functionally, a frequency of 400 kHz would not be reliably

detected on the last third of the body and therefore the topology shown in Figure 46 was unacceptable because the instability spatial resolution did not reach the 2-3 cell requirement for the entire body of the cone for a coarse grid.

To fix the unreliable instability detection issue on the cone body there are two available courses of action. The first option would be to increase the total cell density by scaling the grid indiscriminately by a factor. This solution would exceed the computational resources allocated for this research effort and this solution would not be optimized because the number of cells on the front third of the cone body would be the same as the number of cells on the back third of the body despite the change in surface area. For consistent instability spatial resolution throughout the entire cone body the number of cells must scale proportionally with the surface area. Otherwise, the front third would have a higher instability spatial resolution than the back third which would result in inconsistent spatial resolution of an instability along the cone body in the streamwise direction. The second and preferable course of action was refinement of the topology to dictate where the already existing density should reside in order to achieve the proper instability spatial resolution for the maximum collected frequencies. In the end, this method decreased the instability spatial resolution of 4.3 cells at the front of the cone to the goal of 2-3 cells and increased the back of the cone's spatial resolution to 2-3 cells.

The topology shown in Figure 47 shows two diamond refinements on the topology of the frustum. The advantage of this topology design was that each streamwise topology line over the frustum could scale to distributed the cells proportional to the surface area increase to achieve proper and consistent instability spatial resolution in the streamwise direction along the entire frustum while maintaining a constant grid density of 62 million cells for the coarse cases. For example, in Figure 46 the single topology line on the frustum in the streamwise direction was divided into 1,000 line

segments of equal spacing regardless of surface area. Therefore the cells in the front of the frustum were tiny while the cells in the back of the frustum in the back were comparably larger. On the other hand in Figure 47, there are three topology lines on the frustum in the streamwise direction and each of the streamwise lines can be divided into a number of segments that corresponds to the surface area. Specifically, the front streamwise topology line was divided into 100 segments, the middle streamwise topology line was divided into 350 segments, and the back streamwise topology line was divided into 550 segments. All three streamwise topology lines added to the same number of divisions as the singular streamwise topology line in Figure 46 resulting in the same cell density in both cases but the density of the cells was shifted towards the back in Figure 47.

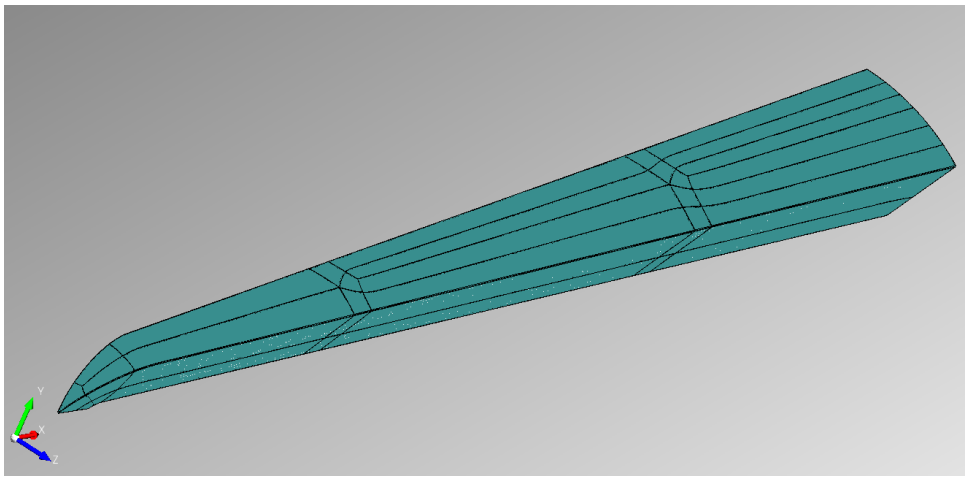

Figure 47. Topology with Nose Singularity and 2 Body Refinements

In a similar manner, the singularity topology shown in Figure 47 aided with instability resolution in the azimuthal direction. The singularities added the opportunity to adjust the instability resolution in the azimuthal direction proportional to the surface area. The same instability resolution acceptability criteria was applied to the azimuthal direction and the results are available in Table 1 for the final topology. Additionally, the addition of cells in the azimuthal direction as surface area increased

aided with the maintenance of the cell isotropy. The cells created in the direction normal to the surface were based on the non-dimensional wall unit calculations and are discussed in Section 2.3.

For the 12.7 mm nose radius case for a coarse grid resulted in the first third of the cone supported an instability of 400 kHz for 2.4 cells and the back third of the cone supported an instability of 400 kHz for 1.8 cells. The goal for the coarse grid was to achieve instability spatial resolution of 2-3 cells therefore this topology still fell short of acceptable on the back third of the frustum.

One more iteration of topology refinement on the frustum was designed in effort to increase detection of instabilities to consistent and acceptable levels. The final topology added three more diamond refinements (five total) over the body and is shown in Figure 48. The final topology generated 11 total singularities with each diamond refinement having introduced a pair of singularities and one singularity contributed from the nose topology. Each singularity added skew and moved the minimum orthogonality and maximum stretching away from one. However, the effect of the singularities was assessed to be minimal. For example, the 12.7 mm nose radius case on the coarse grid has a minimum orthogonality was 4% from the unity value, and a maximum stretching was less than 1% from the unity value. Additionally, the minimum orthogonality and maximum stretching tended closer to one as the grid density increased from the coarse level to the fine level for both nose radii cases. Therefore, the number of singularities was assessed to be acceptable for this research application. The topology in Figure 48 supported an instability of 400 kHz for 5.5 cells over the nose, 2.4 cells on the first third of the body and 2.3 cells on the last third of the body. This was sufficient for the coarse grid because it met the detection requirement of 2-3 cells and the additional requirement of consistent detection along the entire body.

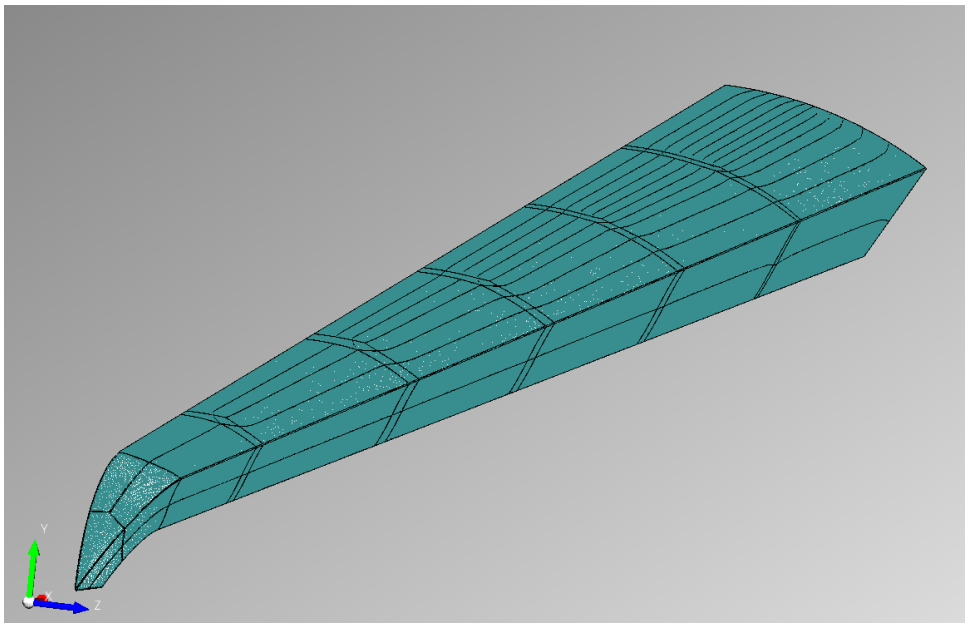

Figure 48. Topology with Nose Singularity and 5 Body Refinements

Although the 12.7 mm nose radius geometry with a coarse grid was used as an example, this instability resolution case study was completed for all the geometries with varying nose radii and at all refinement levels. A summary of the grid and the corresponding number of cells an instability of appropriate frequency would occupy on the nose, on the first third of the body, and the last third of the body in both the streamwise and azimuthal directions is provided in Table 1. Table 1 demonstrated that for the coarse grid the instability spatial resolution in the streamwise direction (x) was maintained at 2-3 cells and for the fine grid the instability spatial resolution was maintained at 8-10 cells. The instability resolution in the azimuthal direction (z) surpassed the necessary instability resolution requirements.

Table 2. Instability Resolution Case Study Results

R_N	Refinement	Cells on Nose	Cells on Front Body	Cells on Back Body
9.5	Coarse (x)	5.5	3.6	3.2
9.5	Coarse (z)	17.3	14.7	8.9
9.5	Fine (x)	10.2	9.4	8.2
9.5	Fine (z)	29.1	21.3	15.4
12.7	Coarse (x)	5.5	2.4	2.3
12.7	Coarse (z)	17.3	12.6	7.1
12.7	Fine (x)	10.2	8.1	8.0
12.7	Fine (z)	29.1	20.9	14.7

2.2 Boundary Conditions.

The required proper usage of the available boundary conditions not only allowed for accurate simulation of the flowfield, but was needed to reduced computational requirements. To enforce all of the boundary conditions used to model the 7° half-angle cone, a layer of cells called the ghost cells was automatically added to the grid within the US3D flowsolver for the primary purpose of modeling the physics of each type of boundary condition. Figure 45 shows which boundary conditions were applied to the geometry features of the model. A brief explanation of each type of boundary condition and the behavior of the ghost nodes follows in the subsequent sections.

2.2.1 Solid Wall Boundary Condition.

The solid wall boundary condition imposed the presence of the geometry under the solution domain. Figure 45 shows that the solid wall boundary condition was applied to the cone surface. The solid wall boundary condition applied to the cone surface was physically enforced by not permitting mass to pass through that boundary of

the computational domain. Additionally, the solid wall boundary condition applied a no-slip boundary condition to the viscous velocity at the wall. The no-slip boundary condition dictated that all the fluid velocity was tangential to the wall and no fluid was flowing into the wall. These characteristics of the solid wall boundary condition are mathematically expressed by

$$\vec{u}_{wall} = 0 \tag{3.9}$$

where $\vec{u}_{wall}$ is the component of velocity normal to the solid cone surface. In physical terms, the solid wall boundary condition allowed the fluid to move parallel to wall but not into or out of the solid wall. This boundary condition does not interfere with quantities that transfer to or from the surface such as heat flux. For hypersonic flight conditions for which the high altitude dictates rarefied conditions, a slip-wall boundary conditions is applied to the surface of the model [47]. However, the AEDC Tunnel 9 test conditions which this research effort endeavors to simulate do not constitute rarefied conditions.

This research effort additionally enforced the Dirichlet wall boundary condition of an isothermal wall. The cone wall was held at a constant temperature of 298 K. This isothermal wall boundary condition was considered an accurate representation of the experiments conducted by Moraru because the AEDC Tunnel 9 has a maximum test time of 15 seconds which would not allow for significant wall temperature change [56].

2.2.2 Supersonic Inflow and Outflow Boundary Conditions.

The supersonic inflow boundary condition was applied to the shock cone which encompassed the 7° half angle cone in Figure 45. The inflow shock surface represented the top of the computational domain and the implied assumption was that all of the relevant flow physics would occur below that threshold. The supersonic outflow boundary condition was applied to the plane in the x-direction at the back of the

7° half-angle cone in Figure 45. Since the wake of the flowfield was not the area of interest for this research effort, the outflow plane was applied flush with the end of the cone. The Euler eigenvalue solutions to the one-dimensional wave provided a crucial understanding of supersonic inflow and outflow boundary conditions. The one-dimensional wave equation is

$$\frac{\partial u}{\partial t} + a\frac{\partial u}{\partial x} = 0 \tag{3.10}$$

where u is the x-direction component of velocity and a is the speed of sound. The eigenvalue solutions of Equation 3.10 are u, $u - a$, and $u + a$. In hypersonic conditions, the value of u is always going to be greater than the value of a therefore the eigenvalue solutions are positive definite and will always move in the positive streamwise direction. In a practical sense for a supersonic inflow boundary condition, all of the eigenvalues of the wave equation were pointed into the domain and the inflow conditions were independent of the interior physics. Therefore, in a supersonic inflow conditions, all flow variables in the ghost cells were set to the freestream values.

For a supersonic outflow conditions, all of the eigenvalue solutions were still pointing in the positive streamwise direction, or out of the domain, since u is always going to be greater than the value of a for hypersonic conditions. Thus, for a supersonic outflow boundary condition, all of the outflow ghost cell values were extrapolated from the respective values of the last interior grid cell. A completely supersonic outflow boundary condition was applied to the back plane of the computational model in Figure 45. However, the solid wall boundary condition enforced a no-slip boundary condition at the wall as described in Section 2.2.1. Therefore the velocity at the cone and for some cells above the wall was subsonic or transonic. The cells with subsonic and transonic velocities created a mismatch between the physics and the boundary condition applied. Referring back to Equation 3.10, in a subsonic outflow boundary

condition, the eigenvalue of $u-a$ would enter back into the domain and the other two eigenvalues of u and $u+a$ would leave the domain. The method in which the boundary conditions were applied in this research neglected the eigenvalue which enters back into the domain for the cells which are subsonic and transonic in the boundary layer.

2.2.3 Symmetry and Periodic Boundary Conditions.

Figure 45 shows the two symmetry planes which created the 30° slice of the 7° half-angle cone. The symmetry plane utilized in the viscous flow was a zero-shear slip wall boundary condition. A symmetry plane required the fluid to not penetrate the surface, i.e. u_n at the surface was equal to zero.

$$u_{t,ghost} = u_{t,interior} \tag{3.11}$$

$$u_{n,ghost} = -u_{n,interior} \tag{3.12}$$

Symmetry planes were useful in reducing the computational domain necessary to glean an understanding of the full research question. The solution could be mirrored over the symmetry plane for a complete picture of the flowfield solution.

Symmetry planes were not the only means to create to a 30°slice. Periodic boundary conditions are also commonly used to simulate a small part of a larger system; like a slice of a cone. A periodic boundary condition takes the solution at the cell centers of the ghost cells at one surface and wraps around the cone to match to the cell centers of the ghost cells of its paired surface. If a periodic boundary condition was applied to this research effort, the planes labeled "Symmetry Planes" in Figure 45 would have become "Periodic Planes". The maximum difference between cell centers of the paired surface ghost cells was 4×10^{-4} m when applied to the 9.53 mm nose radius case on the coarse grid. The maximum difference between cell centers of the paired surface ghost cells improved to 1.4×10^{-6} m when applied to the 9.53 mm

nose radius case on the fine grid refinement level. However, both cases were above the tolerance threshold of 10^{-8} for the flow solver, US3D, and therefore the symmetry boundary condition was applied to the surface to create the 30° slice.

2.3 Boundary Layer.

The boundary layer height is not large therefore, special consideration must be taken when modeling the computational domain in the boundary layer region. Specifically, first cell should have a nondimensional wall distance unit (y^+) of about 1. The equation for the nondimensional wall distance unit was given in Equation 2.5. The nondimensional wall distance unit was based an initial spacing calculated from the flowfield conditions of the flow described in Section 1.1. The first step in estimating the proper initial spacing was to calculate the coefficient of friction (C_f) via Prandtl's one-seventh power law for a flat plate[64].

$$C_f = \frac{0.026}{Re^{\frac{1}{7}}} \tag{3.13}$$

Although Equation 3.13 was designed for the flat plate application, it provides an adequate estimation for the estimation of the coefficient of friction and is embedded in commercial gridding software such as Pointwise. From the coefficient of friction, the skin shear stress on the wall (τ_{wall}) was estimated from the following relationship

$$\tau_{wall} = \frac{C_f \rho_\infty V_\infty^2}{2} \tag{3.14}$$

where ρ_∞ and V_∞ were freestream values of density and velocity respectively. Next, the friction velocity (v^*) was estimated from the skin shear stress value and the

freestream density using Equation 2.40. The initial spacing (Δs) was estimated via

$$\Delta s = \frac{y^+ \mu}{v^* \rho} \tag{3.15}$$

where μ was the kinematic viscosity calculated in Section 1.1 and y^+ was the desired nondimensional wall distance unit. The current research effort used a nondimensional wall distance unit of 0.95 and the initial spacing was 2.7×10^{-5} m. Figure 49 shows that the resultant nondimensional wall distance unit for the 7° cone. Notably, the nondimensional wall distance unit reached a maximum of 0.95 along the nose and maintained much smaller nondimensional wall distance unit along the frustum of the cone. The nondimensional wall distance unit contour plot shown in Figure 49 was the exact values for the smooth wall solution. For the simulations run with the distributed surface roughness, a grid tailoring function of US3D was utilized which redistributed cells in the direction normal to the surface of the cone. However, a nondimensional wall distance unit rule was implemented which did not permit a nondimensional wall distance unit greater than 0.95. The nondimensional wall distance unit rule preserved the integrity of the boundary layer modeling. More information on the grid tailoring functionality and how it was used in this research effort is available in Chapter 4 Section 2.

Since the boundary layer contained the physical phenomena which this research effort endeavored to simulate, placement of an adequate number of cells in the boundary layer region became an additional modeling consideration. LINK3D$^{\text{TM}}$, the gridding software tool, provides a cluster group grid tool which aids in modeling boundary layers appropriately. For this research effort, a cluster group was made for the entire surface of the cone by utilizing the previously calculated initial spacing of 2.7×10^{-5} m, the desired 251 cells normal to the cone, and the desired growth rate of 5%. In other words, the first cell over the entire body of the cone would have a height of

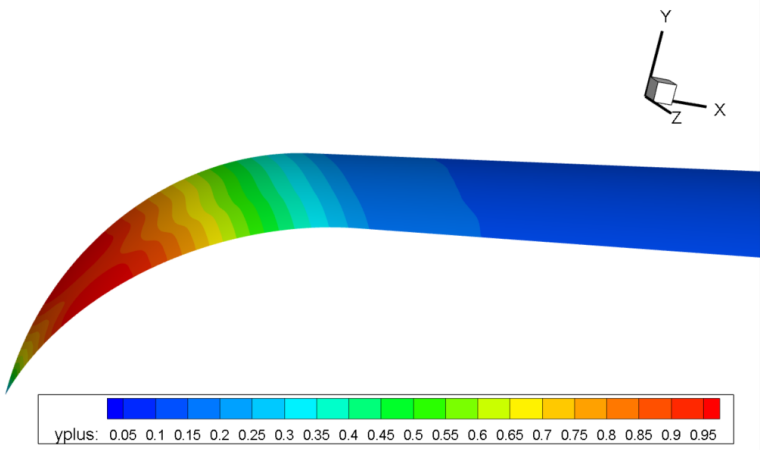

Figure 49. y^+ **Contour**

2.7×10^{-5} m. Then, that height would grow by 5% for the next cell and so forth for 251 cells. The collection of 251 cells would create a region where the boundary layer could be reasonably calculated with high cell density for appropriate physical phenomena modeling. Figure 50 is oriented along the body of the cone with the symmetry planes on either side of the 30° cone slice modeled in black grid pattern. The blue grid sheets in Figure 50 are grid sheets in the streamwise and spanwise direction of the cone body for the purpose of aiding visualization of the boundary layer. The boundary layer is seen in Figure 50 as a thin dark blue region where the surface of the cone was modeled. The boundary layer has a higher density than the rest of the computational domain therefore it shows up in Figure 50 as much darker.

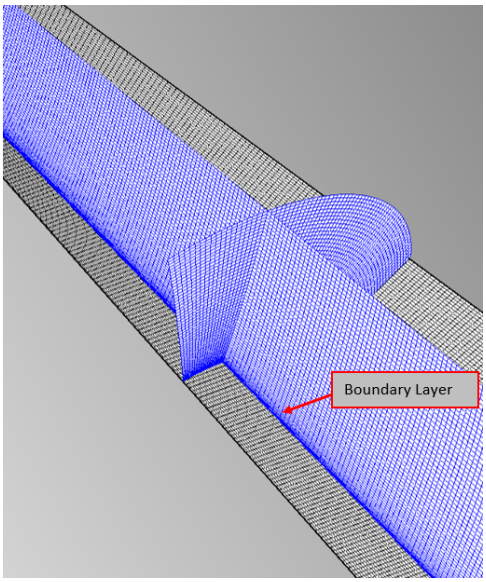

Figure 50. Boundary Layer Clustering on Cone

3 Flow Solver: US3D

The University of Minnesota developed US3D flow solver was chosen for this research effort because of its well established applicability to hypersonic research discussed in [9] and proven in notable works such as [85]. US3D was built on the foundation of the Data Parallel Line Relaxation (DPLR) method described in Reference [91]. The credibility of the US3D results obtained rests on the laurels of the numerous recent research efforts which have leveraged US3D as the flow solver including the research of Dinzl and Candler from the University of Minnesota [21], Edelman and Schneider from Purdue University [23], and Marineau et al. from AEDC [54].

3.1 The Governing Equations.

The Navier-Stokes equations in conservative law form, or integral formulation, are

$$\frac{\partial}{\partial t}\int_{\Omega}\rho d\Omega + \oint_{\partial\Omega}\rho(\vec{v}\cdot\vec{n})dS = 0 \tag{3.16}$$

$$\frac{\partial}{\partial t}\int_{\Omega}\rho\vec{v}d\Omega+\oint_{\partial\Omega}\rho\vec{v}(\vec{v}\cdot\vec{n})dS=\int_{\Omega}\rho\vec{f_e}d\Omega-\oint_{\partial\Omega}p\vec{n}dS+\oint_{\partial\Omega}(\overline{\overline{\tau}}\cdot\vec{n})dS \tag{3.17}$$

$$\frac{\partial}{\partial t}\int_{\Omega}\rho Ed\Omega+\oint_{\partial\Omega}\rho H(\vec{v}\cdot\vec{n})dS=\oint_{\partial\Omega}k(\nabla T\cdot\vec{n})dS+\int_{\Omega}(\rho\vec{f_e}\cdot\vec{v}+\dot{q_h})d\Omega+\oint_{\partial\Omega}(\overline{\overline{\tau}}\cdot\vec{v})\cdot\vec{n}dS \tag{3.18}$$

where ρ is density, Ω is the finite volume, $\vec{v}$ is the velocity vector, $\vec{n}$ is the normal vector, dS is the elemental surface area, $\vec{f_e}$ are any external forces, $\overline{\overline{\tau}}$ is the viscous stress tensor, E is the total energy per unit mass, H is the total enthalpy, k is the thermal conductivity coefficient, T is the absolute static temperature, and $\dot{q_h}$ is the time rate of change of heat transfer per unit mass. Equation 3.16 represents the conservation of mass or the Continuity Equation, Equation 3.17 represents the conservation of momentum, and Equation 3.18 represents the conservation of energy.

US3D solves the Navier-Stokes Equations, Equations 3.16 - 3.18, via finite volume formulation [36]. The finite volume formulation of the Navier-Stokes equations hinges on the definition of flow variables occurring at the centroids instead of the x,y,z location of the intersections of the mesh lines [47]. Thus the control volumes are the same as the grid cells [7]. For accurate calculations, regardless of the dimension of the cell, the cell centered gradients are computed using a weighted-least-squares reconstruction of the primitive variables while viscous fluxes are computed using a deferred-correction approach [36].

3.2 Smooth Wall Computations.

The US3D code has many options for spatial and temporal calculations; all of which are available in Reference [36]. For the smooth wall computation of this re-

search effort, the viscous fluxes were computed as second order and the calculation of the convective fluxes for the steady state simulation were completed using the Modified Steger-Warming (MSW) scheme consistent with Reference [10]. When strong shocks were present, as often the case in hypersonic applications, a second order Monotonic Upwind Scheme for Conservation Laws (MUSCL) scheme in accordance with Reference [44] was utilized.

For the steady state calculations for this research effort the Data Parallel Line Relaxation (DPLR) time integration method consistent with the development in Reference [91] was used when possible and if it were not possible the US3D defaulted to the point relaxation method. The DPLR scheme was able to obtain a steady state solution by solving along lines of cells normal to the wall. Due to the nature of implicit methods, a great deal of communication between processors was required to invert large matrices [91]. Historically, this prohibited the full power of implicit time integration methods from being realized on supercomputers. However, the data parallelization of the DPLR scheme implemented within US3D allowed for implicit methods to realize the efficiencies of supercomputers and made this method of time integration ideal for the smooth wall solutions obtained in this research effort.

As stated in Section 2.2.1, the wall of the 7° half-angle cone was assumed isothermal with a wall temperature (T_w) of 298 K. The tunnel conditions were taken from Entry 3747 of Moraru's thesis available in Reference [59] and stated in Section 1.1. The AEDC Tunnel 9 is a nitrogen blow down facility. Thus the mass fraction was 100% nitrogen. The smooth wall computations were assumed laminar therefore no turbulence model was implemented. The baseflow computations were viscous simulations and the gradients were computed using the chain rule via cell centered metrics within the hexahedral cells that comprised the structured grids.

3.2.1 Baseflow Computational Results and Analysis.

A converged solution was defined as one that reached a steady state solution. Further iterations would not assist in producing a lower residual. An acceptable converged solution reached a steady state solution with residual error on the order of 10^{-6} or less. All baseflow solutions met the acceptable converged solution criteria for the operating conditions defined in Section 1.1. Further proof of time independence is available in Section 3.4.

Figures 51, 53, and 55 are full body contours of the flow solution around the 30° slice of the cones with nose radii of 9.53 and 12.7 mm. Figures 52, 54, and 56 are countour solutions of the flow in the nose region of the 30° slice of the cones with the nose radii of 9.53 and 12.7 mm. These smooth wall solutions are provided for the purpose of verification and visualization of the relevant hypersonic aerodynamics and to later compare and contrast with the rough calculations. In Figure 53, the no-slip boundary condition on the surface of the cone was properly employed because the surface of both of the cones showed a Mach number of zero at the surface. The Mach number quickly increased to the freestream conditions in accordance with the thin boundary layers typical of high Reynolds number flow. An isothermal surface temperature was employed for the simulations due to the small test time. In Figure 51, the isothermal surface of 298 K was evident by the temperature gradient which formed from the surface to the colder freestream air temperature. The highest temperatures were located on the nose of the cone as expected.

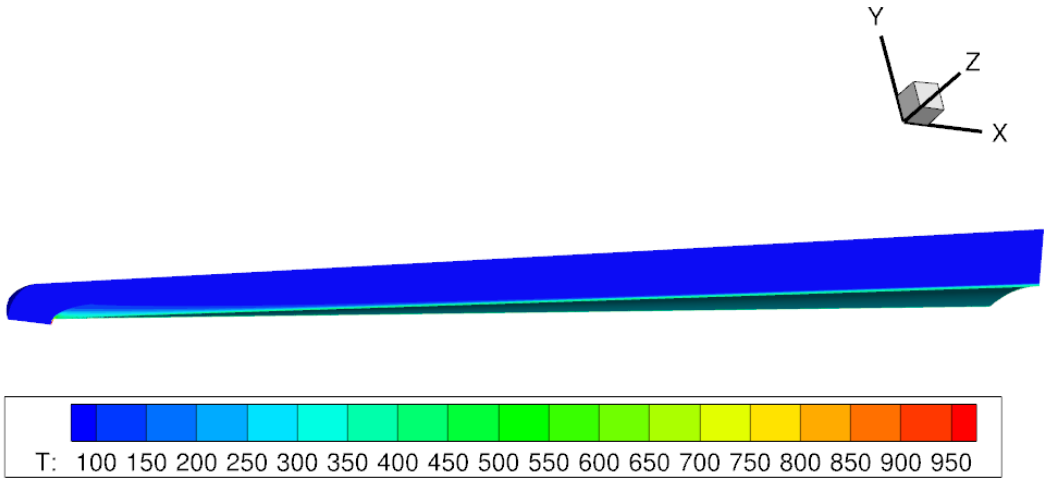

(a) R_N **= 9.53 mm**

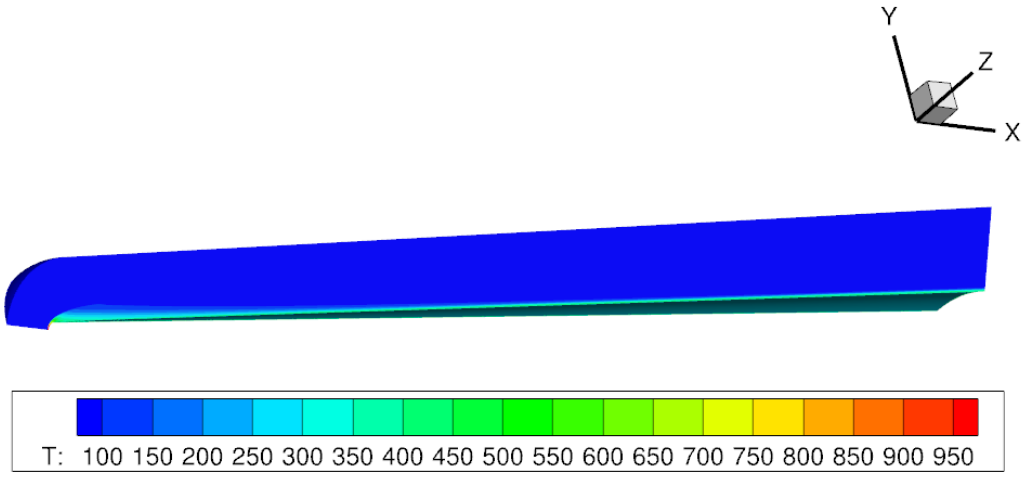

(b) R_N **= 12.7 mm**

Figure 51. Temperature Contour Solution of Laminar Flow at unit Reynolds number of 16.9×10^6 **/m on Fine Grid Refinement**

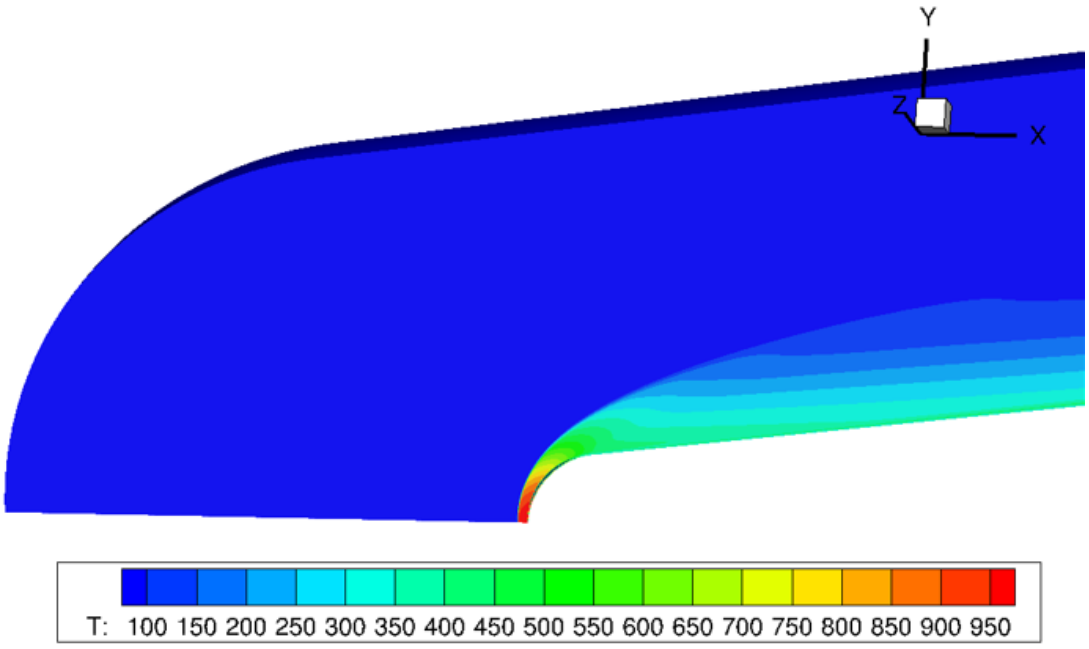

(a) R_N **= 9.53 mm**

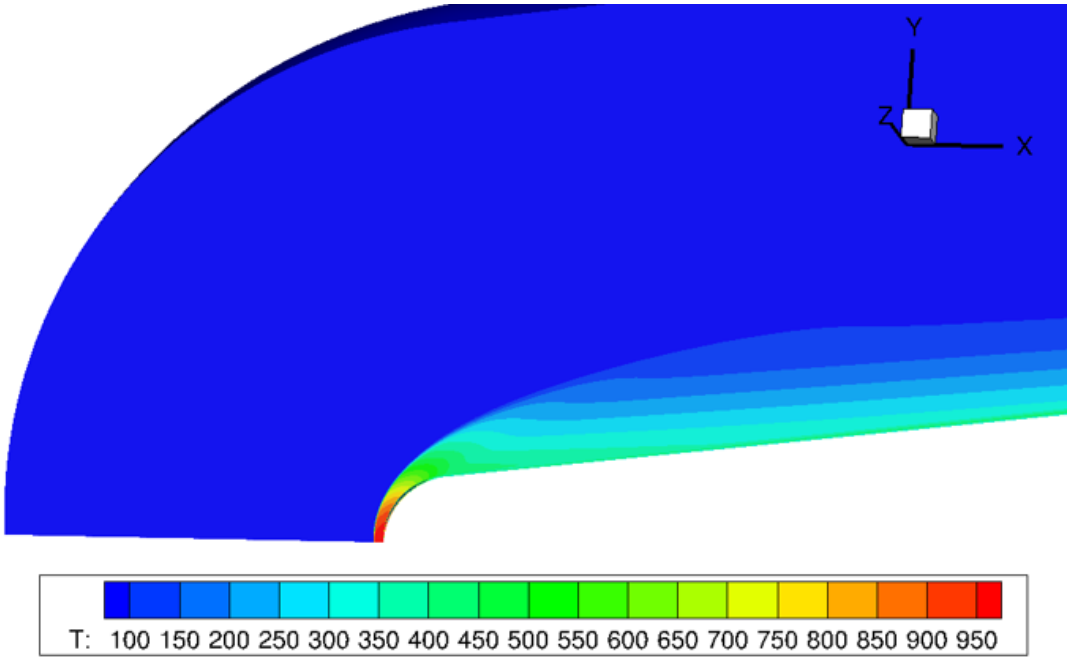

(b) R_N **= 12.7 mm**

Figure 52. Temperature Contour Solution on Nose Region of Cones of Laminar Flow at unit Reynolds number of 16.9×10^6 **/m on Fine Grid Refinement**

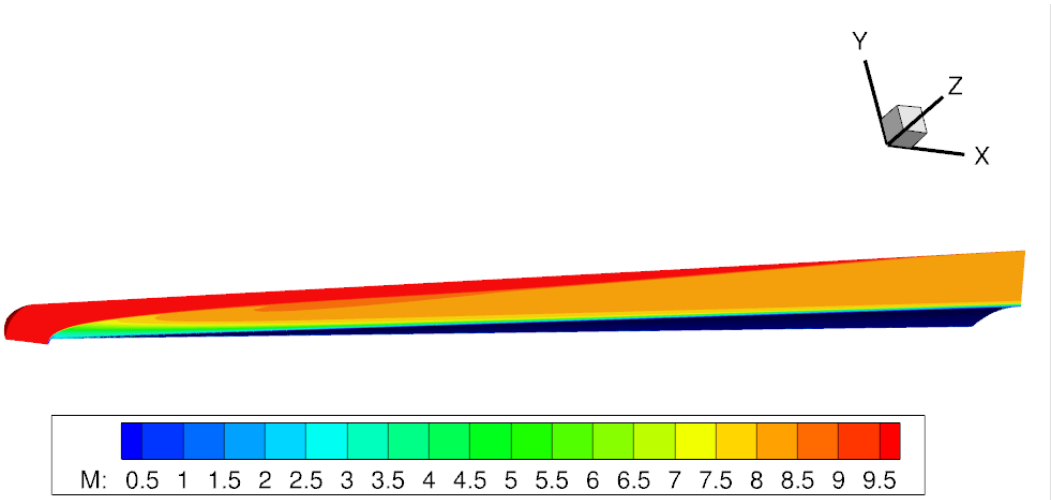

(a) R_N **= 9.53 mm**

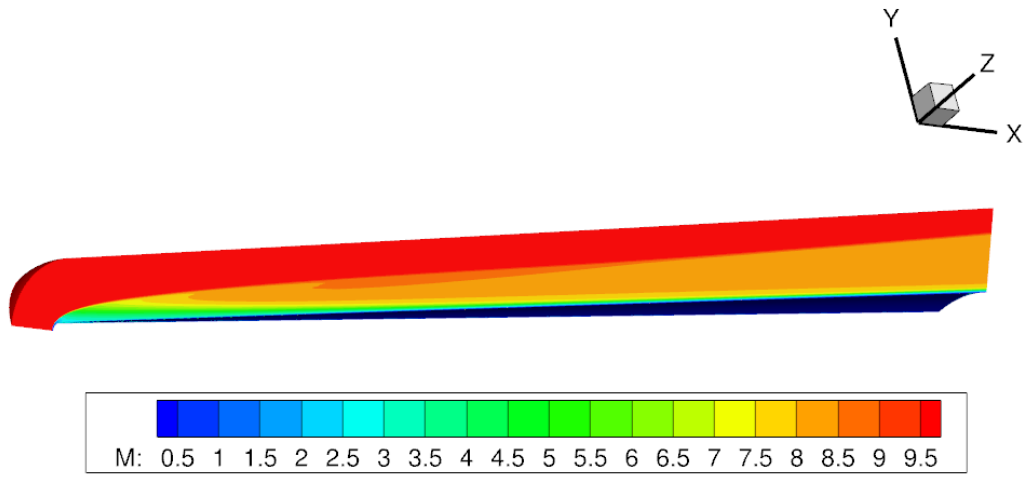

(b) R_N **= 12.7 mm**

Figure 53. Mach Contour Solution of Laminar Flow at unit Reynolds number of 16.9×10^6 **/m on Fine Grid Refinement**

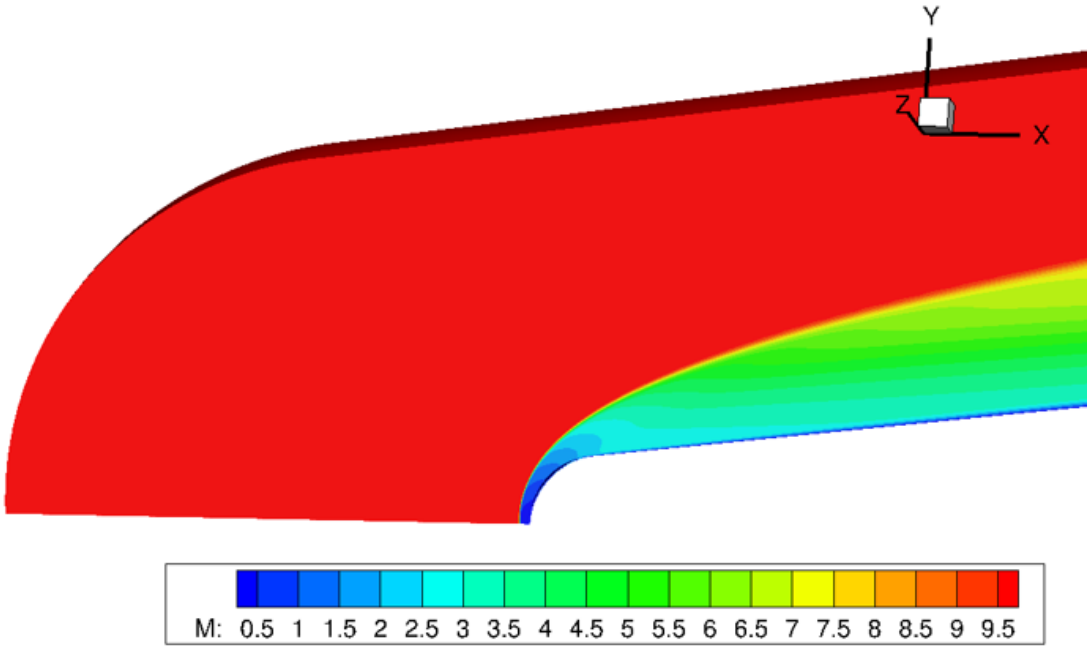

(a) R_N **= 9.53 mm**

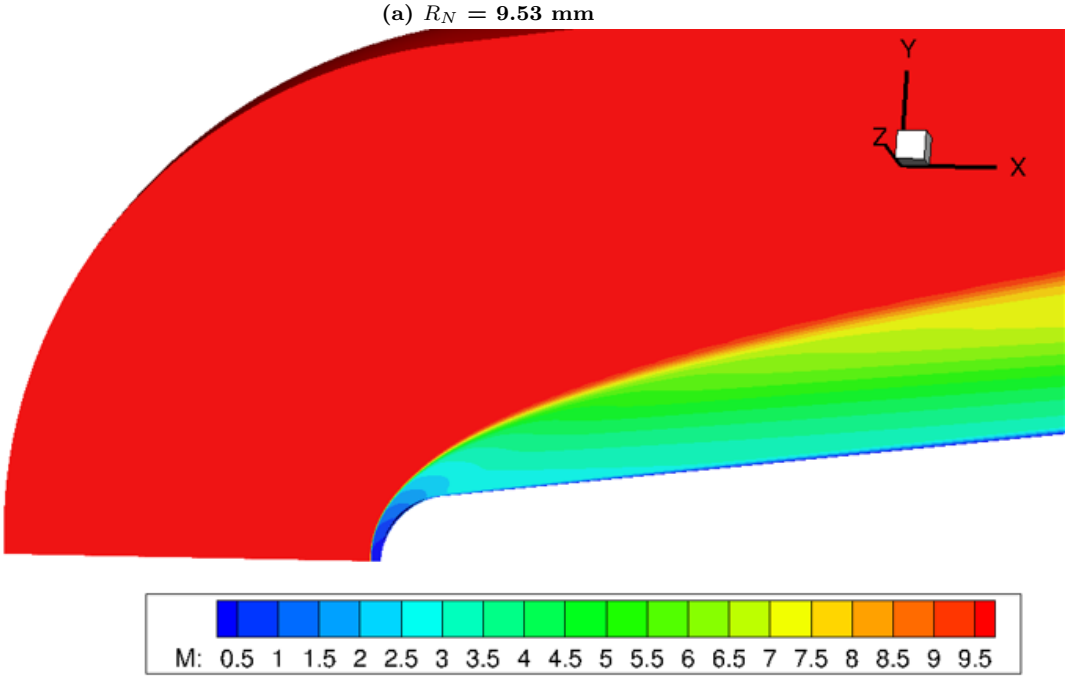

(b) R_N **= 12.7 mm**

Figure 54. Mach Contour Solution on Nose Region of Cone of Laminar Flow at unit Reynolds number of 16.9×10^6 **/m on Fine Grid Refinement**

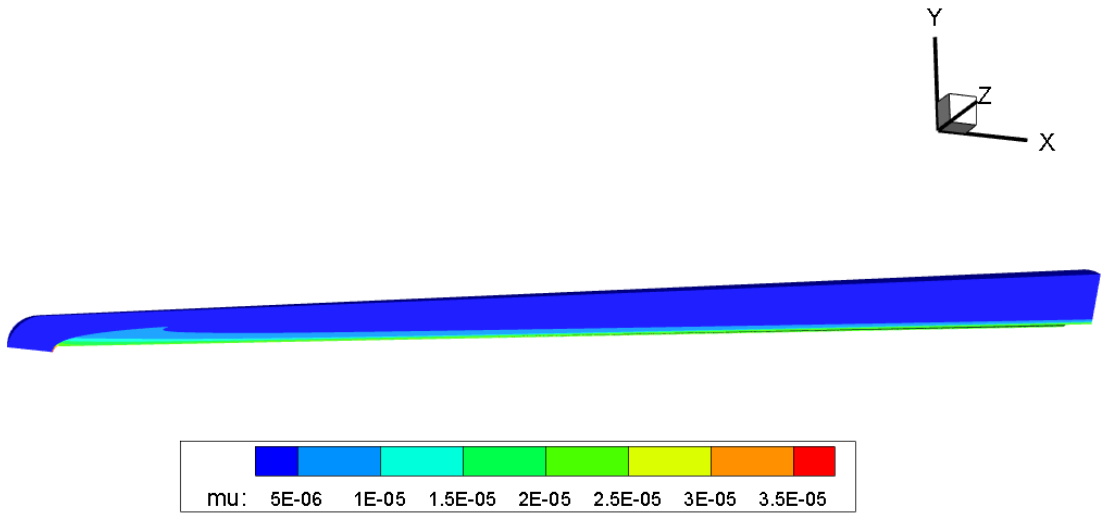

(a) R_N **= 9.53 mm**

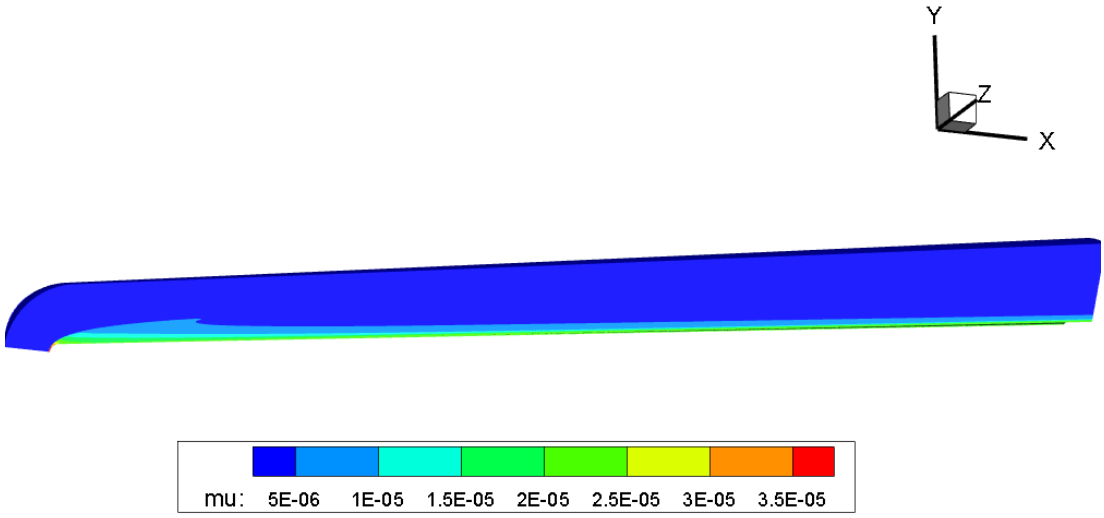

(b) R_N **= 12.7 mm**

Figure 55. Viscosity Contour Solution of Smooth Body Flow at unit Reynolds number of 16.9×10^6 **/m on Fine Grid Refinement**

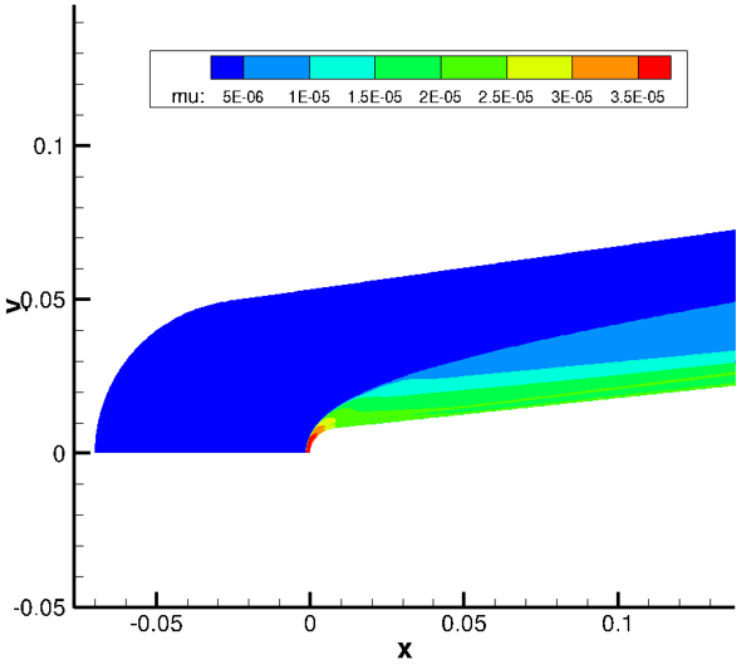

(a) R_N **= 9.53 mm**

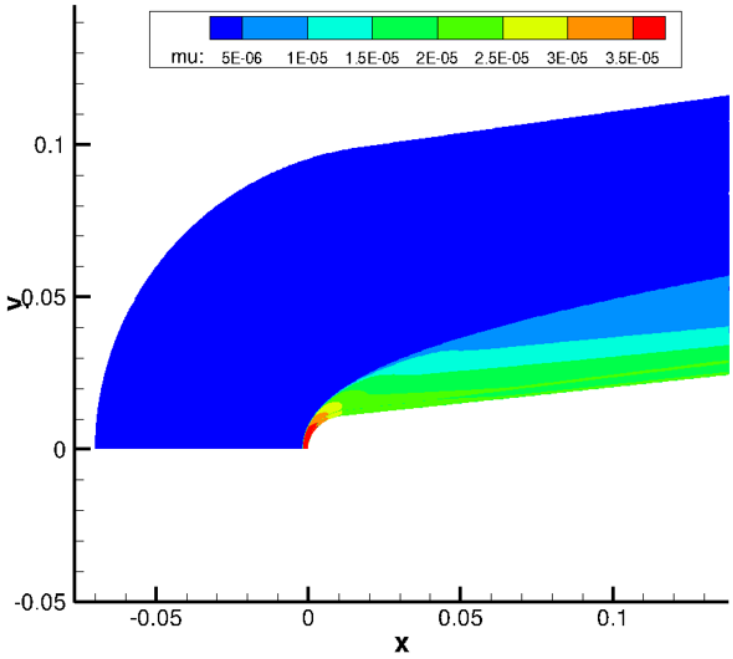

(b) R_N **= 12.7 mm**

Figure 56. Viscosity Contour Solution on Nose Region of Cone of Smooth Body Flow at unit Reynolds number of 16.9×10^6 **/m on Fine Grid Refinement**

In Chapter 2 Section 6, the various methods of transition prediction were discussed, and the amassed knowledge resulted in the conclusion that there was no adequate method of transition prediction for blunt nose geometries. Thus, it was decided to pursue a DNS for this research effort. Further support of this decision is provided in Figure 57. Linear Stability Theory invokes the parallel flow assumption which states that all flow occurs parallel to the surface of the cone and no flow occurs perpendicular to the surface of the cone. The parallel flow assumption has proven highly accurate for sharp nose cones. However, Figure 57 proves that a significant amount of flow occurs in the direction perpendicular to the surface of the cone with blunt nose cone geometries. Therefore, modeling the blunt geometries with any other transition prediction methodology besides a DNS would neglect the vertical flow component shown in Figure 57.

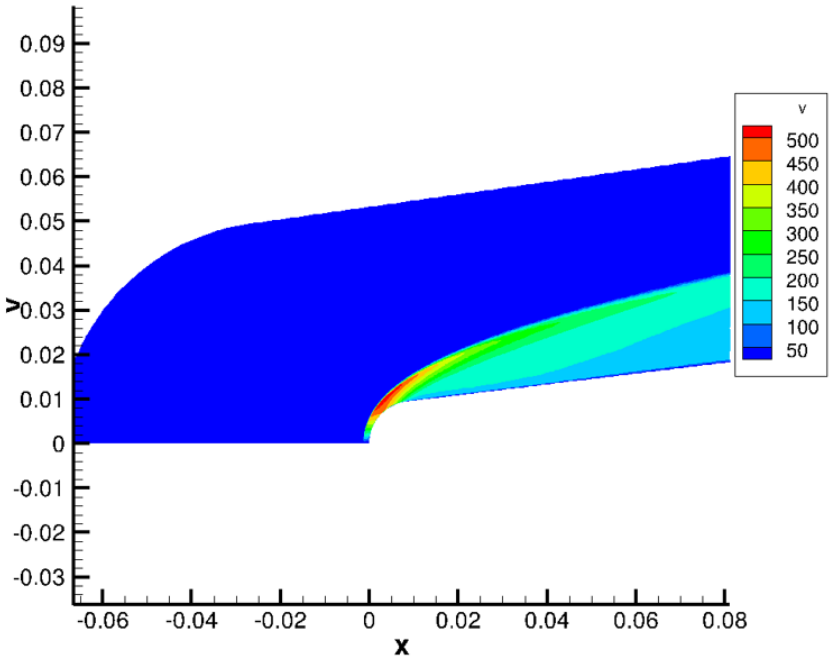

Figure 57. Y-Component of Velocity

Transition was inferred by a sustained increase in heat transfer above the smooth wall calculations. In Figure 58 the total wall heat flux (q_w) was computed from the smooth wall case and is provided in units of W/m^2 for the 9.53 mm and 12.7 mm nose radii cases. A positive magnitude of q_w indicated that heat was being transferred to the cone. As expected, the peak values of the heat flux occurred in the nose regions of the cone and then remained at a lower constant value over the body.

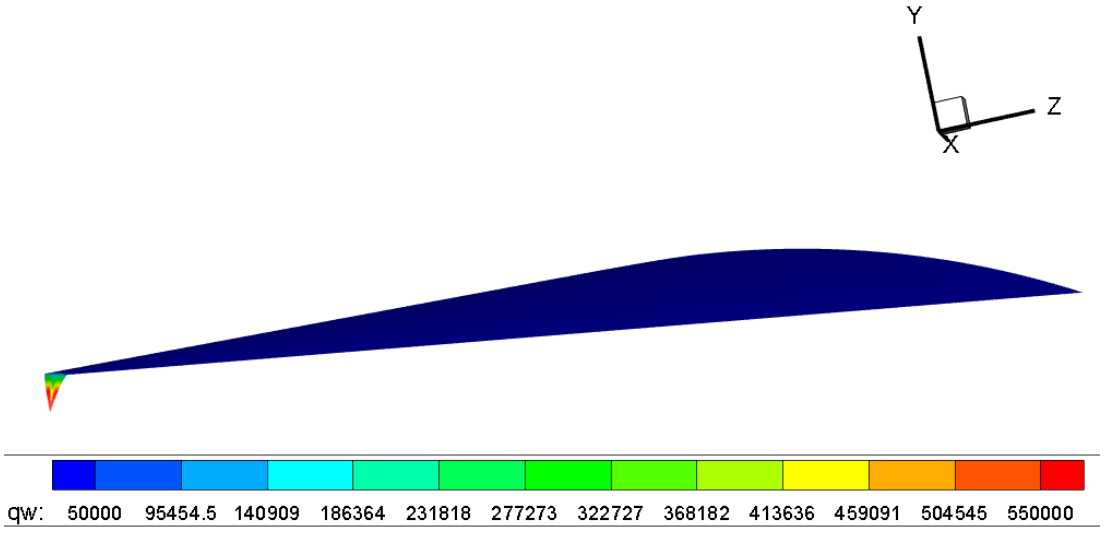

(a) R_N = 9.53 mm

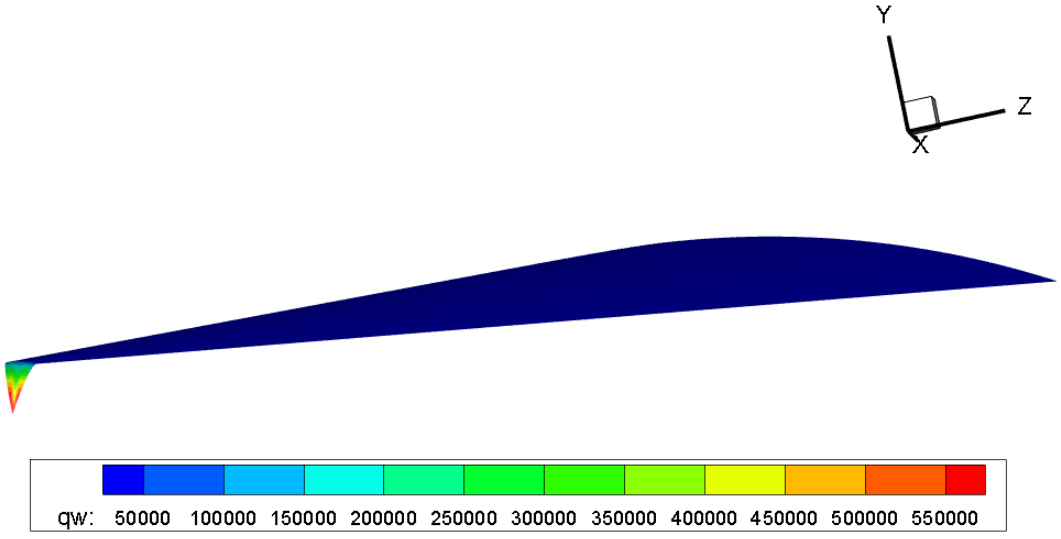

(b) R_N = 12.7 mm

Figure 58. Heat Flux Surface Contour Solution of Laminar Flow at unit Reynolds number of 16.9×10^6 /m on Fine Grid Refinement

The effects of the cells skew on the nose caused by the singularity on the nose topology and the non-parallel lines forming the 30° slice of the geometry cause error in the solution at the nose. In Figure 59 the heat flux was calculated for the cone with the nose radius of 12.7 mm and the pattern of the heat flux proved that error from the skewed cells existed in the solution. The heat flux was the highest at the stagnation point and decreased as the streamlines encountered an increasingly oblique shock. In a smooth wall case this would happen in a horizontal gradation. Figure 59 shows that the heat flux decreased as the streamlines encountered an increasingly oblique shock in a manner that resembled a horizontal gradation pattern but was distorted down the centerline by error due to cell skew.

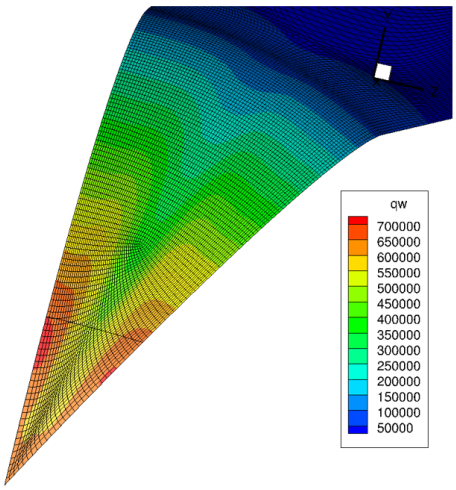

Figure 59. Effects of Nose Cell Skew on Laminar Solution

In Moraru's thesis, laminar CFD simulations were reported and are provided in Figure 60a [59]. These laminar lines of heat flux were used as the baseline to served as an indication as to when the experimental heat flux had a sustained increase above the laminar flow thus implicating transition flow. By obtaining the data which belonged to the nose radii cases of 9.53 mm and 12.7 mm from Figure 60a, a direct comparison with extracted heat flux streamtraces from smooth wall computations of

the present research was made in Figure 60b. Figure 60b provided confidence that the smooth body solution completed in the present research effort was similar to the reference calculations from the AEDC Tunnel 9 experiments. The results of Figure 60b validate the flow operating flow conditions which were backed out of the total temperature, total pressure, and Mach number in Section 1.1. The data in Figure 60 was nondimensionalized by the Stanton number (St), calculated via Equation 1.1, and the Reynolds number based on cone length (Re_L).

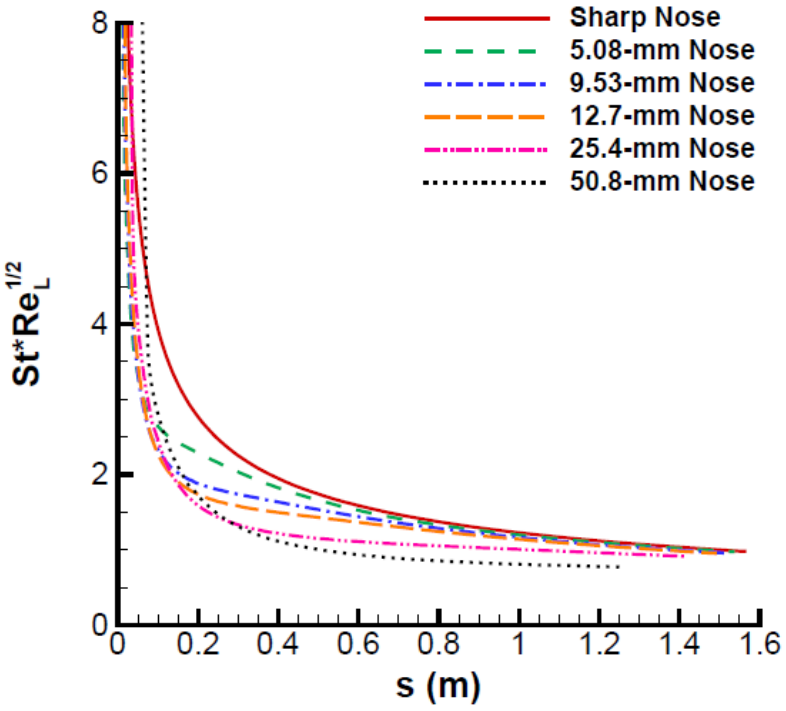

(a) Moraru Laminar CFD Simulation Results (used with permission) [59]

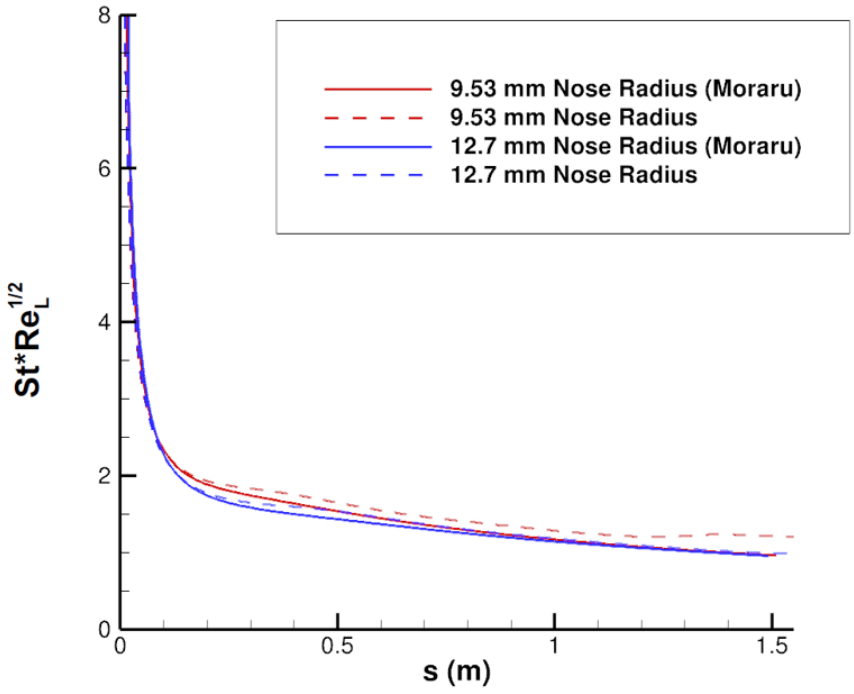

(b) Laminar CFD Simulation Result Comparison: Moraru and Crouch

Figure 60. Smooth Body Simulation Heat Flux Calculations

Figures 61a and 61b are comprised of the heat transfer line calculated by Moraru and the heat transfer line calculated by the present research with details on the grid refinement level. Similarly to the data in Figure 60, the data in Figure 61 was nondimensionalized by the Stanton number (St), calculated via Equation 1.1, and the Reynolds number based on cone length (Re_L). The nose radius case of 9.53 mm when modeled with the coarse grid has the largest deviation from Moraru's laminar solution in Figure 61a. The coarse grid deviated from Moraru's solution by a maximum of 19% near the end of the cone's body and the fine grid deviated from Moraru's solution by a maximum 8% also towards the end of the cone. The discrepancy could have been on account of differences in spatial discretization schemes or differences in viscosity modeling. Recall from Section 1.1 that the simulations for this research effort employed a viscosity model which was built to replicate the pure nitrogen conditions of the AEDC Tunnel 9 facility. The 9.53 mm nose radius case was expected to encounter second mode instabilities which would lead to a sudden spike in heat transfer data as transition occurred; therefore, the discrepancy between smooth wall solutions at the end of the cone was considered acceptable. Additionally, the results for the distributed surface roughness simulations were completed with the fine grids for the 9.53 and 12.7 mm nose radii cases. The discrepancy between the laminar CFD calculations performed by Moraru and the smooth wall calculations solutions performed by the present author was not present in the 12.7 mm nose radius case and much better agreement was demonstrated in Figure 61b. Additionally, Figure 61b provided confidence that the skew on the nose and the distortion of the solution seen in Figure 59 had a minimal impact overall. Therefore the skew in the nose was accepted for the present research efforts.

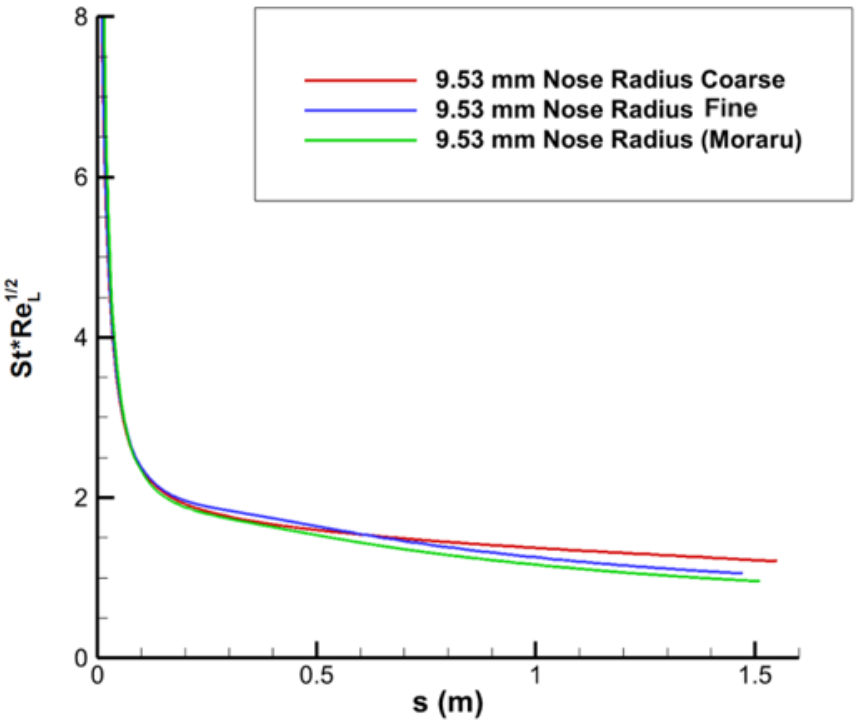

(a) R_N = **9.53 mm Laminar Comparison**

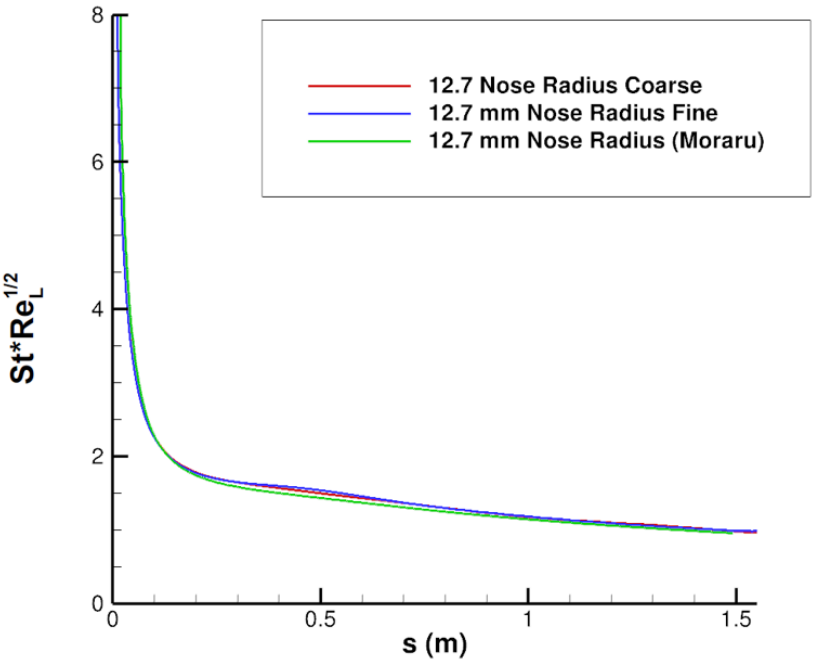

(b) R_N = **12.7 mm Laminar Comparison**

Figure 61. Direct Comparison of Laminar Heat Flux CFD

3.3 Uncertainty due to Discretization.

The experimental uncertainty was presented in Section 1.2; however, quantification of the numerical modeling in the computational efforts performed in this research was necessary to frame the computational analysis. Numerical uncertainty was introduced through the discritization schemes utilized on the Navier Stokes Equations to solve for the solution domain. The Grid Convergence Method (GCI) was used to calculate of the numerical uncertainty. The order of accuracy for the spatial discritization scheme was fourth order Kinetic Energy Consistent (KEC) and the order of accuracy for the temporal discritization was second order Crank-Nicolson. Particular details pertaining to the selection of these spatial and temporal scheme is available in Section 4.

The GCI method is a five step method that was developed based on the widely applied Richardson extrapolation method [13]. The GCI is a measure of the percentage the computed value is away from the value of the asymptotic numerical value [67]. Fundamentally, the GCI method is a form of grid independence used to indicated how further grid refinement would affect the solution. A large GCI would indicate that the solution was highly dependent on the cell size, and further refinement would be recommended.

The GCI method of uncertainty calculation does not account for any modeling errors as it only encompasses the discretization error. The nuanced stipulation in this method of uncertainty reporting lies in the difference between the asymptotic numerical value achieved by the CFD simulations and the true solution value [67]. Since the initial conditions for the CFD simulation were based off of experimental measurements which contain experimental uncertainty, that uncertainty would carry over into these simulations as well. Therefore, there still may be error between the asymptotic value and the true physical solution.

As the GCI process is explained in the remainder of this section, please note that the results of each step for each nose radii geometry is available in Table 3. The first step in the GCI is to calculate a three dimensional representative cell size (C) via

$$C = \left[\frac{1}{N}\sum_{i=1}^{N}(\Delta V_i)\right]^{1/3} \tag{3.19}$$

where N is the total number of cells and V_i is the volume of the ith cell. For the DNS run in this research effort, two levels of refinement were chosen: coarse (60 million cells) and fine (124 million cells). Leveraging US3D's inherent extensibility, a user routine was written to write out the volume of each cell to a file. Due to the requirements of the solved equations, the volume variable within US3D exists solely as the inverse volume. The user routine inverted this variable for a true calculation of the volume. The volume of each cell within the domain is available in Figure 62. In Section 2.1 the concept of cell skew was introduced and in Figure 62 the cell skew is visible in Figure 62 at and around the singularities. These cells at and around the singularities have the largest volume because the cells were stretched larger to fill the non-orthogonal space.

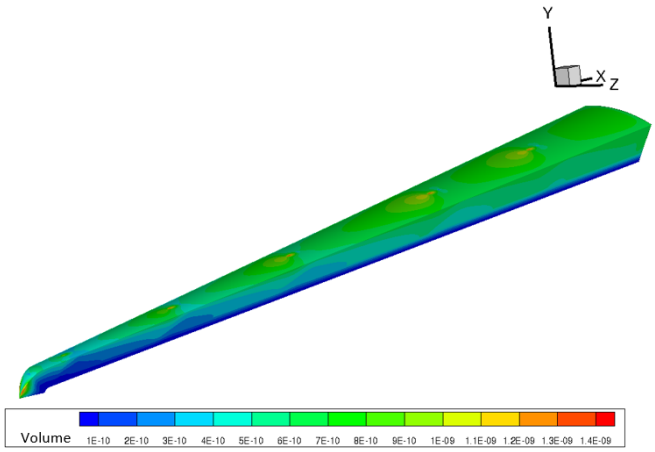

Figure 62. Volume by Cell for R_N = 9.5 mm for the Coarse Grid Refinement

The second step of GCI calls for the calculation of a grid refinement factor (r) to directly compare the representative cell sizes between the three levels of grid refinement.

$$r_{1,2} = \frac{C_{coarse}}{C_{fine}} \tag{3.20}$$

According to Celik et al. an ideal refinement factor has a value of 1.3 and the use of geometrically similarly cells was encouraged [13]. In the case of a structured grid with only hexahedral elements, satisfying the requirement of geometrically similar cells was significantly easier than if an unstructured grid has been created. For all of the grid created for this research effort, the grid refinement factors were around 1.2. To improve the refinement factor to the ideal standard of 1.3, either fewer grid cells would be used in the coarse grids or more grid cells would be used in the fine grids. Since computational considerations negate the option to increase the number of cells in the fine grids, the ideal solution would be to reduce the number of cells used in the coarse grids. However, this action was not taken because reducing the number of cells in the coarse grids would negate the abilities of the grid to reliably detect instabilities according the instability resolution case study performed in Section 2.1. Since the instability resolution was determined to be the more important modeling factor, a refinement factor of 1.2 was determined to be adequate for the endeavored simulations.

The GCI method can be applied to any calculated flow variable which will be generically defined as ϕ. For the calculations in Table 3, Mach number was used as the flow variable and all subsequent error calculations are based on Mach number values. The extrapolated value of the chosen calculated flow variable ($\phi_{ext}^{1,2}$) was calculated in the next GCI step. The calculation of extrapolated values created an error band for the solution. Since the extrapolated values are comprised of the previous two solutions, the error bars lag on refinement level iteration. Thus, the accuracy of the

error bars were considered in Reference [67].

$$\phi_{ext}^{1,2} = \frac{(r_{1,2}\phi_1 - \phi_2)}{r_{1,2} - 1} \tag{3.21}$$

The final step was the calculation of the approximate relative error ($e_a^{1,2}$), the extrapolated relative error ($e_{ext}^{1,2}$), and the fine-grid convergence index (${\text{GCI}_{\text{fine}}}^{1,2}$).

$$e_a^{1,2} = \left| \frac{\phi_1 - \phi_2}{\phi_1} \right| \tag{3.22}$$

$$e_{ext}^{1,2} = \left| \frac{\phi_{ext}^{1,2} - \phi_1}{\phi_{ext}^{1,2}} \right| \tag{3.23}$$

$${\text{GCI}_{\text{fine}}}^{1,2} = \frac{F_s e_a^{1,2}}{r_{1,2} - 1} \tag{3.24}$$

In Equation 3.24, F_s was set to a value of 3.0, the recommended value for only two grids. When comparing three or more grids the Safety Factor would be set to 1.25. From Table 3, all of the GCI values calculated between each refinement level for all nose radii cases were small; therefore further refinement would not improve the solution. Specifically, this indicated that grid independence was achieved between the coarse and fine grid. Transitional CFD protocol often indicates that the smallest grid with grid independence should be used in effort to conserve computational resources. Thus an argument for using solely the coarse grid could be made. However, due to the instability resolution study discussed in Section 2.1, the coarse grid would be insufficient to observe the evolution of the disturbances experienced due to surface roughness. Weighing the results of the instability resolution, the grid convergence study, and the computational resources available, the decision to continue in Chapter 4 with only the fine grids was made.

Table 3. GCI Discretization Error Calculation

GCI Variable	$R_N = 9.5$ mm	$R_N = 12.7$ mm
N_1	65,121,840	60,549,120
N_2	122,370,624	123,177,516
C_1	0.0010	0.0012
C_2	8.38e-04	9.63e-04
$r_{1,2}$	1.19	1.25
ϕ_1	3.493737335	1.16157703334
ϕ_2	3.494115235	1.16389916700
$\phi_{ext}^{1,2}$	3.4918	1.1521
$e_a^{1,2}$	1.08e-04	0.0020
$e_{ext}^{1,2}$	6.68e-04	0.0102
$\mathrm{GCI_{fine}}^{1,2}$	6.99e-04	0.0102

3.4 Time Independence.

A converged solution indicated that no further allotment of time via iterations would change the solution. Determination of a converged solution was made by observing the solution residual which determined the difference between the solution at the current timestep and the previous timestep. When the residual no longer changed or entered into a chattering pattern depending on the dicretization error, then convergence on a solution was determined. To verify this method of convergence monitoring, the solution for the 7° half-angle cone with the nose radius of 12.7 mm on the coarse refinement grid was taken to a solution with a chattering residual on the order of 10^{-6}. At this point the solution for the Mach number was post-processed. Then, the solution was run an additional 10,000 iterations and the solution for the Mach number was post-processed for a second time. Within the plotting software TecPlot$^{\mathrm{TM}}$, both solutions were loaded, and the second Mach number solution was subtracted from the first Mach number solution. The delta between the second and first Mach number solution is shown in Figure 63 and the maximum order of magnitude of change between the two solutions was on the order of magnitude of 10^{-7} which occurred in the areas which occurred on the nose where the cells had the highest amount of skew,

namely the solution near the singularities. Thus the method of residual observation was proven an effective technique for time independence determination.

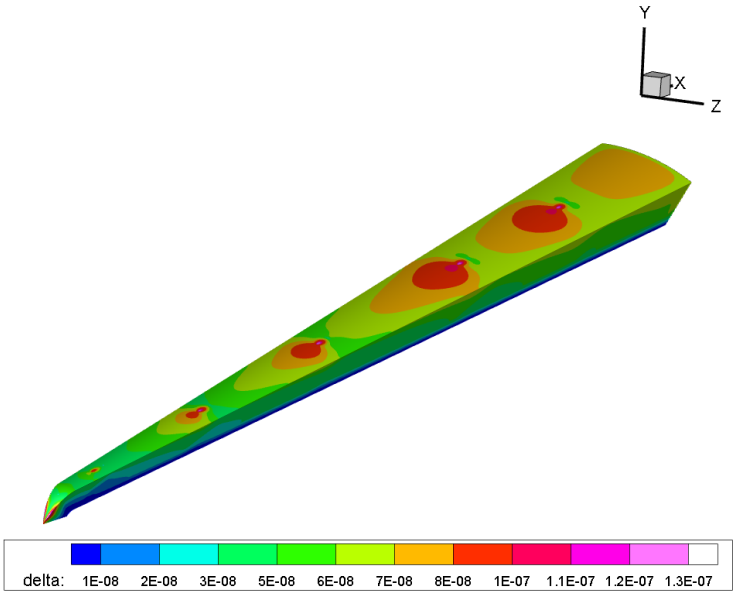

Figure 63. Time Independence of Mach Number Solution on Cone with $R_N = 12.7$ mm at Coarse Refinement Levels

3.5 Distributed Roughness Grid Generation.

The US3D flow solver software is extensible meaning that it provided the capability to augment its functionality through user subroutines without editing the source code. Dinzl wrote a user subroutine for US3D to add the capability to create grids with distributed roughness and applied it to his research in stationary crossflow instabilities on the HIFiRE-5 [21]. The user subroutine was used to create a new US3D library to perform this specialized operation in hacker mode and the US3D library was dynamically loaded [36]. If the new library was present in the current working directory, then it was used instead of the US3D default library [36].

Before starting the distributed roughness grid generation process, a smooth wall grid which has been fully smoothed and proper application of the boundary layer clus-

ter group was required. The connectivity file generated by the US3D pre-processing functionality contained the global information for how the nodes were connected to each other. This connectivity file was necessary information for the distributed roughness grid generation but was not changed throughout the process of creating a distributed roughness grid. The independent grid file, connectivity file, the user routine (us3d_user.f) and the distributed roughness grid generation routine (grid_subs.f) from Dinzl were the necessary tools for the generation of a grid with distributed roughness.

Utilization of the Dinzl user routines to create the distributed roughness required the user to select the proper zone for which the distributed roughness was desired upon and for the user to set the maximum roughness height. The zone for which the distributed roughness was desired upon was selected by the boundary condition type. Since this research effort desired to apply the distributed roughness on to the entire surface of the cone, the surfaces with the solid wall boundary condition were indicated within the Dinzl user routines. Additionally, the user needed to indicate how much roughness was desired within the Dinzl user routines. For this research effort the desired maximum roughness height was the maximum initial roughness measurements taken by Moraru of 15 μm [59]. The amplitude variable controlled the desired maximum roughness height. The actual roughness height (dy) applied to each surface node is calculated by [20]

$$dy = -\frac{1}{2}k + \mathcal{N}k \tag{3.25}$$

where k is the roughness height of 15 μm and $\mathcal{N}$ was a random number was selected between zero and one on a uniform normal distribution. Once the appropriate zone for application has been selected and the amplitude height has been set, the US3D was run in hacking mode to create the distributed roughness grids.

Figure 64a is a visualization of the smooth surface grids and Figure 64b is a visualization of the distributed roughness on the surface of the grid after application of the Dinzl user routines. To aide in visualization Figure 64b had an exaggerated roughness amplitude of 15 x 10^{-4} m. The grid visualization was created using the US3D post-processing functionality. The surface of the cones used in this research with the actual roughness amplitude of 15 x 10^{-6} m is shown in Figure 64c with a magnified portion of the surface to provide a contextual scale for how small the roughness that is hypothesized to cause transition flow. Roughness at the scale shown in Figure 64c was present over the entire surface of the cone.

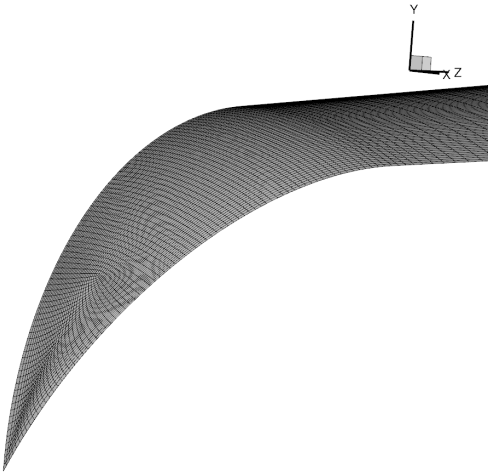

(a) Smooth Surface

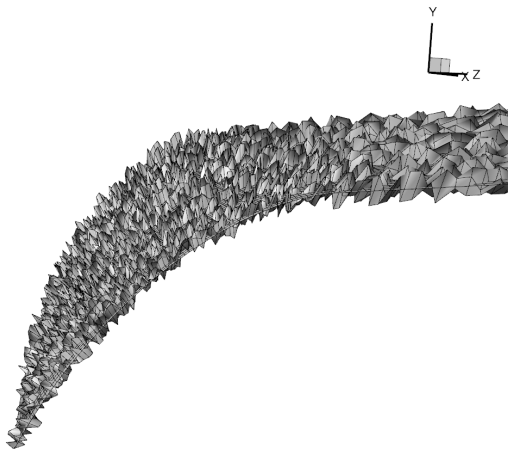

(b) Extreme Surface Roughness

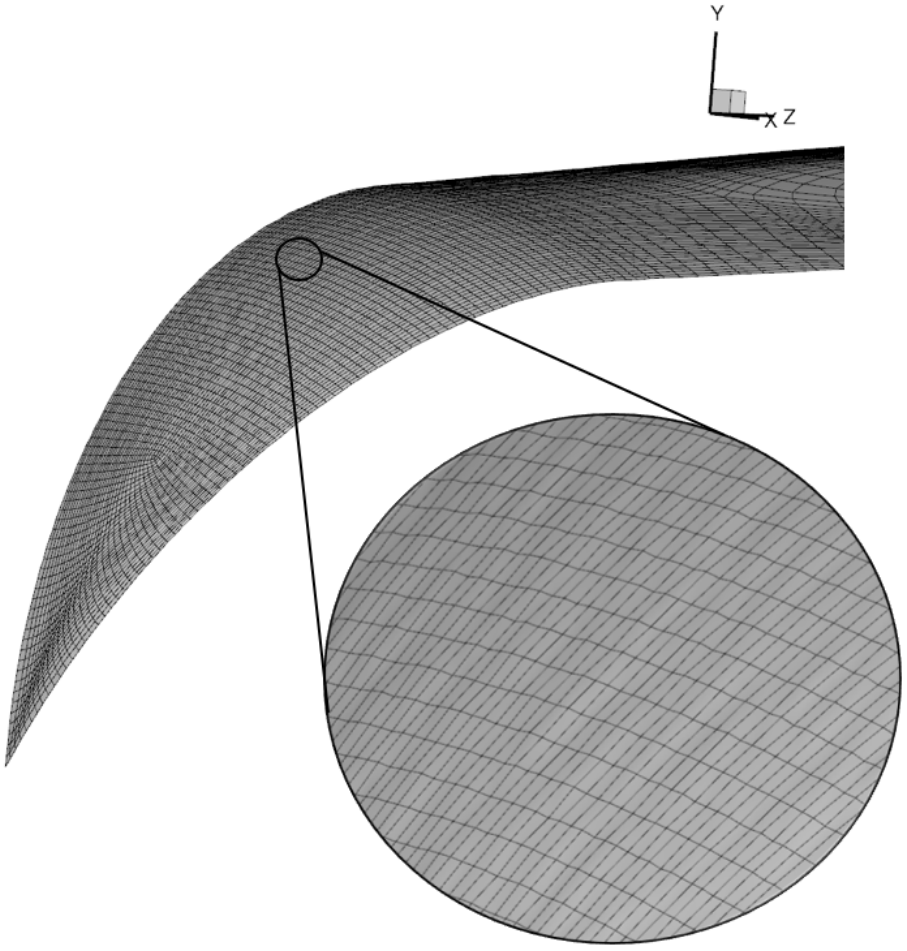

(c) Actual Surface Roughness at 15 μm

Figure 64. Comparison of Baseflow and Roughness Induced Grids

3.5.1 Interpolation of Distributed Roughness Pattern.

Dinzl proved that the roughness pattern must be interpolated from coarse grids onto the medium and fine grids in order for the solutions to produce quantitatively similar data. This concept was discussed in Section 5.1.2 and shown in Figures 25 and 26 with grids made by Dinzl. For this research effort, interpolation was an essential step to prove that the phenomena was not a result of the grid. The computational mesh forces a disturbance at the highest wavenumber possible and was therefore grid density dependent. Hence, the requirement to use interpolation of the roughness pattern onto higher levels of grid refinement provided certainty that the phenomena observed would not be a function of the grid and that the solution was grid independent.

Dinzl wrote a US3D user routine to take a smooth wall grid and create a distributed roughness pattern on the surface [20]. In order to interpolate the roughness onto higher levels of refinement, a user routine must be used on the grid with the lowest level of grid density to create a base pattern of roughness. Then a second US3D user routine, also written by Dinzl, was used to interpolate the roughness pattern from the lower density grid to the smooth wall higher density grid. Figure 65 is a rendering of the surface of the cone coming over the nose at the coarse and fine refinement levels. It follows that Figure 65a had less grid density than Figure 65b; therefore, the contrast of the peaks and valleys of the surface roughness modeled in Figure 65a was more dramatic than the same surface roughness pattern modeled in Figure 65b due to the fact that the fine refinement grid used in Figure 65b had more grid cells to create the rise and descend of each peak and valley. The arrows added in Figure 65 demonstrated the verification that the roughness pattern was interpolated onto the grids of higher refinement by highlighting peaks and valleys which occurred in the same location on the surface regardless of the refinement level.

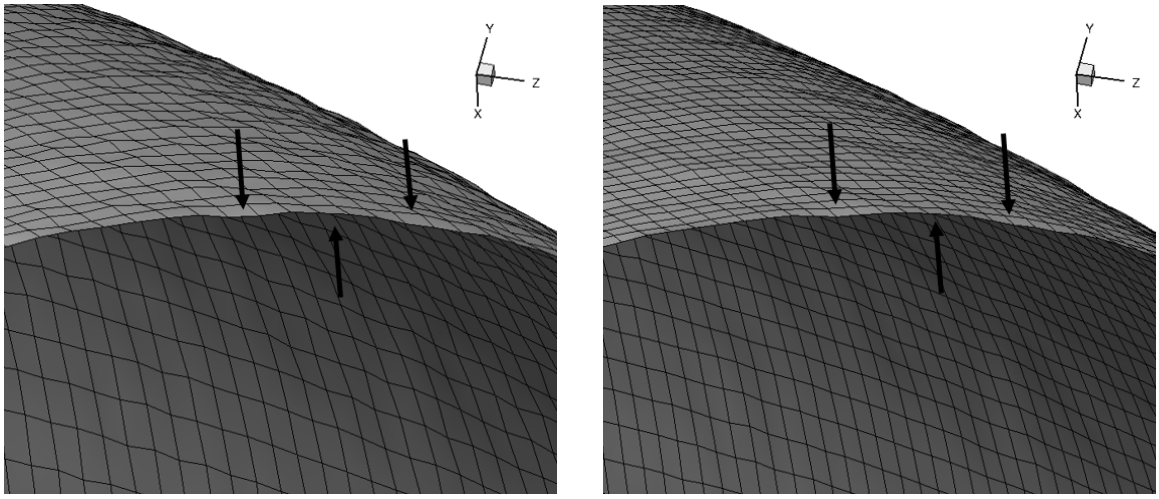

(a) Course Grid Refinement **(b) Fine Grid Refinement**

Figure 65. Interpolation of Cone Surface Roughness

4 Time Accurate Simulation

The time accurate DNS performed on the 7° half-angle cones with the nose radii of 9.5 and 12.7 mm yielded the results in Chapter 4. Running as a time accurate simulation allowed for disturbances within the boundary layer to form and convect spatially downstream the body. Section 4.1 provides temporal methodology of the time accurate simulation and Section 4.2 discusses the spatial methodology employed in the DNS performed in support of the current research effort.

4.1 Timestep Calculation.

The DNS for the distributed roughness grids were run as time accurate simulations. The desired local CFL of one inside the boundary layer drove the requirement for the calculation of the appropriate timestep. The first step to determine the appropriate timestep for the time accurate DNS to achieve a local CFL of one inside the boundary layer was to determine what the current local timestep inside the boundary layer for the converged basedflow solutions. US3D calculated a conservative estimate

of the local timestep via

$$\text{local timestep} = \frac{(\|\vec{v}\| + a)A}{V} \tag{3.26}$$

where the v is the velocity magnitude of the largest face of the cell, a is the speed of sounds, A is the cell surface area, and V is the cell volume. To extract the local timestep information from US3D, a US3D user routine was written by Thompson which leveraged the extensibility of US3D to write the value of the local timestep to the data file [86]. Once the local timestep was calculated throughout the entire solution domain for the baseflow, then the post-processing of a two dimensional slice allowed for the local timestep map like the one shown in Figure 66. The local timestep is not the required timestep for the time-accurate DNS. The time accurate timestep is obtained from the local timestep by the following relationship through the CFL number.

$$\text{CFL}_{\text{local}} = \frac{\text{time accurate timestep}}{\text{local timestep}} \tag{3.27}$$

Since the desired local CFL in the boundary layer was one, the local timestep in the boundary layer equals the appropriate time accurate timestep for this research effort. By magnifying the near surface region, the region where the boundary layer was expected to have formed, in Figure 66 then the local timestep inside of the boundary layer was determined to have been 5×10^{-8}. Figure 66 shows the local timestep for the 9.53 mm nose radius case, however; the local timestep for the 12.7 mm nose radius case was also determined to be 5×10^{-8} by the same process. Subsequently, this timestep was used to calculate the time accurate DNS computations with the grids simulating distributed roughness.

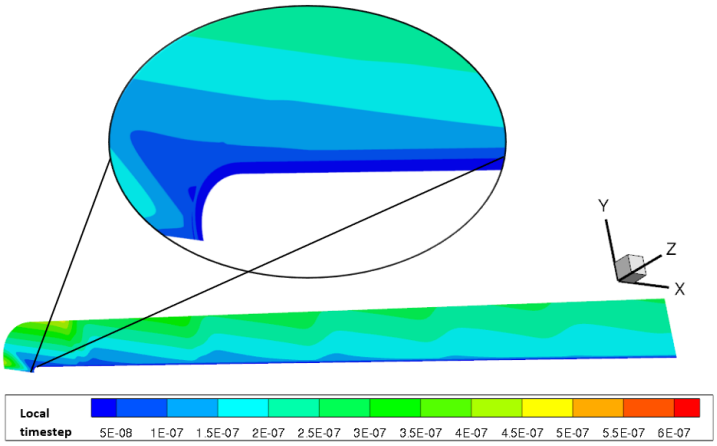

Figure 66. Local Time Step for R_N = 9.53 mm for the Medium Grid Refinement

Once the time accurate timestep was determined, the DNS computations were run with a second order Crank-Nicolson temporal discretization scheme. The Crank-Nicolson scheme is

$$\delta U^n = -\frac{1}{2}\frac{\Delta t}{V}\left(\sum_{faces} F'^n S + \sum_{faces} F'^{n+1} S\right) \tag{3.28}$$

where the exponents n represents the current timestep and $n+1$ represents the next time step, δU is the update to the solution, Δt is the timestep, V is the volume, and F' is the flux vector. This semi-implicit method was chosen because it allowed for these computationally expensive simulations to be run at a larger timestep than an explicit method would allow.

4.2 Spatial Integration.

All of the distributed roughness DNS computations were run as fourth order kinetic energy consistent (KEC) scheme. The KEC scheme was named for the consistent rate of change in the discrete flux of kinetic energy with those predicted by the

momentum and continuity equations [84]. The kinetic energy is defined as

$$\rho k = \rho \frac{u^2 + v^2 + w^2}{2} \tag{3.29}$$

where the kinetic energy is not a conserved variable but will be balanced with the internal energy through the equations for conversation of total energy [84]. Previously, the net change in kinetic energy was only accounted for through the boundaries of the solution [84]. Subbareddy and Candler observed that by calculating the kinetic energy with the other conserved variables throughout the solution the stability of the scheme was substantially improved [84]. To begin the KEC scheme, the vector of conserved variables including kinetic energy was defined by a density weighted average between the current timestep (n) and the future timestep ($n+1$).

$$\begin{bmatrix} -k^\star \\ u^\star \\ v^\star \\ w^\star \end{bmatrix} = \begin{bmatrix} -\frac{u^{\star 2}+v^{\star 2}+w^{\star 2}}{2} \\ \frac{\sqrt{\rho^{n+1}}u^{n+1}+\sqrt{\rho^n}u^n}{\sqrt{\rho^{n+1}}+\sqrt{\rho^n}} \\ \frac{\sqrt{\rho^{n+1}}v^{n+1}+\sqrt{\rho^n}v^n}{\sqrt{\rho^{n+1}}+\sqrt{\rho^n}} \\ \frac{\sqrt{\rho^{n+1}}w^{n+1}+\sqrt{\rho^n}w^n}{\sqrt{\rho^{n+1}}+\sqrt{\rho^n}} \end{bmatrix}$$

These values are used to calculate the convective flux via

$$\begin{bmatrix} \rho u' \\ \rho u' u \\ \rho u' v \\ \rho u' w \\ \rho u' k \end{bmatrix}_f = \rho_f u'_f \begin{bmatrix} 1 \\ \bar{u^\star} \\ \bar{v^\star} \\ \bar{w^\star} \\ \tilde{k^\star} \end{bmatrix}_f$$

where $\bar{u}$, $\bar{v}$, and $\bar{z}$ are spatial averages and the subscript f indicates the value at the face of the cell. Additionally,

$$\tilde{k^\star} = -\bar{k^\star} + \bar{u^{\star 2}} + \bar{v^{\star 2}} + \bar{w^{\star 2}} \tag{3.30}$$

$$\rho_f = (\bar{\rho_f^n} + \bar{\rho_f^{n+1}})/2 \tag{3.31}$$

$$u'_f = (\bar{u^\star} s_x + \bar{v^\star} s_y + \bar{w^\star} s_z) \tag{3.32}$$

where s_x, s_y, and s_z are the direction cosines oriented away from the cell interior. The full derivation of the KEC scheme is available in Reference [84].

In solution domains without shocks, the fourth KEC scheme is stable enough to be solved without the addition of dissipative fluxes. However, in this research effort with a strong bow shock formed ahead of the nose, proper shock capturing through the addition of disspative fluxes was required. The disspative fluxes were calculated via the Ducros switch (α_{diss}), shown below

$$F_{f,diss} = \alpha_{diss} D_f \tag{3.33}$$

where $F_{f,diss}$ was the disspative flux that was added based on the fractional amount of the Ducros switch and D_f was the dissipative portion of a standard shock capturing scheme [22]. The disspative flux is then added to the regularly calculated fluxes for a total flux.

$$F = F + F_{f,diss} \tag{3.34}$$

Since the Ducros switch ranged between zero and one the disspative flux term was only used when necessary. In laminar regions of the flow, the Durcos tended towards zero and minimal dissipative flux was added to the solution. In regions of flow where compressibility effects dominated, the Ducros switch tended towards a value of one

and the full magnitude of the dissipative flux was applied to the solution domain [22]. The Ducros switch was calculated locally by

$$\alpha_{diss} = \min\left(\frac{\theta^2}{\theta^2 + \omega^2 + \epsilon}, 1\right) \tag{3.35}$$

where ω is the vorticity magnitude, θ is the divergence of the velocity, and ϵ is a small number that prevents division by zero [22]. In simulations conducted by Subbareddy and Candler, it was determined that the dissipation added by the Ducros switch method of shock detection in combination with the sixth order KEC did not compromise the solution because only very low levels of disspative flux was functionally added to the solution [84].

US3D flow solver code allows for second, fourth, and sixth order KEC spatial discritization. Originally, the desire was to run the DNS utilizing the full sixth order KEC spatial discretization capabilities. However, the sixth order KEC implementation was very sensitive in terms of stability for this research application. Due to the stability restrictions, the fourth order KEC spatial discritization was chosen as the appropriate discretization for this research effort.

5 Pressure Power Spectral Density

Pressure power spectral density (PSD) calculations reveal how the magnitude of the pressure fluctuations change as a function of frequency for the entire time history of the run. The experimental pressure PSDs were calculated by Moraru and were discussed in Section 1.3. In order to calculate the computational pressure PSDs the data collection system must be replicated on the computational models of the cones with the nose radii of 9.53 mm and 12.7 mm as provided in Section 5.1. Subsequently in Section 5.2, the methodology for turning the collected data into the pressure PSDs

for comparison with Figure 44 is presented. Results and corresponding analysis of the computational pressure PSDs are available in Section 3.3.

5.1 Data Collection.

Conceptually, the collection of data on an experimental model and a computational model were the same. On the AEDC Tunnel 9 experimental 7° cones with nose radii of 9.53 and 12.7 mm the various thermocouples, PCB sensors, and kulite sensors were placed along the 0°, 90°, and 180° streamwise rays as shown in Figure 42. Moraru provided the streamwise coordinates of each sensor location in Reference [59]. The streamwise coordinate of the experimental model sensor placement was translated into its Cartesian coordinate along the 0° ray for the computational model. The Cartesian coordinates of the 9.53 and 12.7 mm computational model sensor location is available in Appendix A. Only one ray of data was needed for the computational models of the axi-symmetric cones because neither uncertainty nor interference associated with the sensor readings were obtained as would take place in an experimental research effort.

The Cartesian coordinates correspond to a face location on the computational model. US3D has inherent capabilities to read in the Cartesian coordinates and return the global face number by identifying the closest centroid of a cell to the Cartesian coordinates given. Chaudhry wrote a US3D user routine named FindElem to leverage this capability [15]. In essence, the face identified by the FindElem user routines becomes the "sensor" and data at that location can be post-processed. For the current research effort, pressure was the chosen data set to collect at each sensor location to be consistent with the experimental pressure PSDs in Figure 44 calculated by Moraru [59]. The Cartesian coordinates of the sensor location did not change between the coarse and fine grids. However, the FindElem user routines was run

separately for each grid refinement level because the global cell numbering assigned by US3D was consistent between the two grids. In other words, the location of the sensor did not change, but the number of the corresponding face did.

5.2 Computational Calculation Methodology of Pressure PSD.

Once the sensor locations have been selected on the grids which simulated distributed surface roughness, then a time accurate DNS was run to collect the pressure data. The time accurate simulations were run with a fourth order KEC spatial discretization and a second order Crank-Nicholson temporal discretization. Chaudhry wrote a second US3D user routine (PrintElem) which decomposed the collected data into the mean and fluctuating components in accordance with Equation 2.9 and printed the power spectrum for the selected flow variable by leveraging the Fastest Fourier Transform in the West (FFTW) library for computing discrete Fourier transforms (DFT). The FFTW wisdom functions by selecting the optimal way to compute the Fourier transforms. Specifically, the FFTW wisdom functionality chooses the correct windowing scheme for the array of data provided. The results of the pressure PSDs for the computational model are provided in Section 3.3.

6 Concluding Remarks

Chapter 3 first covered the pertinent details of the AEDC Tunnel 9 hypersonic experiments on the 7° half-angle cones of increasing nose radii which this research effort sought to recreate via DNS CFD computations. Then, the creation of the smooth computational domain was elucidated through the instability resolution study. Next, the baseflow computations were computed and analyzed through grid independence studies. Once the approach for creating the distributed roughness grid generation was detailed, the procedure for how the time accurate DNS CFD were computed was

provided. Finally, the methodology for calculating the computational pressure PSDs was provided. The results from the time accurate DNS and the pressure PSDs are available in Chapter 4.

IV. Implementation and Analysis

The departure from modern modal transition theory on axi-symmetric cones with increasing nose radii at hypersonic conditions was first documented by Stetson [79]. Modern modal transition theory established that for a second mode dominated transition, as the nose radius increased the transition location moved aft on the geometry [72]. However, in the Stetson experiments this precedent for second mode dominated transition was not upheld for cones with a substantial amount of bluntness. In support of the Stetson experiments, the same non-modal behavior was observed in the Arnold Engineering Development Center (AEDC) Hypervelocity Wind Tunnel 9 experiments which included six, 7° half-angle cones at Mach 10 with increasing nose radii. Figure 67 shows the results of the AEDC Tunnel 9 experiments where the break with modern modal theory was observed as the nose radius increased from 9.5 mm to 12.7 mm. The anticipated downstream movement of the transition onset location for the 12.7 mm case was negligible and indicated a break in the established second mode dominated precedent.

The cause of the non-modal transition between the 9.53 mm and 12.7 mm nose radii cases is not known but one of the leading hypothesis is that the non-modal transition occurred due to transient growth of the instabilities introduced from the distributed surface roughness on the test articles. Therefore, the goal of this research effort was to explore distributed roughness as a possible cause for the non-modal transition observed on 7° half-angle cones with the nose radius of 12.7 mm. The nose radius of 9.53 mm was also included in the simulations as an anchor point to the research as it was the last case to have experienced second mode dominated transition as shown in Figure 67. In efforts to accomplish this research, Section 1 provides the initial DSN results with distributed surface roughness grids and some concerns with the initial results. Correspondingly, Section 2 details the steps taken to correct the

concerns with the initial results. Section 3 concludes the chapter with the final results which includes comparisons to the experimental data and the computational pressure power spectral density calculations.

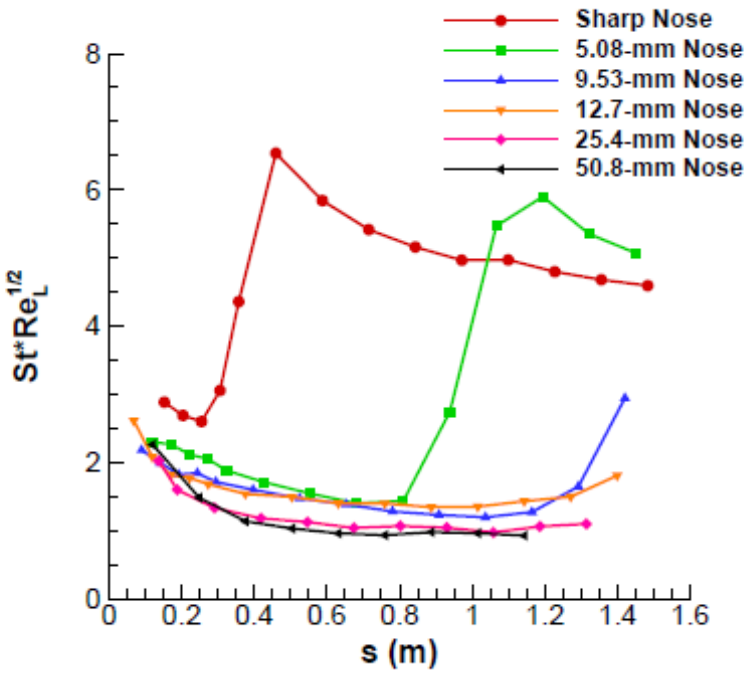

Figure 67. Heat transfer profiles for varying nose radii at Mach 10 and zero angle of attack with Re = 15×10^6 /m (sharp nose) and Re = 17×10^6 /m (blunt nose) (used with permission) [59]

1 Initial Rough Body Simulation Results

The six, axi-symmetric 7° half-angle cones with a length of 1.55 m and increasing nose radius tested by Moraru in the AEDC Tunnel 9 are shown in Figure 68. The geometries chosen for this research effort were limited to the nose radii (R_N) cases of 9.53 mm and 12.7 mm. The 9.53 mm nose radius case served as a baseline case because it was the last cone to have exhibited second mode dominated transition behavior in the AEDC Tunnel 9 experiments [59]. The 12.7 mm nose radius case was

chosen because it was the first cone to have exhibited behavior which departed from the established second mode dominated transition precedent [59]. The established second mode dominated transition precedent stated that the transition location would move aft on the geometry as the nose radius increased [72]. However, Figure 67 demonstrates that the 12.7 mm nose radius case ceased to uphold the established second mode dominated transition precedent by maintaining approximately the same transition location as the 9.53 mm case. The computational fluid dynamic (CFD) direct numerical simulations (DNS) were run at Mach 10 with a fourth order kinetic energy consistent (KEC) spatial discretization scheme and a second order Crank-Nicholson temporal discretization scheme.

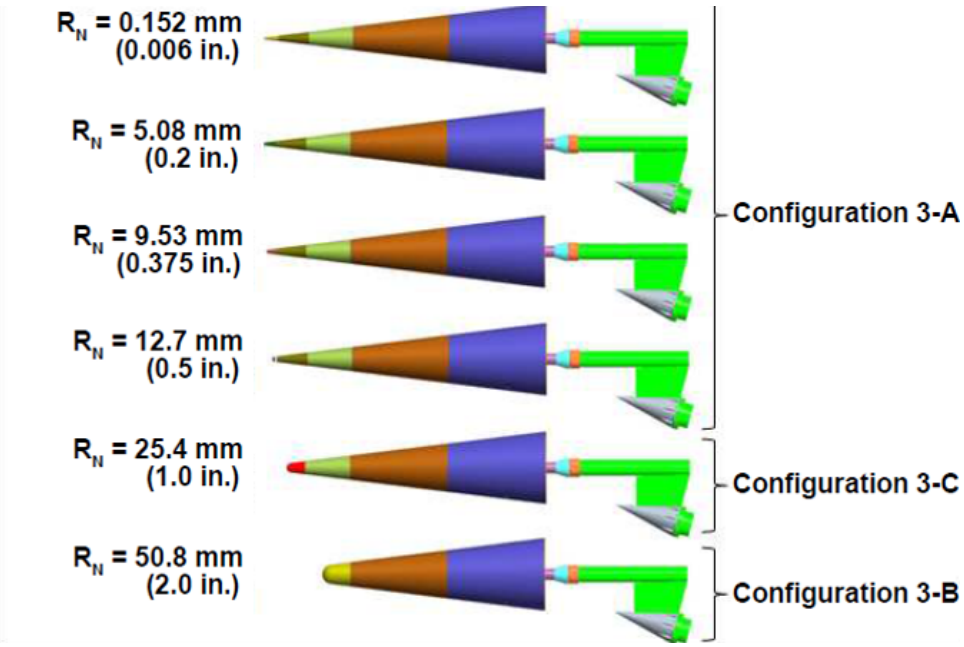

Figure 68. AEDC Tunnel 9 Experimental Configurations for 7° Axi-Symmetric Cones with Increasing Nose Radii [54]

The creation of the computational domain which simulated distributed surface roughness along the entire surface of the cone was described in Chapter 3 Section 3.5. Taking into consideration the results on the instability resolution study conducted in Chapter 3 Section 2.1, the grid independence study conducted in Chapter 3 Section

3.3, and the amount of computational resources available. The decision was made to continue with only the fine grids. The time accurate simulation began in the computing environment provided by the Department of Defense High Performance Computers (DoDHPC). The distributed surface roughness simulations started from the converged smooth wall solution because the overall establishment of the flow was not expected to change significantly since the geometry was consistent between the distributed surface roughness simulations and the smooth wall simulation.

The first indication that an unforeseen factor preventing conclusive results was the timestep required to run a time accurate solution was on the order of 10^{-12} instead of the value of 5×10^{-8} which was computed in Chapter 3 Section 4.1. The scheme was too unstable to support a larger timestep. The second indication that an unforeseen factor was preventing conclusive results was the residual calculation. As the distributed surface roughness simulation ran, a residual calculation was performed at each iteration. The residual calculation was a reflection of the maximum change in the solution and thus served as an indication of when the flow had reached a steady state solution. As stated in Chapter 3 Section 3.2, the residual calculation the smooth wall solution was on the order of 10^{-6}. When starting the distributed surface roughness simulations from the smooth wall solution, the residual calculation was expected to initially spike to much greater orders of magnitude as the flow adjusted to the forced disturbances caused by the distributed surface roughness. This initial spike did manifest in the distributed surface roughness simulations and the distributed surface roughness simulations achieved a maximum residual calculation on the order of 10^{7}. Turbulent flow was expected to form in both nose radii cases therefore a residual calculation on the order of 10^{-6}, as was expected in the smooth wall solutions, was unrealistic. However, the initial distributed surface roughness simulations never achieved a residual calculation on the order of magnitude less than 10^{6}.

Due to the remaining high residual calculation, it was impossible to determine if a steady state solution was achieved. Therefore, finding the source of the residual error in the solution became the next logical step. Figure 69 plotted the contour of the residual in the computational domain and provided crucial insight into where the large change in the solution had occurred. The source of the error which prevented the residuals from decreasing below an order of magnitude of 10^6 was the error forming at the bow shock in front of the geometry as shown in Figure 69. The reason the error in the bow shock region occurred was due to the misalignment of the cell faces to the shock. Specifically, the alignment of the angle between the outward normal vector from the cell face and the vector indicating the gradient of change in conserved flow variables over the bow shock [18]. Chapter 3 Section 2.3 described the special grid considerations taken to create a grid which optimized the cell alignment for modeling the boundary layer. However, the bow shock presented a second region of important fluid dynamics which had no special grid considerations taken to accurately model thus far. The bow shock error invalidated the initial solution. Steps taken to reduce the error in the bow shock region are discussed in Section 2. Figure 69 is provided only for the 9.53 mm nose radius case but the 12.7 mm nose radius case resulted in the same conclusions and demonstrated the same issues at the 9.53 mm case.

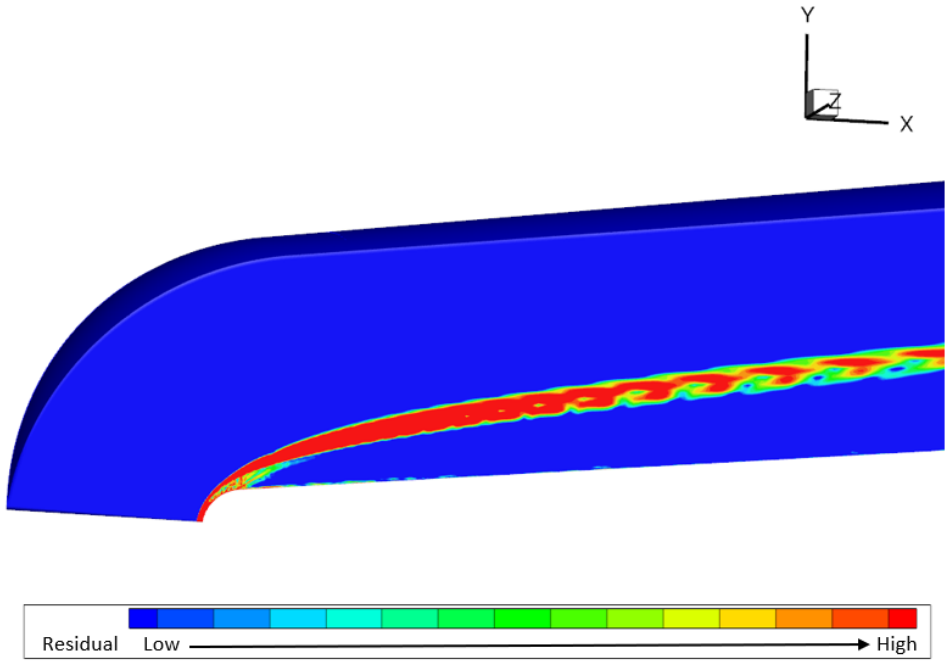

Figure 69. R_N **= 9.53 mm Residual Contour**

While the residual contours revealed the overall source of error present in the flowfield which was preventing good numerical data, these same contours also revealed proof the the broadband forcing caused by the distributed surface roughness was taking effect. Figure 70 was oriented so that the bottom on the computational grid, or the cone surface with the applied surface roughness was shown to the reader. From the presence of the residual error in varying quantities along the entire surface of the cone in Figure 70 it was concluded that the applied distributed surface roughness was forcing the flow in the intended manner.

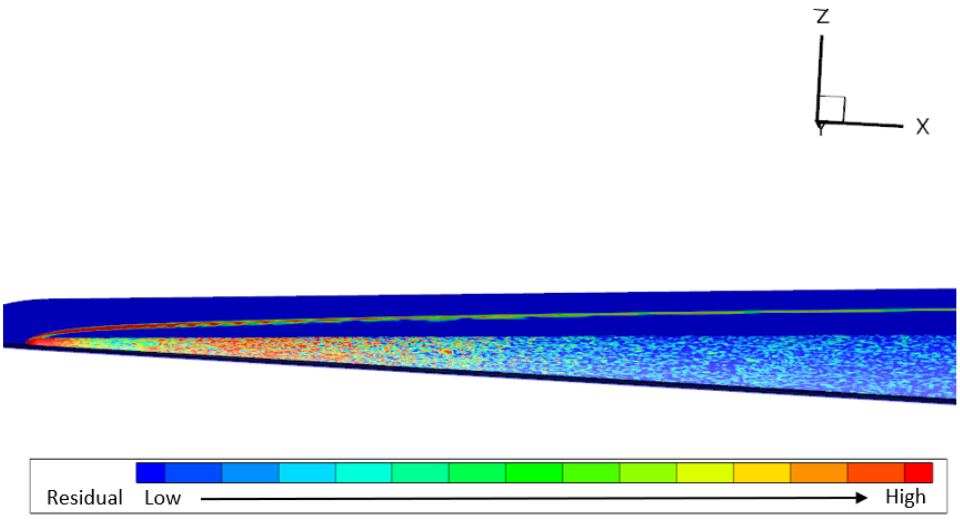

Figure 70. Residual Contour of Cone Surface with Applied Distributed Roughness

2 Grid Tailoring

To correctly account for the bow shock forming over the 7° half-angle cone with the nose radii of 9.53 mm and 12.7 mm, the US3D grid tailoring tool was employed. Once the grid has been built through an independent gridding software, like Link3D, and the solution had been run long enough to have established a flowfield, then the distribution of the grid cells can be adapted using the US3D software grid tailoring tool. The grid tailoring tool maximizes the impact of the current cell density through a redistribution of the cells which aligns the cell faces with the dominating flow features for proper modeling. The grid tailoring functionality changes the distribution of the grid points along the topology lines from one boundary to another. In this research effort, the grid tailoring tool changed the distribution of grid points along the topology lines normal to the cone surface. Initially, when the grid density of a topology line was set in the gridding software, the distribution of grid points was even along the topology line. Section 1 provided that this caused large, unchanging residual calculations in the bow shock region which resulted in an unsettled solution. Grid tailoring can

adjust the distribution of cells along a topology line to achieve high cell density near relevant flow features and low cell density in areas of less interest without affecting the computational cost since the number of total cells in the grid remained constant. This redistribution is known to be particularly helpful in flows containing shocks or other discontinuities and was heavily utilized in the modeling of the HiFIRE-5 geometry [21] and the BOLT geometry [42]. The grid tailoring capability of US3D was applied only to the cells in the direction normal to the cone surface. Therefore, the careful consideration taken in Chapter 3 Section 2.1 to achieve proper spatial resolution in the streamwise and spanwise direction for instability detection was not affected. The goal in applying the grid tailoring tool was to increase the cell density near the bow shock by removing cell density above the bow shock when freestream conditions were achieved.

Figure 71 demonstrates that the freestream solution was achieved well before the end of the computational domain was reached. Therefore, the cells in the freestream solution region could be much larger and achieve the same level of accuracy in the solution than the cells in the bow shock or boundary layer region. On first appearance, an argument could have been made that the computational domain was too large in the direction normal to the surface of the cone and modeling above the bow shock was a waste of computational resources. However, the extra grid cell density that was used to create the region of the domain above the bow shock was the feature that made grid tailoring an option for this research effort.

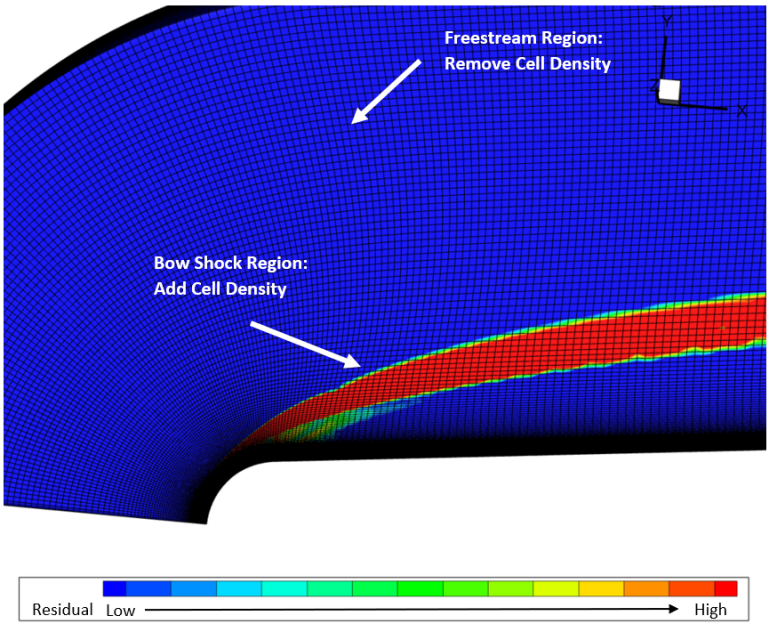

Figure 71. Grid Before Tailoring with Residual Contour

The methodology of grid tailoring was based on the specified value of initial nondimensional wall coordinate spacing (y^+) and then the grid is adapted via a geometric growth function or via a hyperbolic tangential function. The initial spacing is defined as

$$y^+ = \frac{y\rho u_\tau}{\mu} \tag{4.1}$$

where y is the distance from the wall to the first cell centroid, and u_τ is the friction velocity defined as

$$u_\tau = \sqrt{\nu \left.\frac{\partial u}{\partial s}\right|_{y=0}} \tag{4.2}$$

The equation for geometric growth is

$$s_{max} = \sum_{j=2}^{N} g^{j-2} ds_0 \tag{4.3}$$

where g is the growth rate, N is the number of cells in the j direction, and ds_0 is the

spacing of the first cell away from the wall at the $j = 2$ location. The equation for the hyperbolic tangential function is

$$s(\xi) = 1 + \frac{tanh\left[\delta\left(\frac{\xi}{N} - 1\right)\right]}{tanh(\delta)} \tag{4.4}$$

where ξ is the computational domain and δ is the stretching function.

For the present research effort, the grid point distribution method was a one-sided hyperbolic tangent function with a specified initial nondimensional wall coordinate spacing (y^+) of 0.95 at the wall and no adjustments were made to the outer boundary to the shock. US3D calculated the appropriate spacing the direction normal to the surface of the cone (Δy) based on the designated value of y^+. These specifications guaranteed that proper wall coordinates were always maintained throughout the cell redistribution in effort to maintain proper modeling of the boundary layer. The shock detection sensitivity was set to 0.001% and this variable functioned as a threshold for where tailoring would occur within the solution. If the flow solver detected a change in the solution over 0.001% from the solution of the previous iteration, then the grid cells were tailored smaller to reduce the error in that area.

The grid tailoring functionality can be applied on any data set in which the entire flowfield has been established. Traditionally, grid tailoring is applied to the converged laminar data set because the shape and location of the bow shock would not be expected to move significantly in the flowfield. However, once the grid tailoring has been applied the grid information was no longer stored in the grid file and began to be stored in the data file. Thus, tailoring the laminar solution was not an option for this application because the user routines to create distributed surface roughness were built to receive and modify a grid file, not a data file. Therefore, the grid tailoring was applied after the distributed roughness application and interpolation and after

the flowfield was established with the grids which simulated a surface with distributed roughness.

Figure 72 presents the grid before and after the grid tailoring. In Figure 72a the cells near the shock surface are smaller than the cells near the shock surface in Figure 72b. The comparison of Figures 72a and 72b prove that the grid was adjusted based on the grid tailor function. Originally, the grid before tailoring was created to have a high degree of isotropy in the cells normal to the surface. Isotropy of a cell aids in reducing grid induced error. However, one unintentional side effect of the grid tailoring was that some of that isotropy was lost in the grid after tailoring. The grid tailoring function redistributed the cells in accordance to where to flow calculated the highest residual and did not have a consideration of cell isotropy. The loss of well established isotropy was accepted because the accuracy of the overall solution improved with the grid density redistributed to the flowfield areas of high change.

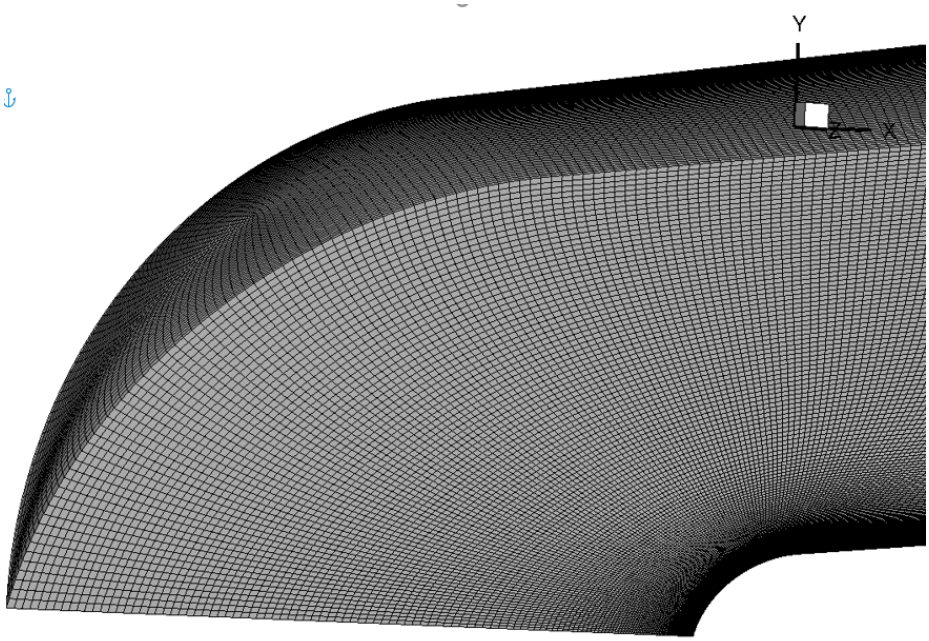

(a) Grid Before Tailoring

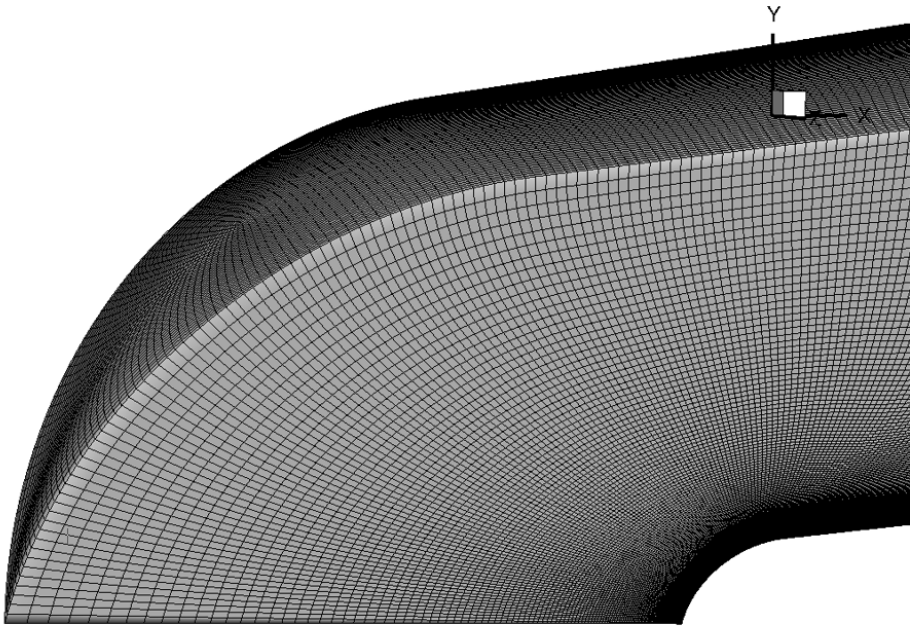

(b) Grid After Tailoring

Figure 72. Comparison of the Grid Before and After Tailoring

3 Final Rough Body Results

Figure 70 demonstrated that the disturbed surface roughness was properly modeled on the surface of the cones through the application method described in Chapter 3 Section 3.5; however, Figure 69 proved that the flowfield was plagued by high residual dominating the flowfield caused by cell face alignment with the bow shock region. In response to the concentration of residual present in bow shock region, the grid tailoring functionality of US3D was used to change the alignment of the cells faces with the bow shock. After the grid tailoring was performed, the time accurate DNS was repeated. Section 3.1 compares the results of the DNS to the results of the AEDC Tunnel 9 experiments conducted by Moraru. Section 3.2 provides comparison between the smooth body and rough body simulations. Subsequently, Section 3.3 details the computational pressure power spectral density (PSD) calculations and an analytic comparison to the experimental pressure PSDs. Finally, Section **??** analyzes the instability growth or decay based on the N factor calculations.

3.1 Heat Flux Calculations.

In the experimental data, boundary layer transition was inferred by a sustained increase in heat flux above the smooth wall baseflow solution computed by Moraru [59]. The same method of determining boundary layer transition was applied to this research effort. To determine if transitional flow was caused by the addition of distributed surface roughness the same heat transfer post-processing procedure discussed in Chapter 3 Section 3.2 which was used to create the smooth wall solution comparison between Moraru's laminar solution, and the present research's smooth wall solution shown in Figure 60b was repeated. Consequently, Figures 73 and 74 were created to provide a comparison with Moraru's experimental heat transfer data, the smooth wall calculations from the present author, and the DNS with the distributed

surface roughness. As with the procedure described in Chapter 3 Section 3.2, the data in Figures 73 and 74 were nondimensionalized by the Stanton number (St), calculated via Equation 1.1, and the Reynolds number based on cone length (Re_L).

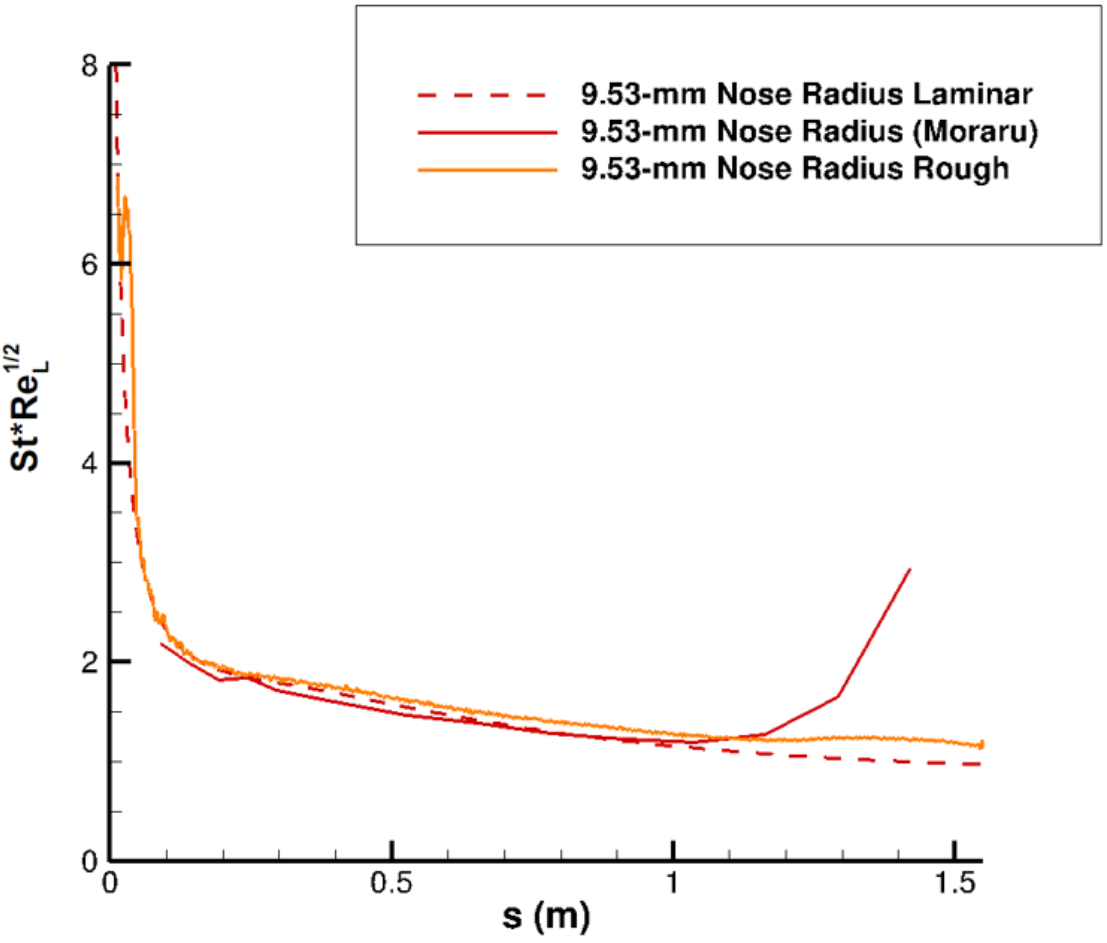

Figure 73. Heat Flux Comparison Between Moraru Experimental Data [59] and Distributed Surface Roughness DNS for R_N = 9.53 mm

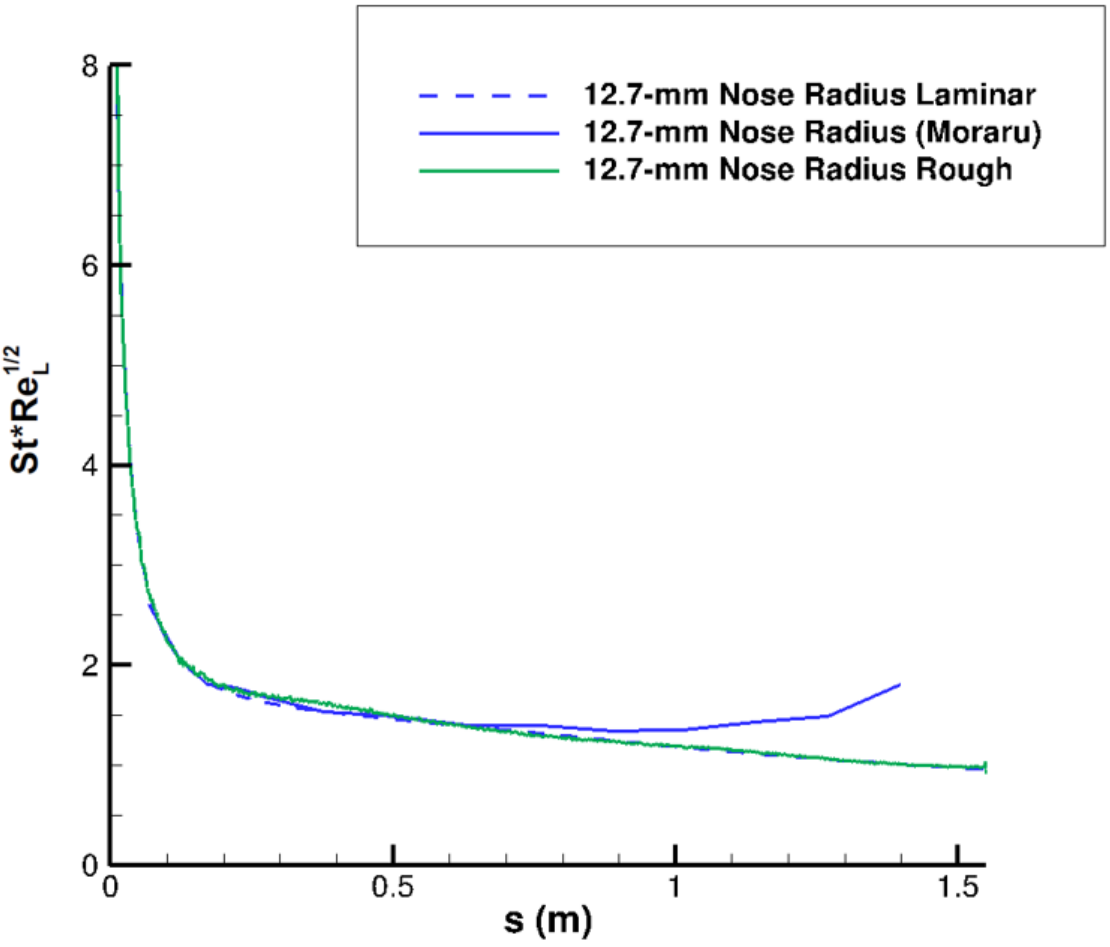

Figure 74. Heat Flux Comparison Between Moraru Experimental Data [59] and Distributed Surface Roughness DNS for R_N = 12.7 mm

Figures 73 and 74 showed that the distributed surface roughness simulations of the present research effort did not yield an increase in heat flux which would be indicative of transition in either the 9.53 mm or the 12.7 mm nose radius case for the entire length of the cone. The computational distributed surface roughness lines shown in Figures 73 and 74 have shapes which resemble the smooth wall streamtraces and not the experimental lines which demonstrated transition. However, upon closer inspection of the lines produced by the distributed surface roughness DNS in Figure

75, the effect of the distrusted surface roughness was shown in the jagged nature of the lines as opposed to the smooth lines of the smooth wall computations. The jagged nature of the lines provided proof that the distributed surface roughness was effecting the solution as intended. The analysis of Figures 73 and 74 against Figure 75 informed the conclusion that the distributed surface roughness alone was not enough of an environmental disturbance to cause transition to occur on these geometries at the current conditions.

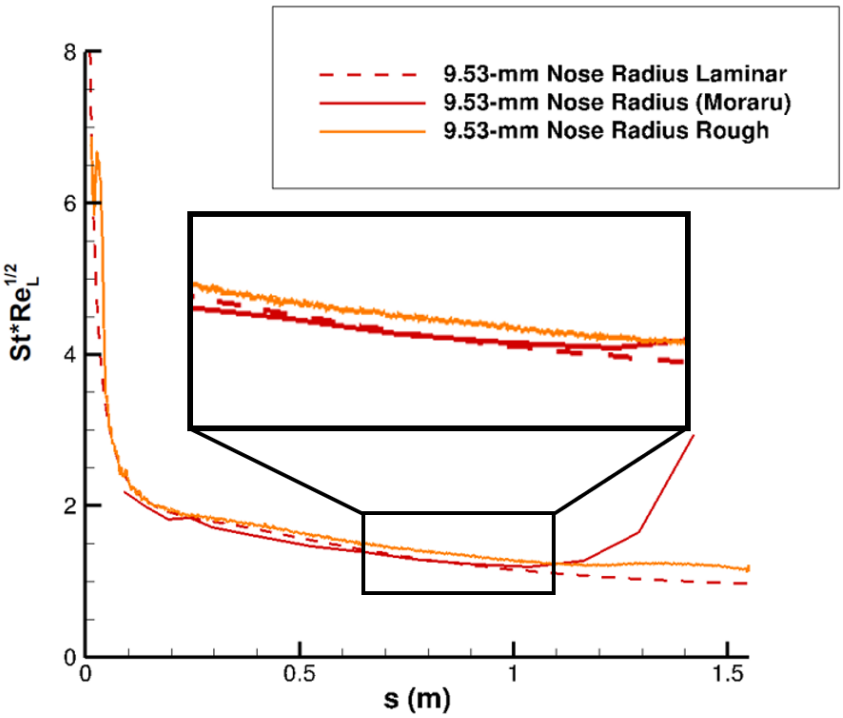

(a) R_N = 9.53 mm

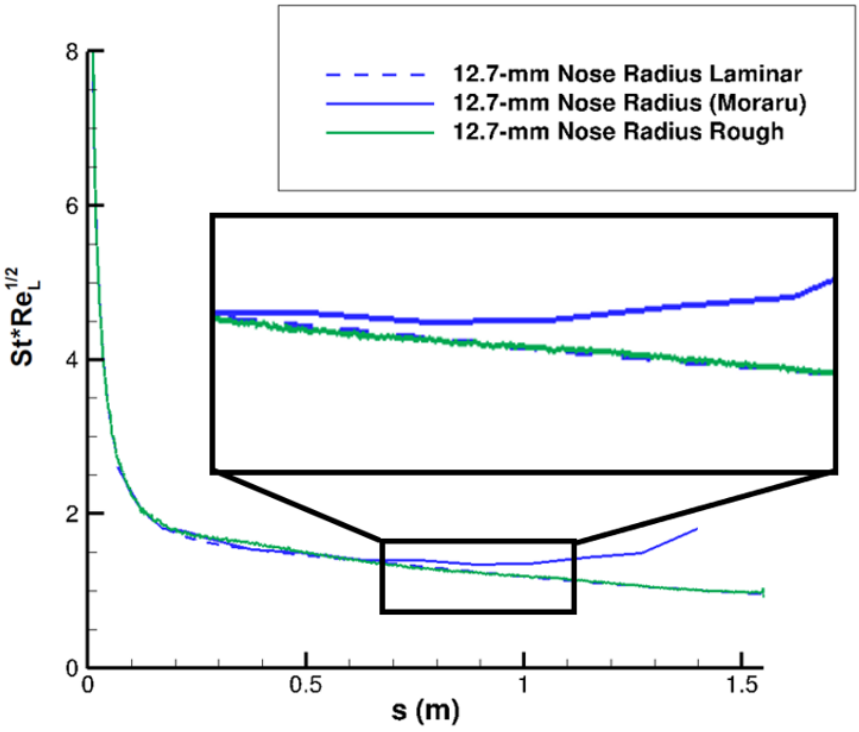

(b) R_N = 12.7 mm

Figure 75. Close Analysis of the Heat Flux Comparison Between Moraru Experimental Data [59] and Distributed Surface Roughness DNS

The last cone to experience a second mode dominated transition in the experiments conducted by Moraru was the 9.53 mm nose radius case [59]. Therefore, the 9.53 mm nose radius cone was chosen to serve as a base case for this research effort. However, in the distributed surface roughness DNS, the 9.53 mm nose radius case failed to produce transitional flow as evident in Figure 73. From Figure 75 it was concluded that the forcing function caused by the distributed surface roughness manifested in the same manner for both the 9.53 mm and the 12.7 mm nose radii cases. Therefore the pressure fluctuation analysis presented in the current section was performed on only the 9.53 mm nose radius case, but the conclusions apply to both geometries. To characterize the instabilities caused by the distributed surface roughness on the nose for the 9.53 mm nose radius case, a surface contour of the pressure fluctuations was created in Figure 76. Similarly, a contour of the pressure fluctuations was created for the y-symmetry plane of the 9.53 mm nose radius case in Figure 78. The pressure fluctuations were computed by

$$P' = P - \bar{P} \tag{4.5}$$

where the pressure measurements (P) was decomposed into the mean pressure of the cell ($\bar{P}$) and the fluctuating component (P'). The surface of the nose obtained higher pressure fluctuations than the body. Since distributed surface roughness was a constant forcing function and the resulting instabilities did not lead to transition, the fluctuations maintain a stationary pattern on the surface of the cone. This stationary pattern is observed on the nose surface of the cone in Figure 76 and from the Y-Symmetry plane view in Figure 77.

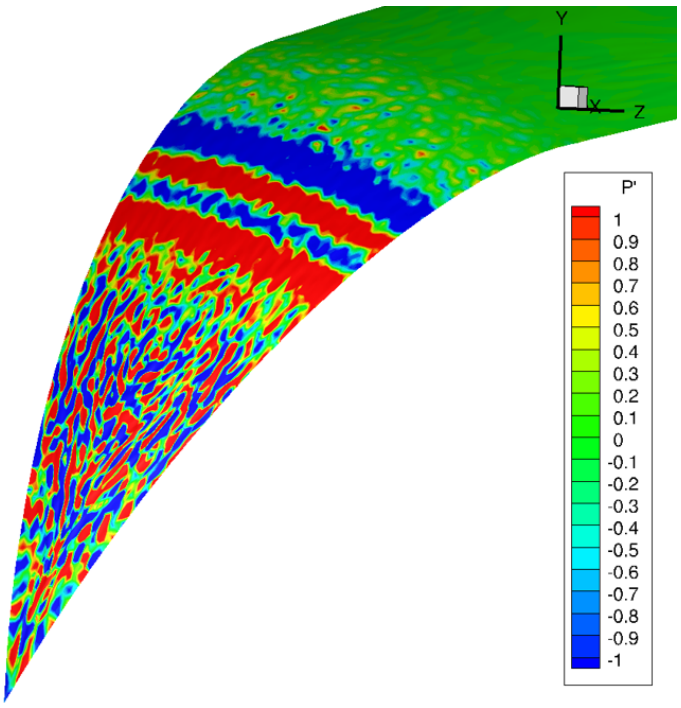

Figure 76. Pressure Fluctuations on the Nose of the R_N = 9.53 mm Cone at Mach 10

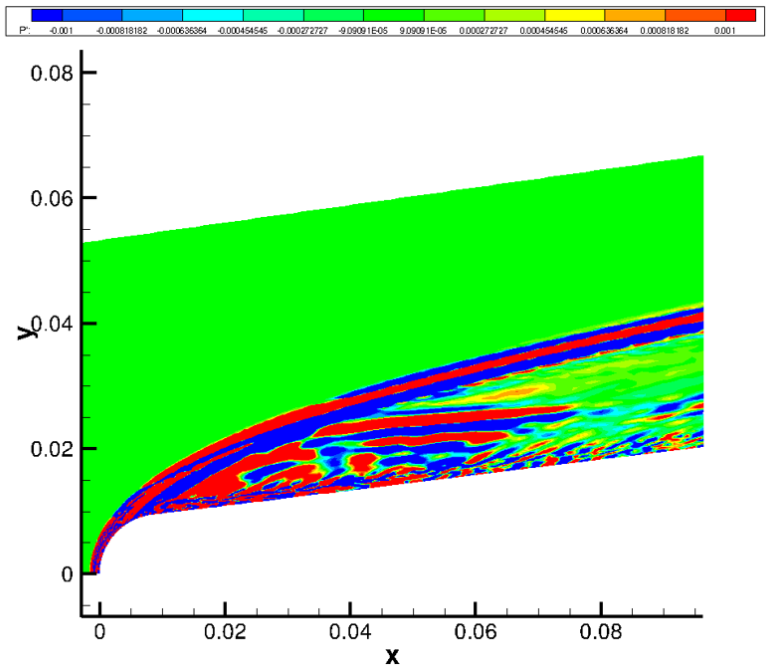

Figure 77. Pressure Fluctuations on the Nose Region of the Y-Symmetry Plane of the R_N = 9.53 mm Cone at Mach 10 with Distributed Surface Roughness

Figure 78 revealed two regions of high pressure fluctuations. The first region of high pressure fluctuations was along the surface of the cone where the distributed surface roughness was taking effect. The second region of high pressure fluctuations occurred at the bow shock location. Cross-referencing Figure 69 with Figure 78 confirmed that the grid was not tailored aggressively enough to eliminate all residual in the bow shock region. To apply the tailoring function capability the number of tailoring passes was specified within the input deck. After the tailoring passes were applied then the grid had to be re-smoothed. Note that the re-smoothing performed by the grid tailoring function does not refer to the smooth or rough quality of the surface grid. Then the flow had to be re-established with the new tailored grid. To intensify the level of grid tailoring, the number of tailoring passes could have been increased or the whole grid tailoring, re-smoothing, and re-establishing process could have been applied multiple times to the solution domain. The present research effort applied 100 tailoring passes and applied the whole grid tailoring function three complete times to the 9.53 mm nose radius case and two complete times to the 12.7 mm nose radius case. However, as evident in Figure 78, the grid tailoring was insufficient to completely align the cell faces to the bow shock, and as a result there was a large degree of pressure fluctuations present in the bow shock region.

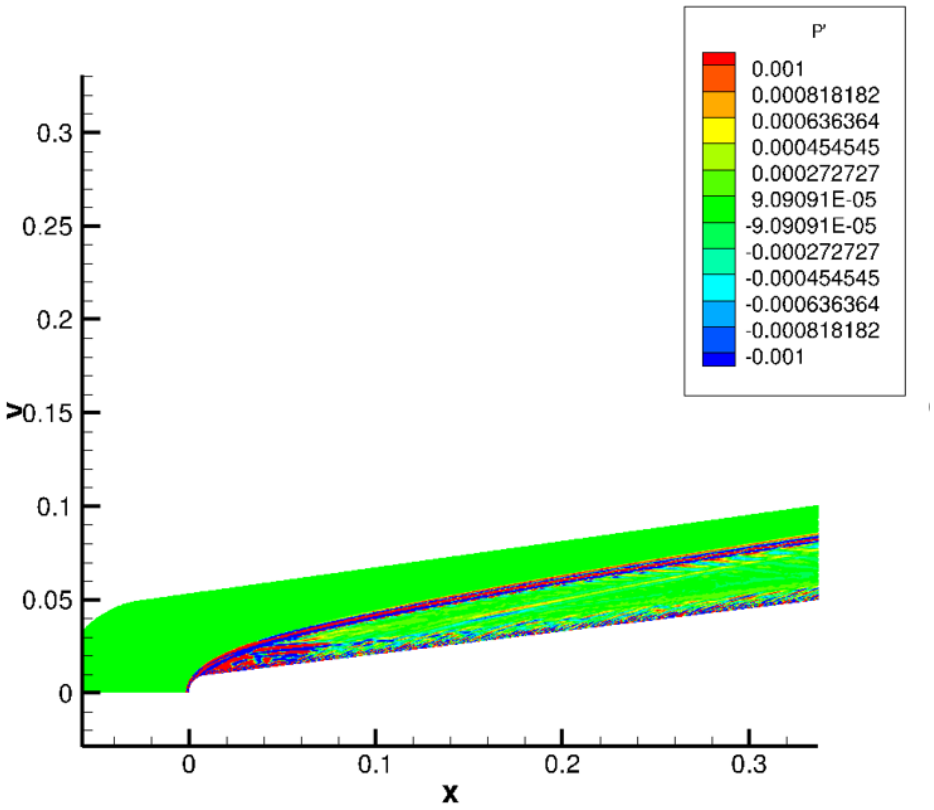

Figure 78. Pressure Fluctuations on the Y-Symmetry Plane of the R_N = 9.53 mm Cone at Mach 10 with Distributed Surface Roughness

Figure 79, focuses attention on the region of pressure fluctuations near the surface of the cone where the black box highlights the revealed instabilities which formed above the surface roughness. The pattern of the instabilities forming in Figure 79 resembled the supersonic mode instabilities shown in Figure 19 and discussed in Chapter 2 Section 4.4. Recall that the supersonic mode instabilities occur when an unstable second mode instability synchronizes with the slow acoustic spectrum causing the disturbance to travel upstream supersonically relative to the mean tangential flow outside of the boundary layer [40]. In Figure 19, which provided a schematic of the supersonic mode, there were three regions defined by the relative Mach number. The relative Mach number compared the speed of the instability relative to the

mean flow velocity component tangential to the wall. In the first region, the second mode instabilities formed and bounce between the sonic line and wall geometry like a trapped acoustic wave. In Figure 79 there were evidently instabilities formed from the distributed surface roughness acting as a forcing function. However, it was apparent from Figures 73 and 74 that these instabilities did not lead to transition. In the second region, or the subsonic region, of the supersonic mode schematic presented in Figure 19, was where the "rope-like" structures formed in the flowfield. These "rope-like" structures take on a similar form as the instabilities in the black box of Figure 79. In the final region of the supersonic mode schematic the decaying Mach waves formed above the boundary layer. In a similar manner, decaying Mach waves were apparent above the boundary layer in Figure 79.

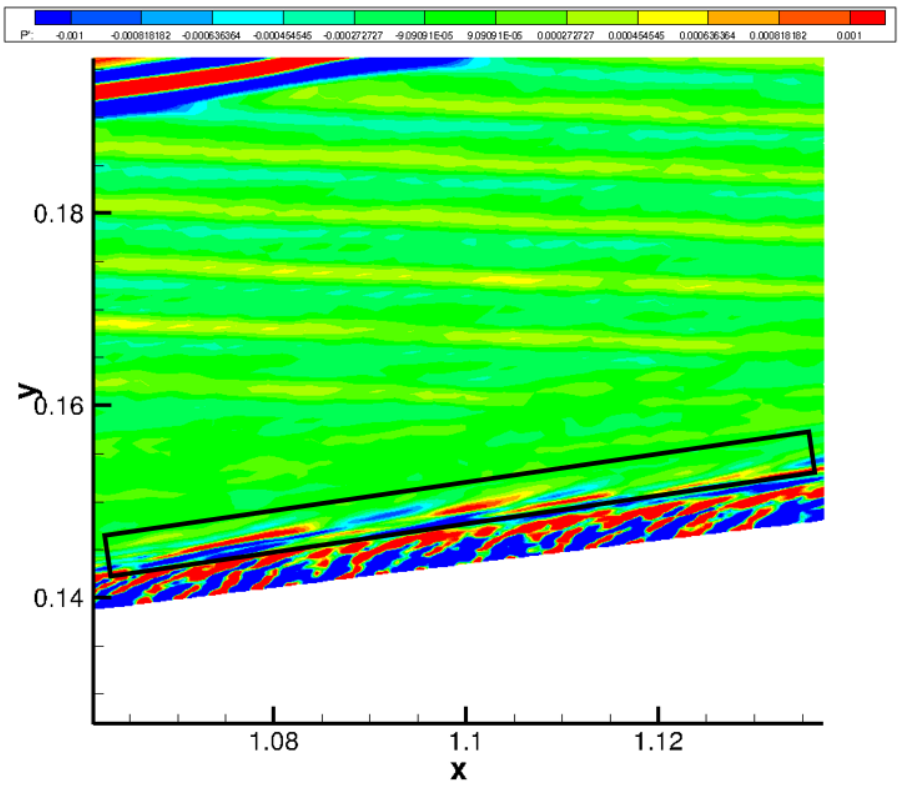

Figure 79. Y-Symmetry Plane Pressure Fluctuations Near the Surface of the Cone with R_N = 9.53 mm at Mach 10 with Distributed Surface Roughness

The instabilities seen in Figure 79 near the surface of the cone were further examined by extracting the pressure fluctuation data from the three streamtraces as indicated in Figure 80a. The first streamtrace was extracted in the region closest to the surface of the cone and streamtrace three was furthest from the surface. The resulting extracted pressure fluctuation data was plotted in Figure 80b. Intuitively, streamtrace one experienced the highest pressure fluctuations because it captured the majority of the distributed surface roughness phenomenon. The streamtraces path shown in Figure 80a demonstrated the entropy layer swallowing. When the streamtraces were incoming from the freestream they were equally spaced. As the entropy layer became entrained in the boundary layer, the streamtraces collapsed into a small region towards the back of the cone.

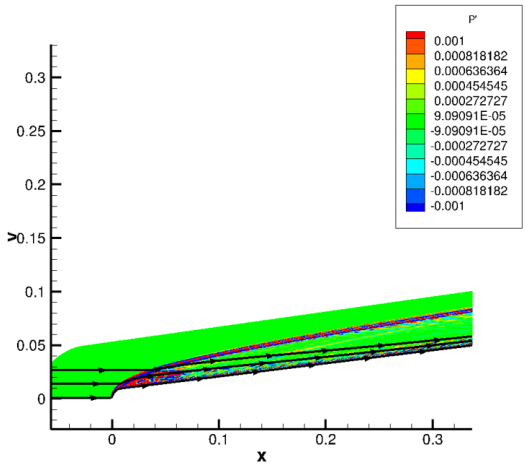

(a) Location of Streamtraces on the Y-Symmetry Plane

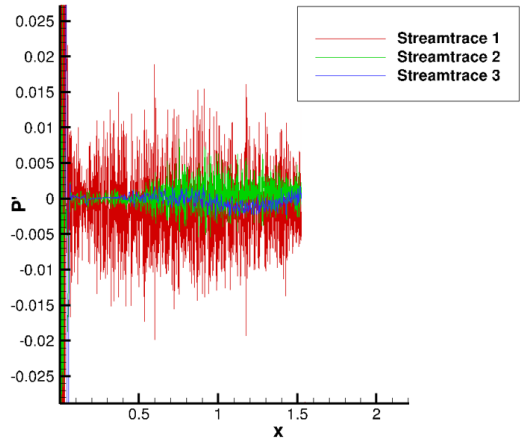

(b) Pressure Fluctuation Data Extracted from Streamtraces on the Y-Symmetry Plane

Figure 80. Streamtraces of Pressure Fluctuation

3.2 Rough Body Computational Analysis.

In Chatper 3 Section 3.2, the smooth body results were presented. The current section presents the rough body results in the same manner. Figures 81 and 83 provide full contour solution of the dynamic viscosity and the temperature while

Figures 82 and 84 are contour solutions focused on the nose region. Figures 81, 82, 83, and 84 appear nearly identical to the respective smooth body solutions provided in Chapter 3 Section 3.2 in Figures 51, 52, 55, and 56. In Section 3.1 of the current chapter, the rough body simulations showed no increase in heat flux to the body which indicated that the flow remained laminar. Therefore, it is expected that the temperature and dynamic viscosity contour solutions would appear similar. Indeed, similar flow features were seen in the temperature and dynamic viscosity solution domains were present in both the smooth and rough body simulations. Specifically, the isothermal boundary condition set at 298 K on the surface of the cone was properly enforced and the regions of highest magnitude of each flow variable occur in the nose region.

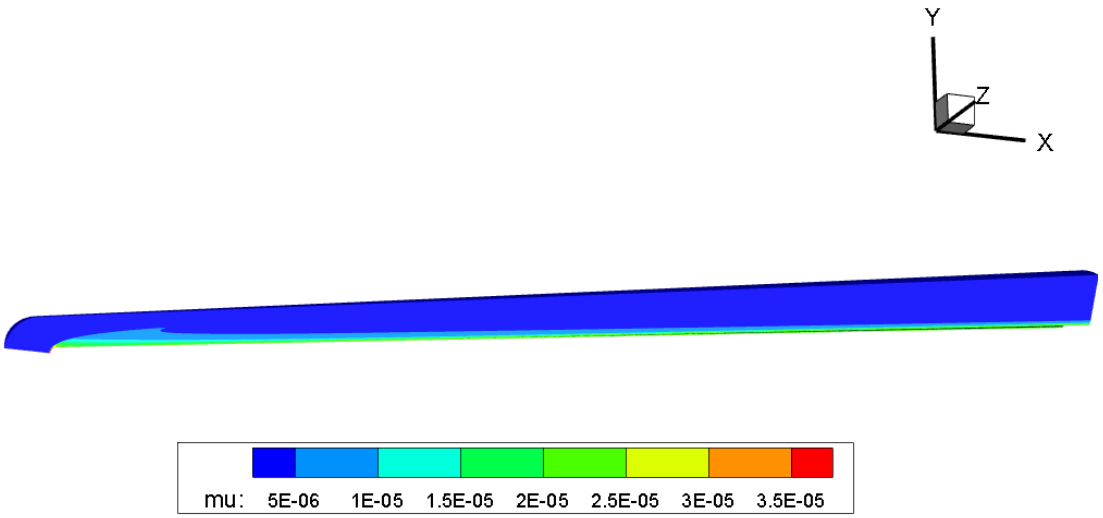

(a) R_N **= 9.53 mm**

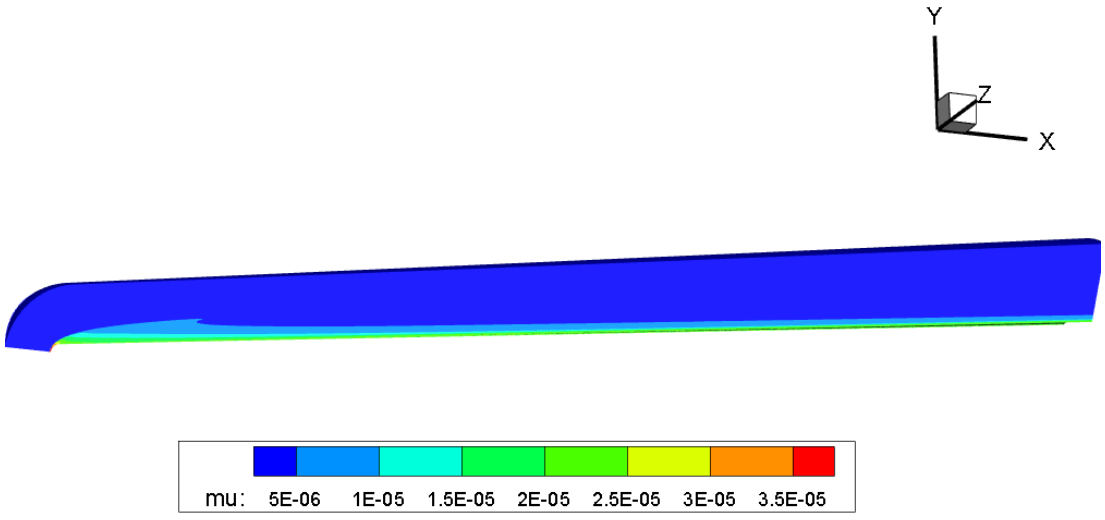

(b) R_N **= 12.7 mm**

Figure 81. Viscosity Contour Solution of Rough Body Flow at unit Reynolds number of 16.9×10^6 **/m on Fine Grid Refinement**

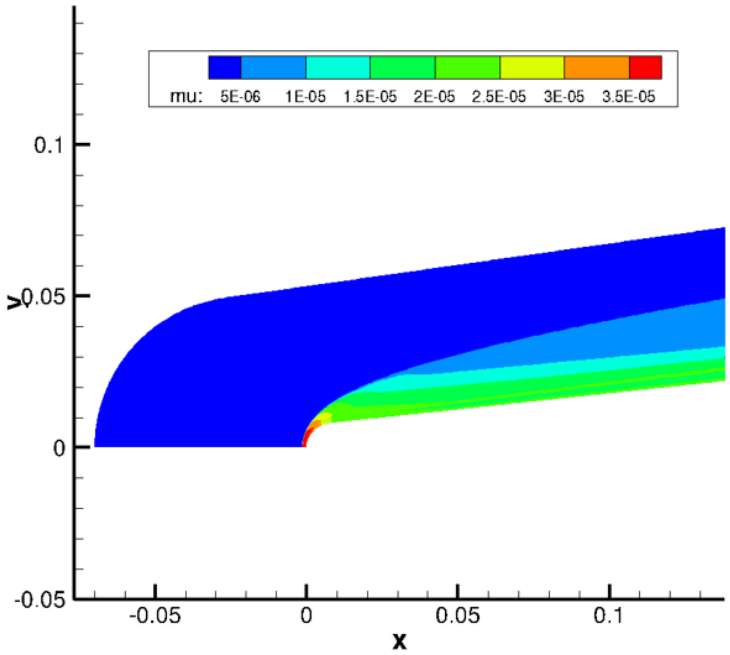

(a) R_N = **9.53 mm**

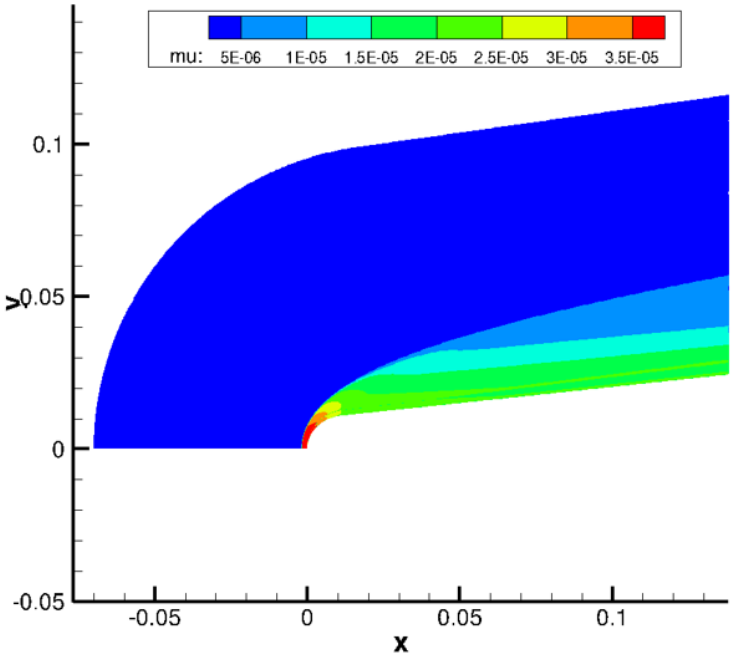

(b) R_N = **12.7 mm**

Figure 82. Viscosity Contour Solution on Nose Region of Cone of Rough Body Flow at unit Reynolds number of 16.9×10^6 **/m on Fine Grid Refinement**

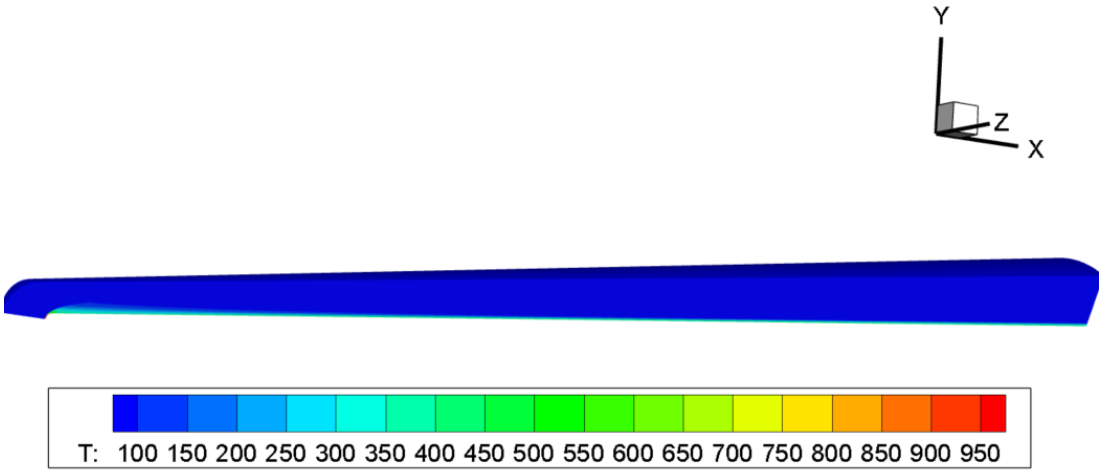

(a) R_N **= 9.53 mm**

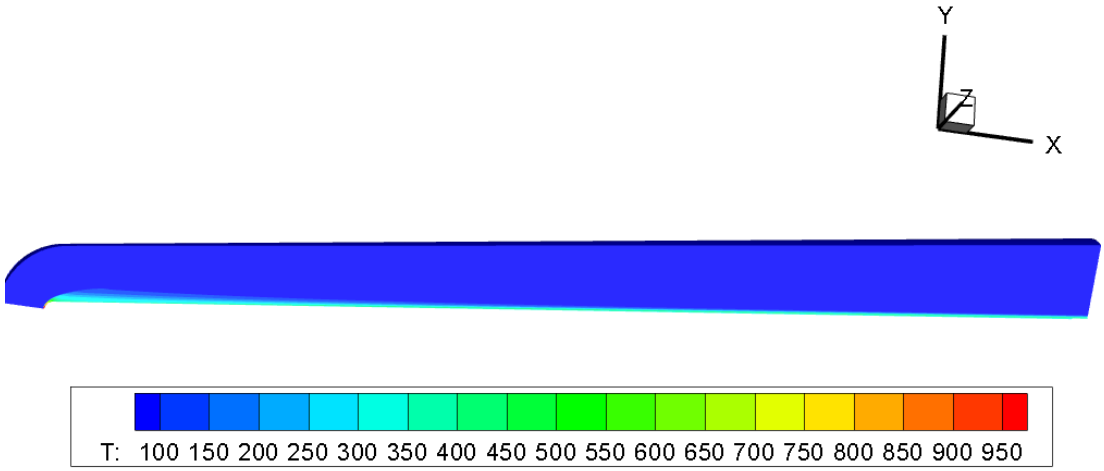

(b) R_N **= 12.7 mm**

Figure 83. Temperature Contour of Distributed Surface Roughness Simulations at unit Reynolds number of 16.9×10^6 **/m on Fine Grid Refinement**

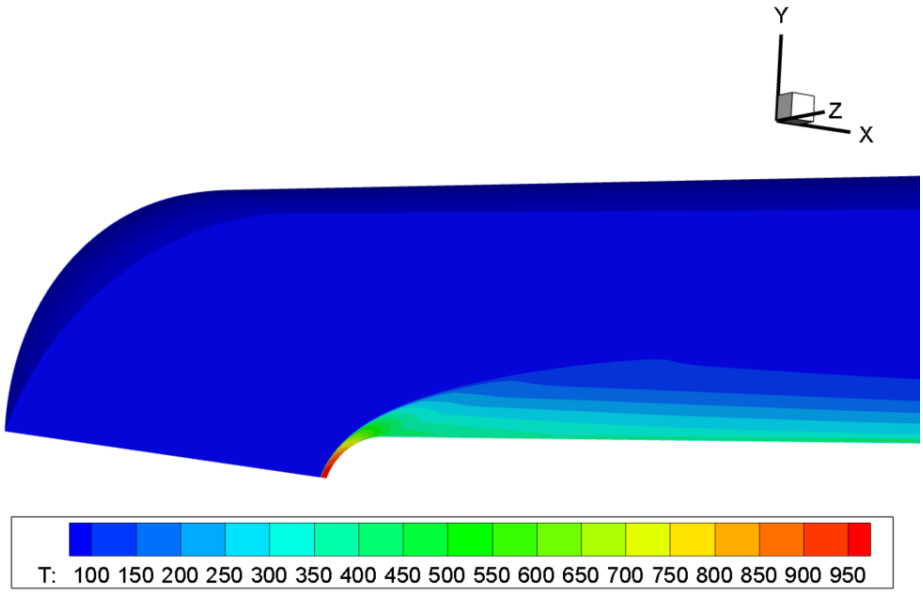

(a) R_N **= 9.53 mm**

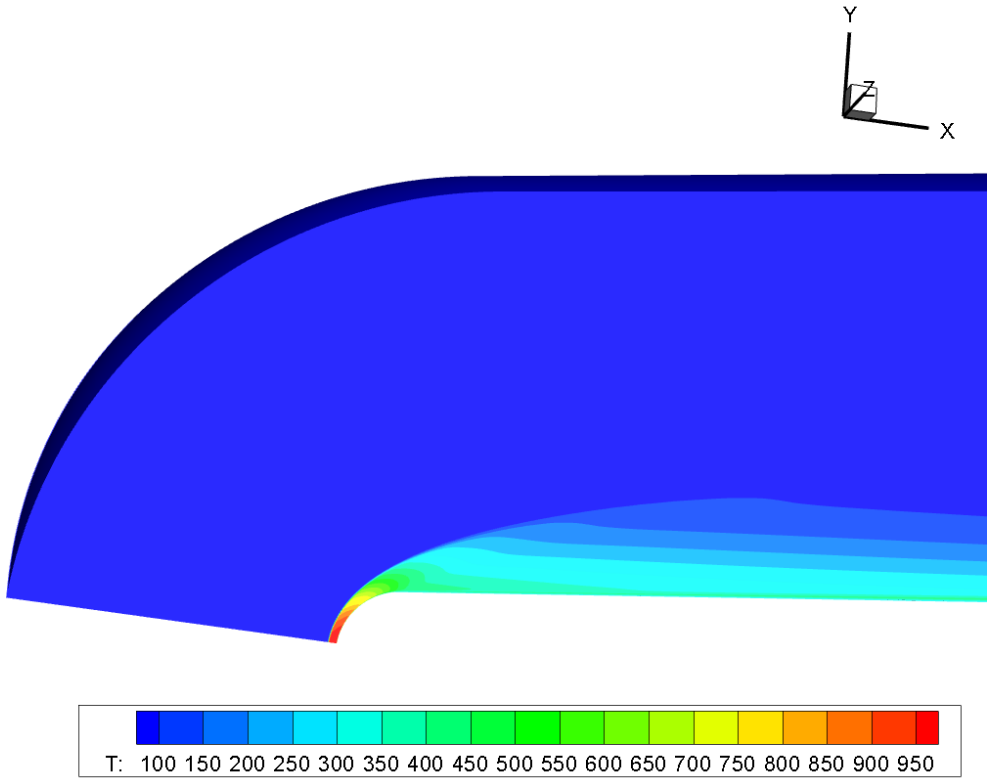

(b) R_N **= 12.7 mm**

Figure 84. Temperature Contour of Distributed Surface Roughness Simulations in the Nose Region at unit Reynolds number of 16.9×10^6 **/m on Fine Grid Refinement**

Figure 79 demonstrated that the distributed surface roughness forced an instability. However, Figure 75 provided the heat flux evidence that the forced instability did not transition the laminar flow into turbulent flow. Although the overall solution domains would appear similar, slight variations in the solution domain would exist due to the instabilities forced by distributed surface roughness. To compare these slight variations, temperature data was extracted in a vertical line at different streamwise positions on the smooth and rough body simulations for both the 9.53 and 12.7 mm nose radii cases and the results are shown in Figure 85. The data was extracted at the streamwise positions of 0.01 m, 0.02 m, and 0.05 m. In both nose radii cases, as the solution continued downstream the smooth body and rough body extracted temperature data lines differed less and after the streamwise position of 0.1 m any differences between the two solutions did not exceed the value of the uncertainty due to discretization. Therefore, the decision was made to examine the extracted temperature data lines at streamwise positions near the nose. For the 9.53 mm nose radius case shown in Figure 85a, the rough body extracted temperature data lines slightly exceeded the temperature data lines of the smooth body simulations. The consistent rise in temperature of the rough body simulations above the smooth body simulations was attributed to the presence of instabilities near the surface. For the 12.7 mm nose radius case shown in Figure 85b, only the streamwise position of 0.01 m demonstrated an increase in temperature for the rough body simulations and as the extracted temperature data line moved downstream the rough body simulations and the smooth body simulations matched within the discretization uncertainty.

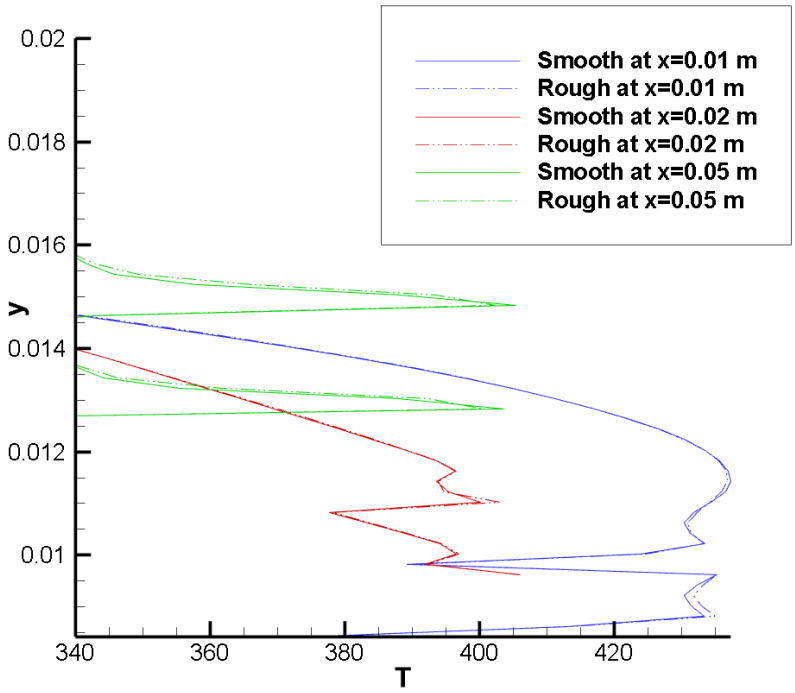

(a) R_N = **9.53 mm**

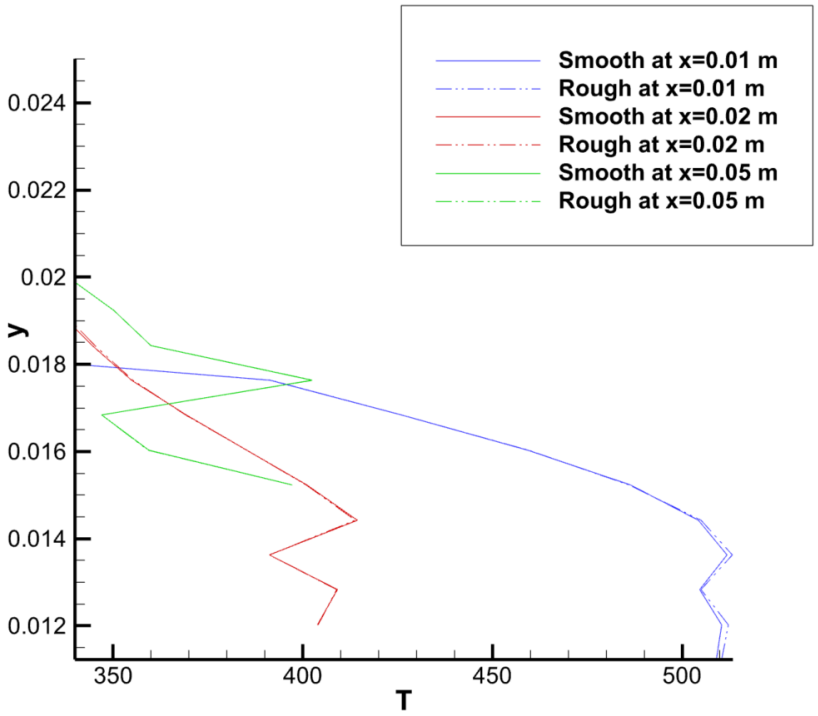

(b) R_N = **12.7 mm**

Figure 85. Temperature Contour Solution Slices of Smooth and Rough Body in the Nose Region at unit Reynolds number of 16.9×10^6 **/m on Fine Grid Refinement**

3.3 Pressure Power Spectral Density.

The pressure Power Spectral Density (PSD) calculations are used to identify the frequency of the instability experienced in an experiment or simulation and the location of the frequency on the geometry. The analysis of the experimental pressure PSDs were provided in Chapter 3 Section 1.3. The computational PSD for the 9.53 and 12.7 mm nose radii cases are provided in Figure 86 and 87. The 15 sensor coordinates are provided in Appendix A. The sensors span the length of the cone and mirror the sensor placement in the experiments conducted by Moraru [59]. The 9.53 mm nose radius case was created with 126,000 samples and was computed with a base frequency of 160,000 kHz. Similarly, the 19.7 mm nose radius case was created with 138,000 samples and was computed with a base frequency of 1,550,000 kHz. Recall from Section 2 that the grid tailoring was applied three times to the 9.53 mm nose radius case and two times to the 12.7 mm nose radius case. Previously, both the 9.53 mm and the 12.7 mm nose radius cases had been running with a time step on the order of 10^{-12}. After the third round of grid tailoring the 9.53 mm nose radius case was able to sustain stability with a timestep on the order of 10^{-11}. The 12.7 mm nose radius case did not undergo enough grid tailoring to be able to reduce the timestep thus the time accurate DNS was unable to run at a larger timestep.

From the results in Section 3.1, it was concluded that the flow remained laminar when the distributed surface roughness was the only forcing function present in the system. Therefore, it was not expected that a clear second mode frequency would be identifiable in the computational pressure PSD for either case. The pressure PSD routines required that the data collected be at the same timestep. Therefore, the data collection for the pressure PSDs was not run concurrently with the rough body simulations. As a result there were not enough computational hours to collect enough data samples to resolve the pressure PSDs to useful frequencies. The pressure PSD

for the 9.53 mm case shown in Figure 86 revels some frequency content. However, the frequency content does not reveal second mode instabilities. The pressure PSD for the 12.7 mm nose radius case shown in Figure 87 reveals no frequency content because the timestep for the 12.7 mm was an order of magnitude larger than the 9.53 mm nose radius case.

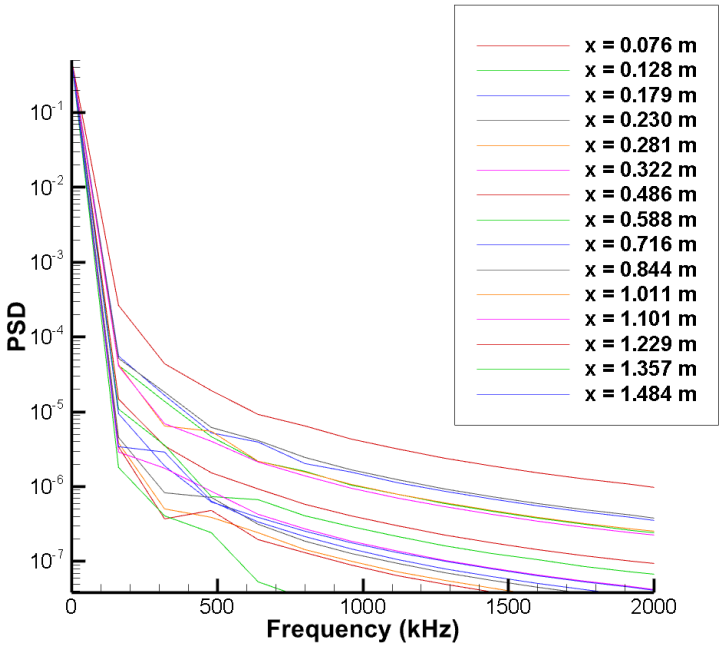

Figure 86. Pressure Power Spectral Density for R_N = 9.53 mm

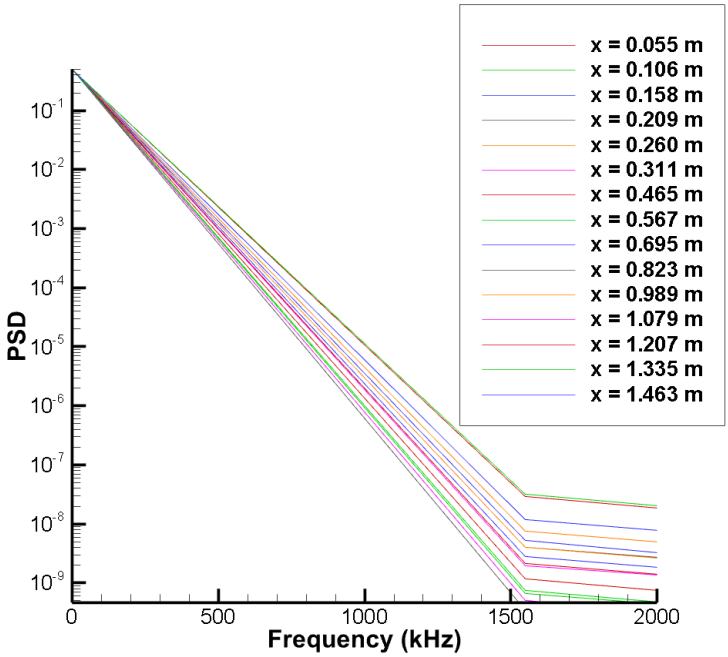

Figure 87. Pressure Power Spectral Density for R_N = 12.7 mm

4 Concluding Remarks

Chapter 4 covered the initial results of the simulation as a result of the methodology presented in Chapter 3. The analysis of the initial results indicated that adjustments in the form of grid tailoring were required for the time accurate DNS calculations. From the time accurate DNS with the tailored grid, it was concluded that the forcing function caused by the simulation of distributed surface roughness was not sufficient to transition the 7° axi-symmetric cones with the nose radii of 9.53 and 12.7 mm.

V. Conclusion

The ability to build proper thermal protection systems for hypersonic vehicle flight depends greatly on the ability to predict transition and the ability to predict transition is predicated on full understanding of the modalities to turbulent flow. Presently, the complexity of hypersonic boundary layer transition exceeds academic understanding but continues to be a quickly evolving and exciting area of research. The current research effort sought to pair the analysis of experimental data conducted by Moraru [59] with an analysis of data produced via computational means to gain insight into a non-modal transition phenomena which incurred a break with modern modal boundary layer transition theory as nose radius increased on axi-symmetric cones. The Arnold Engineering Development Center (AEDC) Hypervelocity Wind Tunnel 9 conducted experiments on six, 7° half-angle cones with increasing nose radii and documented the break with modern modal boundary layer transition theory between the nose radii of 9.53 and 12.7 mm. The cone with the nose radius of 9.53 mm was the last cone to conform to the established second mode dominated transition which dictated that as the nose radius increased the transition location would move downstream [72]. On the other hand, the cone with the nose radius of 12.7 mm broke with the established second mode precedent when the transition location failed to move downstream in correspondence to the increase in nose radius. The departure from modern modal transition theory observed in the 12.7 mm nose radius case was predicted to be caused by distributed surface roughness as a result of the machine finish on the physical test article [59]. In 1983, Stetson documented the same break with modern modal transition theory on blunt cones with increase nose radii and similarly hypothesized that the distributed surface roughness was an influencing factor on transition [79]. Therefore, the hypothesis that distributed surface roughness was a likely culprit for non-modal transition on blunt nose axi-symmetric cones has

been prevalent for almost four decades and was previously untested until the present research effort. In order to test this theory a computational fluid dynamic (CFD) direct numerical simulation (DNS) was run on both nose radii cases while simulated a distributed roughness surface at the same amplitude as the experimental test articles in effort to reproduce the experimental data. The totality of this research effort amounted to the conclusion that the transition experienced on the AEDC Tunnel 9 7° half-angle cones with the nose radii of 9.53 and 12.7 mm was not solely due to distributed surface roughness.

1 Key Findings

Distributed surface roughness has been a hypothesized reason for the break with modern modal theory since Stetson's 1983 and this research effort provided proof that the distributed forcing function caused by the simulated distributed roughness was insufficient. The heat transfer profile which resulted from the computational simulations which employed a distributed surface roughness at a maximum amplitude of 15 μm, it was concluded that transition did not occur. Further examination of the instabilities imposed by the distributed surface roughness revealed no meaningful frequency content and yielded N factors which immediately decayed. However, this conclusion does not exclude distributed surface roughness from playing an integral part in hypersonic boundary layer transition on blunt nose cones. The resulting instabilities from distributed surface roughness could be interacting with other disturbances and causing the non-modal transition phenomenon observed by Moraru [59] and Stetson [79].

2 Future Work

The results from the present research effort contribute to the conversation of the effects of distributed surface roughness on hypersonic boundary layer transition. That being stated, much work remains to achieve full understanding of the mechanisms that lead to boundary layer transition. In regards to the data aggregated in the current research effort, the interaction of the entropy layer and the boundary layer should be analyzed. As discussed in Section 1.2, the entropy layer is a region of inherent vorticity. Therefore analysis of the effects of the entropy layer swallowing are of poignant relevance to the overall understanding of boundary layer transition.

Improvements to the current research effort include aggressively tailoring the grids to achieve better alignment between the cell faces and the shock region. This would lead to the ability to run with a larger timestep. Additionally, the results of the instability resolution study in the spanwise direction dictated the necessary width of the cone slice. For future work it is suggested to reduce the model from a 30° slice to the minimum slice required to adequately resolve instabilities in the spanwise direction.

Ideally, improvements could be made to all distributed surface roughness studies by creating a distributed surface roughness that was not cell size dependent. The state of the art methodology of creating distributed surface roughness discussed in Section 3.5 was developed to force at the frequency of the grid cell size [21]. Therefore, the broadband forcing was a function of the grid. However, better conclusions about the effects of distributed surface roughness will be made when the distributed surface roughness methodology is not dependent on the modeling.

The conclusion of this work underpins the great scientific need of continuing the pragmatic study of individual influencing transitional factors as well as combination of influencing transitional factors. As referenced in Section 5, the factors which influence

transition are not additive in effect [8] therefore the study of the effects of distributed surface roughness alone is just the beginning of the journey to a full understanding of hypersonic boundary layer over axi-symmetric blunt nose cones. The research effort of performing a DNS while simulating distributed surface roughness with another forcing function such as noise or entropy layer instabilities would be a logical continuation of this research effort. Currently, there is no precedent for how the instabilities of freestream noise or instabilities entering through the entropy layer, a region of inherent voriticty, and instabilities of distributed surface roughness would interact with each other but arguably, these are likely instabilities to be interacting on axi-symmetric blunt nose cones.

The computational resources required for a DNS simulating the freestream noise and distributed surface roughness are high. However, the emerging input-output analysis for blunt nose cones emerging out of the University of Minnesota is trail blazing a new norm for hypersonic boundary layer transition theory. Recall from Section 6.5 that input-output analysis no longer employs the parallel flow assumption that fails to adequately model the flow phenomenon at the nose of the blunt cone. This methodology has the potential to completely replace the linear stability theory for the application of blunt nose cones. Even though the input-output analysis is only available for two dimensional slices of a geometry, valuable information on the characteristics of the instabilities could be gleaned by subjecting the AEDC Tunnel 9 geometries to this analysis. This analysis requires substantially less computational resources and is the recommended next step to this research effort in the computational domain.

Appendix A. Computational Sensor Location

Table 4. Sensor Locations on Computational Model for R_N = 9.53 mm

Sensor	X Location (m)	Y Location (m)	Z Location (m)
1	0.076	0.015	0.009
2	0.128	0.021	0.012
3	0.179	0.026	0.015
4	0.230	0.032	0.018
5	0.281	0.037	0.021
6	0.332	0.043	0.024
7	0.486	0.059	0.034
8	0.588	0.070	0.040
9	0.716	0.084	0.048
10	0.844	0.097	0.056
11	1.011	0.115	0.066
12	1.101	0.125	0.071
13	1.229	0.138	0.079
14	1.357	0.152	0.087
15	1.484	0.165	0.095

Table 5. Sensor Locations on Computational Model for R_N = 12.7 mm

Sensor	X Location (m)	Y Location (m)	Z Location (m)
1	0.055	0.016	0.009
2	0.106	0.021	0.012
3	0.158	0.027	0.015
4	0.209	0.032	0.018
5	0.260	0.037	0.022
6	0.311	0.043	0.025
7	0.465	0.058	0.034
8	0.567	0.070	0.040
9	0.695	0.084	0.048
10	0.823	0.097	0.056
11	0.989	0.115	0.066
12	1.079	0.125	0.072
13	1.207	0.138	0.080
14	1.335	0.152	0.088
15	1.463	0.165	0.095

Bibliography

1. Aleksandrova, E. A., A. V. Novikova, S. V. Utyzhnikov, and A. V. Fedorov. "Experimental Study of the Laminar Turbulent Transition on a Blunt Cone", *Journal of Applied Mechanic and Technical Physics*, 55(3):375–385, 2014. Doi: 10.1134/S0021894414030018.

2. Anderson, John D. Jr. *Modern Compressible Flow with Historical Perspective*, Series in Aeronautical and Aerospace Engineering. McGraw-Hill, 1990.

3. Anderson, John D. Jr. *Hypersonic and High-Temperature Gas Dynamics*, AIAA Education Series. AIAA, 2006.

4. Anderson, John D. Jr. *Fundamentals of Aerodynamics*, Series in Aeronautical and Aerospace Engineering. McGraw-Hill, 2007.

5. Azim, R., M. Hasan M., and Mohammad Ali. "Numerical Investigation on the delay of boundary layer separation by suction for NACA 4412", *Procedia Engineering*, 105:329–334, 2015. Doi: 10.1016/j.proeng.2015.05.013.

6. Bergman, Theodore L., Adrienne S. Lavine, Frank P. Incropera, and David P. Dewitt. *Fundamentals of Heat and Mass Transfer*. Wiley, 2011.

7. Blazek, Jiri. *Computational Fluid Dynamics: Principles and Applications*. Butterworth-Heinemann, 2015.

8. Braslow, Albert L. "A Review of Factors Affecting Boundary Layer Transition", *NASA*, 1966. TN D-3384.

9. Candler, Graham V., Heath B. Johnson, Ioannis Nompelis, Vladimyr M. Gidzak, Pramod K. Subbareddy, and Michael Barnhardt. "Development of the US3D Code for Advanced Compressible and Reacting Flow Simulations", *53rd AIAA Aerospace Sciences Meeting*, (January):1–27, 2015. Doi: 10.2514/6.2015-1893.

10. Candler, Graham V., Pramod K. Subbareddy, and Ioannis Nompelis. *Hypersonic Nonequilibrium Flows: Fundamentals and Recent Advances*, volume 247, chapter CFD Methods for Hypersonic Flows and Aerothermodynamcis, 203–238. Progress in Astronautics and Aeronautics, 2016. Doi: 10.2514/4.103292.

11. Casper, Katya M., Steven J. Beresh, John F. Henfling, Russell W. Spillers, Brian O. M. Pruett, and Steven P. Schneider. "Hypersonic Wind-Tunnel Measurements of Boundary-Layer Transition on a Slender Cone", *AIAA Journal*, 54(4):1250–1263, 2016. Doi: 10.2514/1.J054033.

12. Casper, Katya M., Heath B. Johnson, and Steven P. Schneider. "Effect of Freestream Noise on Roughness-Induced Transition for a Slender Cone", *Journal of Spacecraft and Rockets*, 48(3):406–413, 2011. Doi: 10.2514/1.48300.

13. Celik, Ismail B., Urmila Ghia, Patrick J. Roache, Christopher J. Freitas, Hugh Coleman, and Peter E. Raad. "Procedure for Estimation and Reporting of Uncertainty Due to Discretization in CFD Applications", *Journal of Fluids Engineering*, 130(7), 2008. Doi: 10.1115/1.2960953.

14. Chandrasekhar, S. *Hydrodynamic and Hydrodynamic Stability*, The International Series of Monographs on Physics. Oxford, 1961.

15. Chaudhry, Ross. "Print Element (PrintElem)".

16. Cook, David A., John S. Thome, Joseph M. Brock, Joseph W. Nichols, and Graham V. Candler. "Understanding effects of nose-cone bluntness on hypersonic boundary layer transition using input-output analysis", *AIAA SchiTech Forum*, 1–15, January 2018. Doi: 10.2514/6.2018-0378.

17. Cook, David A., John S. Thome, Joseph W. Nichols, and Graham V. Candler. "Receptivity Analysis of BOLT to Distributed Surface Roughness Using Input-Output Analysis", *AIAA Scitech*, 1–13, January 2019. Doi: 10.2514/6.2019-0089.

18. Cummings, Russell M., William H. Mason, Scott A. Morton, and David R. McDaniel. *Applied Computational Aerodynamics: A Modern Engineering Approach*, Cambridge Aerospace Series. Cambridge University Press, 2017.

19. Dietz, G. and S. Hein. "Entropy-Layer Instabilities over a Blunted Flat Plate in Supersonic Flow", *Physics of Fluids*, 11(1):7–9, 1999. 10.1063/1.869899.

20. Dinzl, Derek J. *Analysis of Crossflow Instability on HIFiRE-5 using Direct Numerical Simulation*. Ph.D. thesis, University of Minnesota, February 2016.

21. Dinzl, Derek J. and Graham V. Candler. "Direct Simulation of Hypersonic Crossflow Instability on an Elliptic Cone", *AIAA Journal*, 55(6):1769–1782, 2017. Doi: 10.2514/1.J055130.

22. Ducros, F., V. Ferrand, F. Nicoud, C. Weber, D. Darracq, C. Gacherieu, and T. Poinsot. "Large-eddy simulation of shock/turbulence interation", *Journal of Computational Physics*, 152(2):517–549, 1999. Doi: 10.1006/jcph.1999.6238.

23. Edelman, Joshua B. and Steven P. Schneider. "Secondary Instabilities of Hypersonic Stationary Crossflow Waves", *AIAA Journal*, 56(1):182–192, 2018. Doi: 10.2514/1.J056028.

24. Estorf, Malte, Rolf Radespiel, Steven P. Schneider, Heath B. Johnson, and Stefan Hein. "Surface-Pressure Measurements of Second-Mode Instability in Quiet Hypersonic Flow", *46th AIAA Aerospace Sciences Meeting and Exhibit*, January 2008. Doi: 10.2514/6.2008-1153.

25. Fedorov, Alexander, Vitaly Soudakov, Ivan Egorov, Andrey Sidorenko, Yury Gromyko, Dmitry Bountin, Pavel Polivanov, and Anatoly Maslov. "High-Speed Boundary-Layer Stability on a Cone with Localized Wall Heating or Cooling", *AIAA Journal*, 53(9):2512–2524, September 2015. Doi: 10.2514/I.J05366.

26. Fedorov, Alexander and Anatoli Tumin. "Evolution of Disturbances in Entropy Layer on Blunted Plate in Supersonic Flow", *AIAA Journal*, 42(1):89–94, 2004. Doi: 10.2514/1.9033.

27. Fisher, David F. and N. Sam Jr. Dougherty. "Flight and Wind Tunnel Correlation of Boundary-Layer Transition on the AEDC Transition Cone", *NASA*, Technical Memorandum 84902, October 1982.

28. Fisher, David F. and N. Sam Jr. Dougherty. "In-Flight Transition Measurement on a 10-Deg Cone at Mach Numbers from 0.5 to 2.0", *NASA*, TP-1971, June 1982.

29. Floryan, Jerzy M. and William S. Saric. "Stability of Gortler Vortices in Boundary Layers", *AIAA Journal*, 20(3):316–324, 1982. Doi: 10.2514/3.51076.

30. Greenwood, Roger T. *Measurements of Entropy-Layer Instabilities over Cone-Ogive-Cylinders at Mach 6*. Ph.D. thesis, Purdue University, December 2014.

31. Greenwood, Roger T. and Steven P. Schneider. "Measurements of Entropy-Layer Instabilities over Cone-Ogive-Cylinders in a Mach-6 Quiet Tunnel", *AIAA SciTech Forum*, 1–21, January 2016. Doi: 10.2514/6.2019-0627.

32. Gronvall, Joel E., Heath B. Johnson, and Graham V. Candler. "Hypersonic three-dimensional boundary layer transition on a cone at angle of attack", *AIAA Journal*, 2011. Doi: 10.2514/6.2012-2822.

33. Hein, S. "Numerical Investigation of Hypersonic Wall-Bounded Shear Flows - Part 2L Entropy Layer Instability in Blunt Cone Flows", *ERCOFTAC Bulletin*, 74:57–60, 2007.

34. Itoh, Nobutake. "The origin and subsequent development of Tollmien-Schlichting waves in a boundary layer", *Fluid Dynamics Research*, 1(2):119–130, 1986. Doi: 10.1016/0169-5983(86)90012-2.

35. Jewell, Joseph S., Richard E. Kennedy, Stuart J. Laurence, and Roger L. Kimmel. "Transition on a Variable Bluntness 7-Degree Cone at High Reynolds Number", *AIAA Journal*, 2018. Doi: 10.2514/6.2018-1822.

36. Johnson, Heath B., Travis W. Drayna, Ioannis Nompelis, and Graham V. Candler. *US3D Software User Manual*. Department of Aerospace Engineering and Mechanics of Univeristy of Minnesota, version 1.0 (beta) edition).

37. Klebanoff, P. S. "Characteristics of Turbulence in a Boundary Layer with Zero Pressure Gradient", *National Advisory Committee for Aeronautics*, 1–19, 1955. Report 1247.

38. Knisely, Carleton P. and Xiaolin Zhong. "An Investigation of Sound Radiation by Supersonic Unstable Modes in Hypersonic Boundary Layers", *AIAA Aviation*, 1–41, June 2017. Doi: 10.2514/6.2017-4516.

39. Knisely, Carleton P. and Xiaolin Zhong. "Supersonic Modes in Hot-Wall Hypersonic Boundary Layers with Thermochemcial Nonequilibrium Effects", *AIAA SciTech*, 1–31, January 2018. Doi: 10.2514/6.2018-2085.

40. Knisely, Carleton P. and Xiaolin Zhong. "Impact of Thermochemical Nonequilibrium Effects on the Supersonic Mode in Hypersonic Boundry Layers", *AIAA SciTech*, 1–1, January 2019. Doi: 10.2514/6.2019-1132.

41. Komives, Jeffrey R. *Development and Validation of a Turbulence Wall Model for Compressible Flows with Heat Transfer*. Ph.D. thesis, University of Minnesota, 2016.

42. Kostak, Heather B., Rodney D. W. Bowersox, Gregory R. McKiernan, John Thome, Graham V. Candler, and Rudolph A. King. "Freestream Disturbance Effects on Boundary Layer Instability and Transition on the AFOSR BOLT Geometry", *AIAA SciTech Forum*, 1–24, January 2019. Doi: 10.2514/6.2019-0088.

43. Lafferty, John F. and Joseph D. Norris. "Measurements of Fluctuating Pitot Pressure, "Tunnel Noise," in the AEDC Hypervelocity Wind Tunnel No. 9", *2007 U.S. Air Force Test and Evaluation Days*, 2007. Doi: 10.2514/6.2007-1678.

44. van Leer, Bram. "Towards the Ultimate Conservative Difference Scheme. V. A. Second-Order Sequal to Godunov's Method", *Journal of Computational Physics*, 32(1):101–136, July 1979. Doi: 10.1016/0021-9991(79)90145-1.

45. Liao, Wei, Mujeeb R. Malik, Elizabeth M. Lee-Rausch, Fei Li, Eric J. Nielsen, Pieter G. Buning, Meelan Choudhari, and Chau-Lyan Chang. "Boundary-Layer Stability Analysis of the Mean Flows Obtained Using Unstructured Grids", *42nd AIAA Fluid Dynamics Conference and Exhibit*, 52(1):49–63, June 2015. Doi: 10.2514/1.C032583.

46. Low, George M. "Boundary-Layer Transition at Supersonic Speeds", *NACA*, RM E56E10, 1956.

47. MacCormack, Robert W. *Numerical Computation of Compressible and Viscous Flow*, AIAA Education Series. AIAA, 2014.

48. Mack, Leslie M. "Linear Stability Theory and the Problem of Supersonic Boundary-Layer Transition", *AIAA-Journal*, 1957. Doi: 10.2514/3.49693.

49. Mack, Leslie M. "Transition and Laminar Instability", *NASA*, 1977. CP-153203.

50. Mack, Leslie M. "Special Course on Stability and Transition of Laminar Flow", *AGARD*, Report 709:1–81, 1984.

51. Malik, Mujeeb R. "Numerical Methods for Hypersonic Boundary Layer Stability", *Journal of Computational Physics*, 86(2):376–413, 1990. Doi: 10.1016/0021-9991.

52. Malik, Mujeeb R., Fei Li, Meelan M. Choudhari, and Chau-Lyan Chang. "Secondary instabilities of crossflow vorticies and swept-wing boundary-layer trnasition", *Journal of Fluid Mechanics*, 399:85–115, 1999.

53. Marineau, Eric C. "Prediction Methodology for Second-Mode-Dominated Boundary-Layer Transition in Wind Tunnels", *AIAA Journal*, 55(2):484–499, 2017. Doi: 10.2514/1.J055061.

54. Marineau, Eric C., George C. Moraru, Daniel R. Lewis, Joseph D. Norris, John F. Lafferty, and Heath B. Johnson. "Investigation of Mach 10 Boundary Layer Stability of Sharp Cones at Angle-of-Attack, Part 1: Experiments", *53rd AIAA Aerospace Sciences Meeting*, (January):1–21, 2015. Doi: 10.2514/6.2015-1737.

55. Marineau, Eric C, George C. Moraru, Daniel R Lewis, Joseph D Norris, John F Lafferty, Ross M Wagnild, and Justin A Smith. "Mach 10 Boundary Layer Transition Experiments on Sharp and Blunted Cones", *19th AIAA International Space Planes and Hypersonic Systems and Technologies Conference*, 12(June):1–24, 2014. Doi: 10.2514/6.2014-3108.

56. Marren, D. and John F. Lafferty. "The AEDC Hypervelocity Wind Tunnel 9", *Advanced Hypersonic Test Facilities, Progress in Aeronautics and Astronautics*, 2002.

57. Mendez, M., M. S. Shadloo, A. Hadjadj, and A. Ducoin. "Boundary layer transition over a concave surface caused by centrifugal instabilities", *Computers and Fluids*, 171:135–153, 2018. Doi: 10.1016/j.compfluid.2018.06.009.

58. Moore, Franklin K. "Laminar Boundary Layer on a Circular Cone in Supersonic Flow at Small Angles of Attack", *NACA*, TN 2521, October 1951.

59. Moraru, Ciprian G. *Hypersonic Boundary-Layer Transition Measurements at Mach 10 on a Large Seven-Degree Cone at Angle of Attack*. Master's thesis, Purdue University, August 2015.

60. Morkovin, M. V. "Instability, Transition to Turbulence and Predictability", *AGARD*, Report 236:1–33, 1977.

61. Panton, Robert L. *Incompressible Flow*. Wiley, 2013.

62. Paredes, Pedro, Meelan M. Choudhari, Fei Li, Joseph S. Jewell, and Roger L. Kimmel. "Nonmodal Growth of Traveling Waves on Blunt Cones at Hypersonic Speeds", *AIAA SciTech Forum*, 1–18, January 2019. Doi: 10.2514/6.2019-0876.

63. Paredes, Pedro, Meelan M. Choudhari, Fei Li, Joseph S. Jewell, Roger L. Kimmel, Eric C. Marineau, and Guillaume Grossir. "Nosetip Bluntness Effects on Transition at Hypersonic Speeds: Experimental and Numerical Analysis Under NATO STO AVT-240", *AIAA Aerospace Sciences Meeting*, 1–26, January 2018. Doi: 10.2514/6.2018-0057.

64. Pope, Stephen B. *Turbulent Flows*. Cambridge University Press, 2000.

65. Reshotko, Eli. "Boundary Layer Instability, Transition and Control", *32nd Aerospace Sciences Meeting and Exhibit*, January 1994. Doi: 10.2514/6.1994-1.

66. Reynolds, Osborne. "On the Dynamical Theory of Incompressible Viscous Fluids and the Determination of Criterion", 1894. URL `http://rsta.royalsocietypublishing.org/content/roypta/186/123.full.pdf`. Accessed: September 21, 2018.

67. Roache, Patrick J. "Perspective: A Method for Uniform Reporting of Grid Refinement Studies", *Journal of Fluids Engineering*, 116:405–413, 1994. Doi: 10.1115/1.2910291.

68. Saric, William S., Helen L. Reed, and Edward B. White. "Stability and Transition of Three-Dimesional Boundary Layers", *Annual Review of Fluid Mechanics*, 35(1):413–440, 2003. Doi: 10.1146/annurev.fluid.35.101101.161045.

69. Schlichting, Heermann and Gersten Klaus. *Boundary-Layer Theory*. Springer, 2017.

70. Schneider, Steven P. "Design of a Mach-6 Quiet-Flow Wind-Tunnel Nozzle Using the e**N Method for Transition Estimation", *36th AIAA Aerospace Sciences Meeting and Exhibit*, 1997. Doi: 10.2514/6.1998-547.

71. Schneider, Steven P. "Effects of High-Speed Tunnel Noise on Laminar-Turbulent Transition", *Journal of Spacecraft and Rockets*, 38(3):323–333, 2001. Doi: 10.2514/2.3705.

72. Schneider, Steven P. "Hypersonic laminar-turbulent transition on circular cones and scramjet forebodies", *Progress in Aerospace Sciences*, 40(1-2):1–50, 2004. Doi: 10.1016/j.paerosci.2003.11.001.

73. Schneider, Steven P. "Development of Hypersonic Quiet Tunnels", *Journal of Spacecraft and Rockets*, 45(4):641–664, 2008. Doi: 10.2514/1.34489.

74. Schneider, Steven P. "Effects of Roughness on Hypersonic Boundary-Layer Transition", *Journal of Spacecraft and Rockets*, 45(2):193–209, 2008. Doi: 10.2514/1.29713.

75. Schneider, Steven P. "Summary of Hypersonic Boundary-Layer Transition Experiments on Blunt Bodies with Roughness", *Journal of Spacecraft and Rockets*, 45(6):1090–1105, 2008. Doi: 10.2514/1.37431.

76. Schneider, Steven P. "Developing mechanism-based methods for estimating hypersonic boundary-layer transition in flight: The role of quiet tunnels", *Progress in Aerospace Sciences*, 72:17–29, 2015. Doi: 10.1016/j.paerosci.2014.09.008.

77. Schubauer, G. B. and H. K. Skramstad. "Laminar Boundary-Layer Oscillations and Stability of Laminar Flow", *Journal of the Aeronautical Sciences*, 14(2):69–78, February 1947.

78. Stetson, Kenneth F. "Mach 6 Experiments of Transition on a Cone at Angle of Attack", *Journal of Spacecraft and Rockets*, 19(5):397–403, 1982. Doi: 10.2514/3.62276.

79. Stetson, Kenneth F. "Nosetip Bluntness Effects on Cone Fustrum Boundary Layer Transition in Hypersonic Flow", *16th Fluid and Plasma Dynamics Conference*, July 1983. Doi: 10.2514/6.1983-1763.

80. Stetson, Kenneth F. and Roger L. Kimmel. "On Hypersonic Boundary-Layer Stability", *AIAA Journal*, January 1992. Doi: 10.2514/6.1992-737.

81. Stetson, Kenneth F. and George H. Rushton. "Shock Tunnel Investigation of Boundary-Layer Transition at M = 5.5", *AIAA Journal*, 5(5):899–906, 1967. 10.2514/3.4098.

82. Stetson, Kenneth F., Elton R. Thompson, Joseph C. Donaldson, and Leo G. Siler. "Laminar Boundary Layer Stability Experiments on a Cone at Mach 8, Part 2: Blunt Cone", *AIAA 22nd Aerospace Sciences Meeting*, January 1984. Doi: 10.2514/6.1984-6.

83. Su, Caihong. "DNS of Wave Packets in a Supersonic Boundary Layer: A Validation for a Popular Transition Prediction Method Based on Linear Stability Theory", *Procedia IUTAM*, 14:534–552, 2015. Doi: 10.1016/j.piutam.2015.03.081.

84. Subbareddy, Pramod K. and Graham V. Candler. "A fully discrete, kinetic energy consistent finite-volume scheme for compressible flows", *Journal of Computational Physicss*, 228(5), March 2009. Doi: 10.1016/j.jcp.2008.10.026.

85. Subbareddy, Pramod K. and Graham V. Candler. "DNS of Transition to Turbulence in a Mach 6 Boundary Layer", *43rd AIAA Thermophysics Conference*, 1–14, June 2013. Doi: 10.2514/6.2012-3106.

86. Thompson, Ryan. "Local Timestep US3D User Routines", November 2018.

87. Umantsev, Alexander. "Conditions of Stable Equilibrium". http://faculty.uncfsu.edu/aumantsev, August 2014. Fayetteville State Univeristy.

88. Wheaton, Bradley M. and Steven P. Schneider. "Roughness-Induced Instability in a Hypersonic Laminar Boundary Layer", *AIAA Journal*, 50(6):1245–1256, 2012. Doi: 10.2514/1.J051199.

89. White, Edward B. and William S. Saric. "Secondary instability of crossflow vortices", *Journal of Fluid Mechanics*, 525:275–308, 2005.

90. White, Frank M. *Viscous Fluid Flow*. McGraw-Hill, 2006.

91. Wright, M. J., Graham V. Candler, and D. Bose. "Data-Parallel Line Relaxation Method for Navier-Stokes Equations", *AIAA Journal*, 36(9):1603–1609, September 1998. Doi: 10.2514/2.586.

REPORT DOCUMENTATION PAGE

Form Approved
OMB No. 0704–0188

1. REPORT DATE *(DD–MM–YYYY)*	2. REPORT TYPE	3. DATES COVERED *(From — To)*
21–03–2019	Master's Thesis	Aug 2017 — Mar 2019

4. TITLE AND SUBTITLE

Direct Numerical Simulation of Roughness Induced Hypersonic Boundary Layer Transition on a 7° Half-Angle Cone

5a. CONTRACT NUMBER

5b. GRANT NUMBER

5c. PROGRAM ELEMENT NUMBER

6. AUTHOR(S)

Crouch, Tara E., 1st Lt, USAF

5d. PROJECT NUMBER

19Y373

5e. TASK NUMBER

5f. WORK UNIT NUMBER

7. PERFORMING ORGANIZATION NAME(S) AND ADDRESS(ES)

Air Force Institute of Technology
Graduate School of Engineering and Management (AFIT/EN)
2950 Hobson Way
WPAFB OH 45433-7765

8. PERFORMING ORGANIZATION REPORT NUMBER

AFIT-ENY-MS-19-M-211

9. SPONSORING / MONITORING AGENCY NAME(S) AND ADDRESS(ES)

Arnold Engineering Development Center
Attn: John F. Lafferty, NH-04
Technical Director-Tunnel 9
White Oak, MD 20903
(301)394-6405 (DSN: 290-6405)
Email: john.lafferty@us.af.mil

10. SPONSOR/MONITOR'S ACRONYM(S)

11. SPONSOR/MONITOR'S REPORT NUMBER(S)

12. DISTRIBUTION / AVAILABILITY STATEMENT

Distribution Statement A:
Approved for Public Release: Distribution unlimited.

13. SUPPLEMENTARY NOTES

14. ABSTRACT

Direct numerical simulation (DNS) computational fluid dynamic (CFD) calculations were performed on a 30° slice of 7° half-angle cones with increasing nose radii bluntness at Mach 10 while simulating a distributed roughness pattern on the cone surface. These DNS computations were designed to determine if the non-modal transition behavior observed by the Arnold Engineering Development Center (AEDC) Hypervelocity Wind Tunnel 9 was induced via distributed surface roughness. When boundary layer transition is dominated by second mode instabilities, an increase in nose radius delays the transition location downstream. However, blunt nose experiments indicated that as the nose radius continued to increase from sharp to blunt, the transition location was no longer second mode dominated and the transition location failed to continue to move downstream. The DNS results employed the grids which simulated distributed roughness by moving the nodes on the surface according to a normal distribution centered on the maximum roughness height. The results showed that the distributed surface roughness was not sufficient to cause transitional flow. The cause of transition in the AEDC Tunnel 9 experiments was due to freestream disturbances or a combination of freestream disturbances with distributed surface roughness.

15. SUBJECT TERMS

Hypersonic, Computational Fluid Dynamics (CFD), Direct Numerical Simulation (DNS), Blunt Cones, Surface Roughness

16. SECURITY CLASSIFICATION OF:			17. LIMITATION OF ABSTRACT	18. NUMBER OF PAGES	19a. NAME OF RESPONSIBLE PERSON
a. REPORT	b. ABSTRACT	c. THIS PAGE			Lt. Col Jeffrey R. Komives, AFIT/ENY
U	U	U	UU	224	19b. TELEPHONE NUMBER *(include area code)* (937) 255-3636, x4744; Jeffrey.Komives@afit.edu